

Heterogeneous Photochemistry: Solar Energy Conversion and Environmental Remediation

Guest Editors: Daniele Dondi, Sandra Babić, Irene Michael,
Giovanni Palmisano, and Andrea Speltini





Heterogeneous Photochemistry: Solar Energy Conversion and Environmental Remediation

International Journal of Photoenergy

Heterogeneous Photochemistry: Solar Energy Conversion and Environmental Remediation

Guest Editors: Daniele Dondi, Sandra Babić, Irene Michael, Giovanni Palmisano, and Andrea Speltini



Copyright © 2016 Hindawi Publishing Corporation. All rights reserved.

This is a special issue published in "International Journal of Photoenergy." All articles are open access articles distributed under the Creative Commons Attribution License, which permits unrestricted use, distribution, and reproduction in any medium, provided the original work is properly cited.

Editorial Board

- M. S.A. Abdel-Mottaleb, Egypt
Angelo Albini, Italy
Maan Alkaisi, New Zealand
Xavier Allonas, France
Nicolas Alonso-Vante, France
Alberto Alvarez, Mexico
Wayne A. Anderson, USA
Raja S. Ashraf, UK
Vincenzo Augugliaro, Italy
Detlef W. Bahnemann, Germany
Antonio Barbon, Italy
Valeriy Batoev, Russia
Laura Bellia, Italy
Ignazio Renato Bellobono, Italy
Raghu N. Bhattacharya, USA
Simona Binetti, Italy
Fabio Bisegna, Italy
Thomas M. Brown, Italy
Stephan Buecheler, Switzerland
Gion Calzaferrì, Switzerland
Joaquim Carneiro, Portugal
Carlo S. Casari, Italy
Yatendra S. Chaudhary, India
Chuncheng Chen, China
Věra Cimrová, Czech Republic
Juan M. Coronado, Spain
P. Davide Cozzoli, Italy
Ying Dai, China
Dionysios D. Dionysiou, USA
Abderrazek Douhal, Spain
Miroslav Dramićanin, Serbia
Mahmoud M. El-Nahass, Egypt
Polycarpos Falaras, Greece
Chris Ferekides, USA
Paolo Fornasiero, Italy
Manuel Fuentes Conde, Spain
Hermenegildo García, Spain
Germà García-Belmonte, Spain
David García-Fresnadillo, Spain
Elisa Isabel Garcia-Lopez, Italy
- Beverley Glass, Australia
Daniel Glossman-Mitnik, Mexico
Mohammed Ashraf Gondal, KSA
Giulia Grancini, Switzerland
Hidehisa Hagiwara, Japan
Anthony M. Harriman, UK
Michael D. Heagy, USA
Shinya Higashimoto, Japan
Cheuk-Lam Ho, Hong Kong
Wing-Kei Ho, Hong Kong
Jürgen Hüpkès, Germany
Adel A. Ismail, Egypt
Chun-Sheng Jiang, USA
Jurga Juodkazyte, Lithuania
Shahed Khan, USA
Sylvie Lacombe, France
Fernando Langa, Spain
Cooper H. Langford, Canada
Stefan Lis, Poland
Vittorio Loddo, Italy
Gongxuan Lu, China
Wouter Maes, Belgium
Manuel Ignacio Maldonado, Spain
Tapas Mallick, UK
Dionissios Mantzavinos, Greece
Ugo Mazzucato, Italy
Sheng Meng, China
Santolo Meo, Italy
Alberto Mezzetti, France
Claudio Minero, Italy
Edgar Moctezuma, Mexico
Thomas Moehl, Switzerland
Antoni Morawski, Poland
Franca Morazzoni, Italy
Fabrice Morlet-Savary, France
Mohammad Muneer, India
Ebinazar B. Namdas, Australia
Maria da Graça P. Neves, Portugal
Tebello Nyokong, South Africa
Tsuyoshi Ochiai, Japan
- Kei Ohkubo, Japan
Boris Orel, Slovenia
Leonidas Palilis, Greece
Leonardo Palmisano, Italy
Ravindra K. Pandey, USA
Thierry Pauporté, France
Pierre Pichat, France
Philippe Poggi, France
Gianluca Li Puma, UK
Tijana Rajh, USA
Peter Robertson, UK
Leonardo Sandrolini, Italy
Avigdor Scherz, Israel
Elena Selli, Italy
Jinn Kong Sheu, Taiwan
Panagiotis Smirniotis, USA
Bhushan Sopori, USA
Waldemar Stampor, Poland
Zofia Stasicka, Poland
Elias Stathatos, Greece
Jegadesan Subbiah, Australia
Velumani Subramaniam, Mexico
Meenakshisundaram Swaminathan, India
Mohamad-Ali Tehfe, Canada
K. R. Justin Thomas, India
Nikolai V. Tkachenko, Finland
Ahmad Umar, KSA
Thomas Unold, Germany
Veronica Vaida, USA
Roel van De Krol, Germany
Mark van Der Auweraer, Belgium
Rienk Van Grondelle, Netherlands
Wilfried G.J.H.M. Van Sark, Netherlands
Sergey Varlamov, Australia
Xuxu Wang, China
David Worrall, UK
Yanfa Yan, USA
Hongtao Yu, USA
Jiangbo Yu, USA
Klaas Zachariasse, Germany

Contents

Heterogeneous Photochemistry: Solar Energy Conversion and Environmental Remediation

Daniele Dondi, Sandra Babić, Irene Michael, Giovanni Palmisano, and Andrea Speltini

Volume 2016, Article ID 2083696, 1 page

Sorbents Coupled to Solar Light TiO₂-Based Photocatalysts for Olive Mill Wastewater Treatment

Andrea Speltini, Federica Maraschi, Michela Sturini, Valentina Caratto, Maurizio Ferretti, and Antonella Profumo

Volume 2016, Article ID 8793841, 7 pages

Photodegradation of 2,4-Dichlorophenol in Aqueous Systems under Simulated and Natural Sunlight

Dorota Gryglik, Marta Gmurek, Magdalena Foszpańczyk, and Stanisław Ledakowicz

Volume 2016, Article ID 9462098, 9 pages

Design and Performance Evaluation of a Solar Assisted Heat Pump Dryer Integrated with Biomass Furnace for Red Chili

M. Yahya

Volume 2016, Article ID 8763947, 14 pages

Flexible Bench-Scale Recirculating Flow CPC Photoreactor for Solar Photocatalytic Degradation of Methylene Blue Using Removable TiO₂ Immobilized on PET Sheets

Doaa M. EL-Mekkawi, Norhan Nady, Nourelhoda A. Abdelwahab, Walied A. A. Mohamed, and M. S. A. Abdel-Mottaleb

Volume 2016, Article ID 9270492, 9 pages

Noble Metal Decoration and Presulfation on TiO₂: Increased Photocatalytic Activity and Efficient Esterification of *n*-Butanol with Citric Acid

Yu Niu, Pan Huang, Fuying Li, Kai Yang, Jinbei Yang, Renzhang Wang, Cheng Lin, and Ting Qiu

Volume 2016, Article ID 4618924, 12 pages

Editorial

Heterogeneous Photochemistry: Solar Energy Conversion and Environmental Remediation

Daniele Dondi,¹ Sandra Babić,² Irene Michael,³ Giovanni Palmisano,⁴ and Andrea Speltini¹

¹*Department of Chemistry, University of Pavia, Viale Taramelli 12, 27100 Pavia, Italy*

²*Department of Analytical Chemistry, University of Zagreb, Marulićev Trg 20, 10000 Zagreb, Croatia*

³*Department of Civil and Environmental Engineering, University of Cyprus, Kallipoleos Street 75, 1678 Nicosia, Cyprus*

⁴*Department of Chemical and Environmental Engineering, Institute Center for Water and Environment (iWater), Masdar Institute of Science and Technology, P.O. Box 54224, Abu Dhabi, UAE*

Correspondence should be addressed to Daniele Dondi; daniele.dondi@unipv.it

Received 14 July 2016; Accepted 14 July 2016

Copyright © 2016 Daniele Dondi et al. This is an open access article distributed under the Creative Commons Attribution License, which permits unrestricted use, distribution, and reproduction in any medium, provided the original work is properly cited.

This special issue contains original research articles on solar energy use for green applications. In particular, the use of solar thermal energy for low environmental impact processes or the use of the light (with or without heterogeneous photocatalysts) for environmental remediation or synthesis was considered. The topic is highly challenging and the subject would be important, timely, and of great interest. Among the submitted manuscripts, 5 were selected as suitable for publication through the strict experts' peer reviews.

The papers to be published in this special issue are "Design and Performance Evaluation of a Solar Assisted Heat Pump Dryer Integrated with Biomass Furnace for Red Chili" for the direct solar light/thermal applications; "Sorbents Coupled to Solar Light TiO₂-Based Photocatalysts for Olive Mill Wastewater Treatment," "Photodegradation of 2,4-Dichlorophenol in Aqueous Systems under Simulated and Natural Sunlight," and "Flexible Bench-Scale Recirculating Flow CPC Photoreactor for Solar Photocatalytic Degradation of Methylene Blue Using Removable TiO₂ Immobilized on PET Sheets" for the photodegradation topic; and "Noble Metal Decoration and Presulfation on TiO₂: Increased Photocatalytic Activity and Efficient Esterification of n-Butanol with Citric Acid" for synthetic photochemistry.

We believe that this special issue can be interesting and inspiring for the readers of the journal since this advanced

interdisciplinary technology involves a wide range of subjects.

*Daniele Dondi
Sandra Babić
Irene Michael
Giovanni Palmisano
Andrea Speltini*

Research Article

Sorbents Coupled to Solar Light TiO₂-Based Photocatalysts for Olive Mill Wastewater Treatment

Andrea Speltini,¹ Federica Maraschi,¹ Michela Sturini,¹ Valentina Caratto,²
Maurizio Ferretti,² and Antonella Profumo¹

¹Department of Chemistry, University of Pavia, Via Taramelli 12, 27100 Pavia, Italy

²Department of Chemistry and Industrial Chemistry, University of Genoa, Via Dodecaneso 31, 16146 Genova, Italy

Correspondence should be addressed to Antonella Profumo; antonella.profumo@unipv.it

Received 24 February 2016; Accepted 30 June 2016

Academic Editor: Juan M. Coronado

Copyright © 2016 Andrea Speltini et al. This is an open access article distributed under the Creative Commons Attribution License, which permits unrestricted use, distribution, and reproduction in any medium, provided the original work is properly cited.

The aim of this work was to couple physical-chemical approaches with photocatalysis to reduce by a simple, inexpensive way the organic load of olive mill wastewater (OMW), mandatorily prior to the final discharge. Before irradiation, different sorbents were tested to remove part of the organic fraction, monitored by measuring chemical oxygen demand (COD) and polyphenols (PP). Different low-cost, safe materials were tested, that is, Y zeolite (ZY), montmorillonite, and sepiolite. Considerable decrease of organic load was obtained, with the highest abatement (40%) provided by ZY (10 g L⁻¹ in 1:10 OMW). Use of the three sorbents, in particular ZY, was convenient compared to commercial activated carbons. UV light photocatalytic tests, performed using P25 TiO₂ on ZY-treated OMW, yielded quantitative remediation (ca. 90%). Also solar light provided significant results, PP being lowered by 74% and COD by 56%. Sol-gel anatase TiO₂ and N-doped anatase TiO₂ were also tested, obtaining good results, around -80% PP and -40% COD. Finally, an integrated approach was experimented by ZY-supported anatase TiO₂ (TiO₂@ZY). This *photoreactive sorbent* allowed *one-pot* treatment of OMW significant abatements of PP (-77%) and COD (-39%) with only 1 g L⁻¹ material, under solar light.

1. Introduction

Olive mill wastewater (OMW) is a highly toxic effluent obtained from the extraction process of the olive oil industry and is considered an undesired waste. OMW represents a serious problem in the Mediterranean basin [1], as over 95% of the world production, estimated at more than 30 million m³ [2], occurs in Mediterranean countries and about 80% in the European Union, mainly Spain, Italy, and Greece [3]. It has been calculated that the volume of OMW coming from milling activity ranges from 0.5 to 1.5 m³ per ton of olives [3].

The OMW is a blackish liquid containing 80–83% of water (pH around 4.5), organic compounds ranging from 40 to 220 g L⁻¹ [2]. As expectable, the composition is variable and depends on many factors, namely, olive cultivar, extraction process, and climatic conditions, but always includes oil and grease, sugars, polyalcohols, pectins, lipids, and polyphenols

(PP) [4, 5]. Specifically, it has been reported that more than 30 phenolic compounds are present in OMW [6]. Beside lignin and tannins, the high content of phenolic species in a wide range of molecular weights is responsible for the typical black-brownish colour [4]. The dark colour of the OMW disturbs the sunlight absorption by photosynthetical organisms whereas the surface oil film prevents the oxygen absorption from air releasing an intense smell.

OMW is indeed considered a source of environmental pollution, due to the high levels of PP, persistent phytotoxic and antibacterial compounds that inhibit biodegradation. Due to the high content of phenols and long-chain fatty acids, high values of chemical oxygen demand (COD), up to 200 g L⁻¹, and biochemical oxygen demand (up to 100 g L⁻¹) are expected [3, 5]. Since these values may be found as hundreds of times higher than those of typical municipal sewage [7], it is clear that a direct discharge in receiving waters or soils is not possible because it would involve severe

effects, that is, ecotoxicity and eutrophication for natural water bodies.

Although the complex organic composition of OMW has been recently exploited to obtain “clean energy,” such as hydrogen gas [1, 3, 8], the actual major issue is the development of efficient, simple, and low environmental impact treatments for OMW before the final discharge.

Among the methods used for OMW treatment, physico-chemical treatments (i.e., settling, centrifugation, and filtration) coupled with adsorption on activated carbon have been practiced [9]. On the other side, the biological treatments, mainly consisting of anaerobic digestion [10], require large dilution factors or mandatory dephenolization procedures [11]. Advanced oxidation processes (AOPs) by ozonization [12] or photo-Fenton [5, 13–16] have been experimented, and integrated approaches involving flocculation/coagulation and/or adsorption, enzymatic, and biological treatments and photocatalysis have been proposed [5, 13–15, 17]. However, an environmentally safe and cost-effective solution to OMW treatment is still lacking [18].

Heterogeneous photocatalysis, requiring just a semiconductor and a light source, is a very promising, environmentally benign way to reduce the toxic organic load of OMW, as reported in some recent studies [14, 15, 17, 19, 20]. As for photo-Fenton applied to OMW [5], it seems convenient to design a sequential procedure combining pretreatment of the raw OMW, by adsorption onto high surface area sorbents, with a photocatalytic treatment and/or a biological step before the final discharge. As a matter of fact, photocatalysis is becoming increasingly attractive for environmental remediation [21], for instance, for abatement of emerging organic pollutants [22] or toxic metals [23], but also for OMW remediation [14, 15, 17, 19]. Owing to chemical stability, efficiency, low cost, and nontoxicity, titanium dioxide (TiO_2) is the most used photocatalyst, recently applied also for OMW remediation, after immobilization onto sepiolite [19]. However, to the authors' best knowledge, the application of N-doped TiO_2 or ZY-supported TiO_2 has not been reported in the literature for OMW treatment.

Based on this background, the aim of this work was to find out a simple and efficient procedure for the abatement of the organic load of OMW, in particular COD and PP levels. These were the two key parameters for evaluating the efficiency of the various treatments tested, that is, flocculation/coagulation, adsorption, and photocatalysis. Different high surface area materials were employed in the adsorption step, namely, Y zeolite (ZY), sepiolite (SEP), and montmorillonite (MMT), in addition to two commercially available activated carbons. After adsorption, OMW was submitted to photocatalytic treatment, under both UV and solar light. Different semiconductors were investigated, namely, anatase TiO_2 and N-doped anatase TiO_2 prepared by sol-gel method and characterized before use and commercial P25 TiO_2 . Finally, a hybrid material consisting of ZY-supported anatase TiO_2 combining sorption capacity and photocatalytic activity was prepared, characterized, and tested as *photoreactive sorbent* for the *one-pot* treatment of OMW, under solar light.

2. Experimental Procedure

2.1. Chemicals. $\text{AlCl}_3 \cdot 6\text{H}_2\text{O}$ (99%), $\text{Ca}(\text{OH})_2$ ($\geq 95\%$), cetylpyridinium bromide (CPB, 98%), Folin-Ciocalteu's phenol reagent (2N), gallic acid (98%) and Y zeolite (ZY), titanium (IV) tetraisopropoxide (97% v/v), and 2-propanol (99.5% v/v) were obtained from Sigma-Aldrich (Milan, Italy). $\text{Na}_2\text{CO}_3 \cdot 10\text{H}_2\text{O}$ (99.5%) was purchased from Carlo Erba Reagents (Milan, Italy) and Superfloc C 1598, a cationic emulsion polyacrylamide, from Kemira. AC20G (0.6–2.4 mm) and F-300 (0.8–1 mm) activated carbons were acquired from Puro-lite (Llantrisant, UK) and Chemviron Carbon Ltd. (Ashton-in-Makerfield, UK), respectively. SP-1 sepiolite (SEP, 50 grm/unit), Valdemoro, Spain (Miocene age, containing minor calcite), and Camontmorillonite STx-1 (MMT) were obtained from Clay Mineral Society; physical-chemical properties can be found at <http://www.clays.org/Sourceclays.html>. Evonik P25 TiO_2 (80% anatase, 20% rutile, particle size 30 nm, and surface area $50 \pm 15 \text{ m}^2 \text{ g}^{-1}$) was purchased from Evonik Industries AG (Hanau, Germany). Distilled water was produced in laboratory.

2.2. Olive Mill Wastewater. OMW was collected at the outlet of an olive mill located in Recco, near Genova (Italy). Samples were taken using PET containers and stored in the dark (-20°C). Before use, aliquots of each sample were mixed to obtain a homogeneous representative sample, submitted to centrifugation ($3 \times 10 \text{ min}$ at 4500 rpm, Sigma 2-16P Celbio Spa centrifuge) to remove suspended solids and oil residues [5]. The resulting matrix was then characterized having pH 5.1, conductivity at 20°C 8.21 mS cm^{-1} , COD $52500 (1530) \text{ mg L}^{-1} \text{ O}_2$, and total PP content $3444 (114) \text{ mg L}^{-1}$. These values, the mean of three replicates, are typical of OMW [5, 8, 14, 24]. The OMW sample was stored in the dark (4°C) and successively used to test the various chemical-physical and photocatalytic treatments.

2.3. Analytical Determinations. COD was determined before and after treatment according to the ISO 15705 protocol. The commercialized Hach Lange kit was used, working in the concentration interval $0\text{--}1000 \text{ mg L}^{-1} \text{ O}_2$. After incubation of the sample (2 h, 148°C , LT200 thermostat), COD quantification was performed by the standardized Hach Lange spectrophotometer (DR3900).

Total PP were determined according to the Folin-Ciocalteu method. A proper sample aliquot was placed in a 10 mL volumetric flask, and 0.5 mL of the Folin-Ciocalteu reagent was added, followed by 1 mL of Na_2CO_3 (20%, w/v), and made up to 10 mL with distilled water. The control sample (no OMW) was prepared separately. The flasks were allowed to stand for 1 h; then, spectrophotometric measurements were performed at 700 nm (UVmini-1240 Shimadzu Corporation). Quantification was carried out by external calibration analyzing gallic acid standard solutions in the concentration range $2\text{--}8 \text{ mg L}^{-1}$ (linearity $r^2 > 0.9975$, three independent calibration curves).

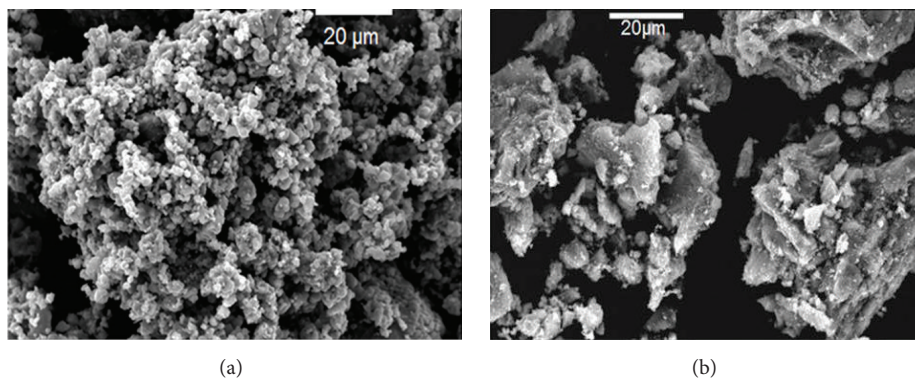


FIGURE 1: SEM images collected on anatase TiO_2 (a) and N-doped anatase TiO_2 (b).

2.4. Pretreatment by Chemical Reagents. To test the potential effect of coagulant/flocculant agents, 30 mL of centrifuged OMW was spiked with $30 \mu\text{L}$ of 1% w/v AlCl_3 solution and then the sample was basified (pH 8) by addition of 5% w/v $\text{Ca}(\text{OH})_2$ solution. Alternatively, the OMW sample was enriched with 0.5 g L^{-1} cationic organic polyelectrolyte. In both cases, the sample was maintained under magnetic stirring overnight and then centrifuged (20 min, 4500 rpm) and filtered (nylon membrane, $0.45 \mu\text{m}$) before COD and PP determination.

2.5. In-Batch Sorption Pretreatment. In the case of commercial granular activated carbons, batch sorption experiments were conducted on 30 mL OMW in the presence of $10/100 \text{ g L}^{-1}$ of each sorbent. The suspensions were shaken on a rotating plate (150 rpm) in polypropylene tubes, at room temperature for 24 h. The same procedure was followed in the case of ZY ($10\text{--}40 \text{ g L}^{-1}$), SEP, and MMT (10 g L^{-1}), using OMW (1:10). SEP was also tested after derivatization with CPB [25]. After equilibration, the suspensions were centrifuged (10 min, 4500 rpm) and then filtered by a nylon membrane ($0.45 \mu\text{m}$) before COD and PP determination.

2.6. Photocatalysts: Synthesis and Characterization. Beside the commercial P25 TiO_2 , other TiO_2 -based photocatalysts were tested. TiO_2 and N-doped TiO_2 have been synthesized by sol-gel process. According to previous work [26], titanium isopropoxide, isopropanol, and water have been used as precursors with the same concentrations reported changing the different solution to H_2O for TiO_2 and $\text{H}_2\text{O-NH}_3$ for TiO_2 doped nanoparticles.

$\text{TiO}_2@\text{ZY}$ has been synthesized according to Maraschi et al. [27]. The sample was obtained by magnetically stirring the resultant suspension of amorphous TiO_2 mixed with H^+ zeolite (2:1 w/w) in water. Powder was filtered, washed, and finally dried. Nominally, 1.5 g of the hybrid sample contains 1 g of nanometric TiO_2 .

The synthesized samples have been finally treated in a muffle furnace (Carbolite RHF1400) at 350°C for 1 hour to promote amorphous to anatase phase conversion.

The samples have been analyzed by X-ray powder diffraction (XRPD), scanning electron microscopy (SEM), diffuse

reflectance spectroscopy (DRS), and Brunauer-Emmett-Teller analysis (BET). Phase identification was performed by XRPD analysis using a Philips PW1830 diffractometer (Bragg-Brentano geometry; $\text{Cu K}\alpha$; Ni filtered; range $20\text{--}80 2\theta$; step $0.025 2\theta$; sampling time 10 s). SEM was performed using a Tescan Vega 3 XMV microscope on powders coated with gold in low vacuum. DRS was performed using a Perkin Elmer UV-Vis spectrophotometer LAMBDA 35 equipped with an integrating sphere. BET analysis was carried out using an ASAP 2010 physisorption analyzer (Micromeritics Instrument Corp). Before measurements, the samples were pretreated at 200°C in vacuum. Ar was used for ZY, while N_2 was used for all other materials.

2.7. Photocatalytic Irradiation. All the photocatalytic experiments were performed on 10 mL ZY-treated OMW (see Section 2.5) in the presence of 1 g L^{-1} of P25 TiO_2 , anatase TiO_2 , and anatase N- TiO_2 . For ZY-supported TiO_2 , any previous adsorption was done. Suspensions were irradiated (8 h) under UV light or simulated solar light. For UV irradiation, samples were placed in quartz tubes and treated under continuous air insufflation at 254 nm ($4 \times 15 \text{ W lamps}$) or 310 nm ($10 \times 15 \text{ W lamps}$). In the case of solar light, samples were placed in Pyrex glass containers and irradiated under magnetic stirring. A solar Box 1500e (CO.FO.ME.GRA S.r.l., Milan, Italy) set at a power factor of 500 W m^{-2} and equipped with a UV outdoor filter of soda lime glass IR treated was used as the solar light simulator. After photocatalysis, each sample was filtered and COD and PP concentrations were checked.

3. Results and Discussion

3.1. Characterization of the Prepared Photocatalysts. XRD spectra of TiO_2 , N-doped TiO_2 , and $\text{TiO}_2@\text{ZY}$ confirm the presence of anatase crystalline structure (Figure S1 in Supplementary Material available online at <http://dx.doi.org/10.1155/2016/8793841>). The SEM analysis shows the morphology of the samples. Undoped TiO_2 grains have rounded shape and form sponge-like aggregates (Figure 1(a)), while the N-doped ones form lamellar isolated aggregates (Figure 1(b)), in accordance with literature [26].

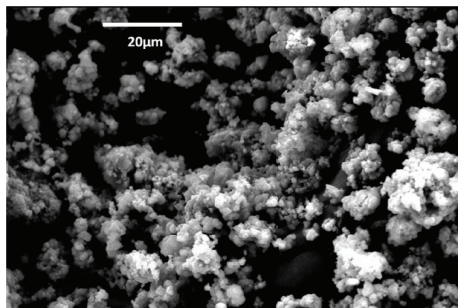


FIGURE 2: SEM image collected on the photoreactive sorbent anatase $\text{TiO}_2@ZY$.

TABLE 1: Values of absorption wavelength, energy gap, and BET surface area determined for each material.

Sample	Absorption wavelength (nm)	Energy gap (eV)	Surface area ($\text{m}^2 \text{g}^{-1}$)
Anatase TiO_2	384	3.2	120
N-doped anatase TiO_2	413	3.0	67
$\text{TiO}_2@ZY$	384	3.2	216
ZY	188	3.7	175

The TiO_2 nanoparticles supported by the zeolite are round shaped (Figure 2) and the sample is homogenous, as previously reported by Maraschi et al. [27]. The values of absorption wavelength, energy gap, and surface area of each material are reported in Table 1. It is apparent that N-doping yields a narrower band gap compared to anatase TiO_2 , although the latter shows a twofold higher surface area. The DRS spectra of doped and undoped TiO_2 are shown in the supplementary information (Figure S2). The E_{gap} calculation was made according to literature [26, 28]. The composite material, $\text{TiO}_2@ZY$, shows the highest surface area ($>200 \text{ m}^2 \text{ g}^{-1}$); the smaller energy gap and higher surface area compared to pristine ZY confirm the successful immobilization of the photocatalyst onto the zeolitic structure.

BET analyses are in agreement with the literature data [27].

3.2. OMW Treatment: Adsorption Coupled to Photocatalysis.

A first series of experiments was carried out to further reduce the suspended particles of the centrifuged OMW prior to the photocatalytic step, which is more efficient in limpid solution due to higher light penetration and lower scattering phenomena [14]. Since use of chitosan (0.4 g L^{-1}) before Fenton and photo-Fenton oxidation was reported [15], some experiments were performed in the presence of less expensive agents, either AlCl_3 (0.001%, v/v) under alkaline conditions (pH 8) or cationic organic polyelectrolyte (0.5 g L^{-1}), in order to test the potential effects of coagulation/flocculation in removing colloids ($<1 \mu\text{m}$). Results showed that both treatments yielded a COD abatement lower than 10%, whereas a 36% decrease of PP was observed using AlCl_3 , indicating that the sole

centrifugation is convenient for removing suspended organic matter.

To reduce the organic load of OMW, in-batch sorption was therefore exploited as a possible more efficient approach, investigated in the recent years for OMW treatment [5, 24, 29]. ZY, MMT, and SEP, largely available and low-cost materials characterized by high surface area, were selected as in principle they can operate in very complex matrices like OMW [5, 24, 29].

ZY (surface area $175 \text{ m}^2 \text{ g}^{-1}$) was tested in the concentration range $10\text{--}40 \text{ g L}^{-1}$, working at the sample native pH, and results are shown in Table 2.

COD and PP levels were substantially lowered after contact with ZY, indicating a strong affinity for the organic constituents of OMW. This is in accordance with literature data reporting on the use of zeolites for wastewater treatment [4, 29]. No significant improvement was seen in going from the lowest to the highest ZY concentration; thus, 10 g L^{-1} seemed convenient.

Despite the good results obtained, 1:10 diluted OMW was used for further experiments (see Table 3), in order to dispose of a final solution suitable for the photocatalytic treatment [15, 20]. Indeed, photocatalysis cannot operate satisfactorily in not diluted OMW, as later described and in agreement with literature [14]. The efficiency of ZY was then compared to clay powders, namely, SEP (surface area $213 \text{ m}^2 \text{ g}^{-1}$) and MMT (surface area $84 \text{ m}^2 \text{ g}^{-1}$), under the above reported conditions. These were tested because clays proved to be effective for purification of urban and industrial wastewater and have been recently employed also in the case of OMW [5, 29, 30].

As reported in Table 3, PP level dropped down by ca. 40% after adsorption onto SEP and MMT, similar to the case of ZY, and COD by ca. 30%.

With the aim of further improving ZY efficiency, the crude powder was derivatized with CPB, a cationic surfactant that could favour sorption of polyphenolic species [25]. However, no significant improvement in PP removal was observed using the CPB-derivatized material; thus, it was preferred to use the raw ZY.

Since activated carbon is the most used sorbent for water and wastewater purification, two types of granular activated carbon, specifically AC20G and F-300, were tested for comparison. Due to the large surface area ($>1000 \text{ m}^2 \text{ g}^{-1}$) and strong binding affinity of these materials for organic compounds, experiments were performed on not diluted OMW, using 100 g L^{-1} sorbent, and on 1:10 OMW with 10 g L^{-1} sorbent obtaining comparable results (see Tables 2 and 3).

Nevertheless, considering the results obtained by using the alternative sorbents (10 g L^{-1} , 1:10 OMW, Table 3) and their low cost compared to activated carbon, ZY proved to be a valid sorbent for OMW remediation and was therefore selected as the convenient adsorbent phase to treat OMW prior to the photocatalytic irradiation. Indeed, after ZY-contact, a biological step followed by an AOP treatment would be required to reach remediation of OMW, or as in this case, the treated OMW can be directly submitted to

TABLE 2: PP and COD values in OMW before and after adsorption onto ZY and activated carbons ($n = 3$).

Sample	PP (mg L ⁻¹)	Abatement (%)	COD (mg L ⁻¹ O ₂)	Abatement (%)
OMW	3444 (114)	—	52500 (1530)	—
OMW + ZY (10 g L ⁻¹)	2431 (170)	30 (5)	35900 (1424)	32 (3)
OMW + ZY (20 g L ⁻¹)	2189 (152)	37 (4)	32846 (1462)	37 (4)
OMW + ZY (40 g L ⁻¹)	1877 (150)	46 (4)	29300 (1568)	44 (3)
OMW + AC20G (100 g L ⁻¹)	617 (76)	82 (2)	18800 (1945)	64 (4)
OMW + F-300 (100 g L ⁻¹)	1130 (114)	67 (3)	22200 (2054)	58 (4)

TABLE 3: PP and COD values in 1:10 OMW before and after adsorption onto 10 g L⁻¹ ZY, CPB/ZY, SEP, MMT, and activated carbons ($n = 3$).

Sample	PP (mg L ⁻¹)	Abatement (%)	COD (mg L ⁻¹ O ₂)	Abatement (%)
1:10 OMW	335 (25)	—	5226 (330)	—
1:10 OMW + ZY (10 g L ⁻¹)	186 (21)	44 (6)	2640 (258)	36 (3)
1:10 OMW + CPB/ZY (10 g L ⁻¹)	194 (19)	42 (5)	2637 (247)	49 (4)
1:10 OMW + SEP (10 g L ⁻¹)	210 (17)	37 (5)	3685 (147)	29 (3)
1:10 OMW + MMT (10 g L ⁻¹)	209 (13)	38 (4)	3220 (161)	38 (3)
1:10 OMW + F-300 (10 g L ⁻¹)	111 (9)	77 (6)	2561 (237)	51 (5)
1:10 OMW + AC20G (10 g L ⁻¹)	121 (11)	74 (6)	2770 (232)	47 (4)

TABLE 4: PP and COD values in 1:10 OMW before and after photocatalytic treatment under UV and solar simulated light using P25 TiO₂ ($n = 3$).

Sample	PP (mg L ⁻¹)	Abatement (%)	COD (mg L ⁻¹ O ₂)	Abatement (%)
1:10 OMW	335 (25)	—	5226 (330)	—
1:10 OMW + ZY (10 g L ⁻¹)	186 (21)	44 (6)	2640 (258)	36 (3)
1:10 OMW + ZY (10 g L ⁻¹) + P25 TiO ₂ (254 nm) ^a	21 (3)	94 (1)	490 (39)	91 (1)
1:10 OMW + ZY (10 g L ⁻¹) + P25 TiO ₂ (310 nm) ^a	31 (4)	91 (1)	775 (54)	85 (1)
1:10 OMW + ZY (10 g L ⁻¹) + P25 TiO ₂ (solar box) ^a	87 (7)	74 (5)	1585 (127)	56 (2)

^a1 g L⁻¹ photocatalyst, 8 h irradiation.

photocatalysis. This was investigated under either UV or solar simulated light, using commercial P25 TiO₂ and sol-gel anatase TiO₂ and N-doped anatase TiO₂, the two latter not being previously investigated for OMW.

Irradiation in presence of the former semiconductor led to quantitative abatements, around 90%, working under UV light. Interesting data were found also under solar simulated irradiation, with COD and PP decrease of 56% and 74%, correspondingly (see Table 4).

Notice that the adsorption step prior to photocatalysis is of great importance in allowing a successful remediation of OMW. Indeed, direct photocatalytic treatment on 1:10 OMW (not contacted with ZY) led to a COD abatement of just 20% even under drastic conditions (254 nm, 8 h radiation). On the other hand, irradiation of not diluted OMW after ZY-adsorption was as well unsuccessful. As shown in UV-Vis spectra of OMW samples (see Figure S3, Supplementary Materials), the sorption step on ZY is convenient not only for PP/COD abatement, but also to favour light penetration by decreasing the sample absorbance (ca. 20%).

These findings support the actual reports on TiO₂ photocatalytic treatment of OMW, requiring a diluted sample [14, 15, 17]. Nevertheless, dilution can be avoided in the case of photo-Fenton, but the additional costs due to the use of

oxidizing reagents and necessity to adjust pH have to be taken into account [13, 14, 16]. Besides, since photo-Fenton was shown to preserve or even increase the OMW effluent toxicity, a successive biotreatment that would be required to further reduce COD and phenols could be hampered [16].

The adsorption-photocatalysis combined treatment on 1:10 OMW presented here is convenient and efficient, as the PP content was reduced to ca. 20 mg L⁻¹, and COD was lowered below the limit (500 mg L⁻¹) indicated by the actual Italian legislation for wastewater discharge. The above results were substantiated by control experiments performed to evaluate the role of direct photolysis that is in the absence of catalyst, under the same conditions. COD and PP reduction being lower than 10%, except in the case of 254 nm for PP (-29%), these findings absolutely attest the great contribution of the photocatalyst in degrading OMW organics.

In the framework of the photochemical step, a part of the work was undertaken to strengthen the possibility of working under solar light and, with this aim, N-doped anatase TiO₂ was tested, compared to anatase TiO₂ as the control sample. Indeed, the absorption edge of P25 TiO₂ is around 390 nm, in relation to its band gap of 3–3.2 eV; thus, just the 5% of the solar light spectrum can be exploited for the activation of the semiconductor. Differently, a red-shift absorption of TiO₂

TABLE 5: PP and COD values in 1:10 OMW before and after photocatalytic treatment under solar simulated light using different TiO₂-based photocatalysts ($n = 3$).

Sample	PP (mg L ⁻¹)	Abatement (%)	COD (mg L ⁻¹ O ₂)	Abatement (%)
1:10 OMW	335 (25)	—	5226 (330)	—
1:10 OMW + ZY (10 g L ⁻¹)	186 (21)	44 (6)	2640 (258)	36 (3)
1:10 OMW + ZY (10 g L ⁻¹) + P25 TiO ₂ ^a	87 (7)	74 (5)	1585 (127)	56 (2)
1:10 OMW + ZY (10 g L ⁻¹) + anatase TiO ₂ ^a	54 (5)	84 (6)	3031	42 (3)
1:10 OMW + ZY (10 g L ⁻¹) + N-doped anatase TiO ₂ ^a	74 (6)	78 (4)	3188	39 (3)
1:10 OMW + TiO ₂ @ZY ^a	77 (6)	77 (3)	3170 (224)	39 (3)

^a1 g L⁻¹ photocatalyst, 8 h irradiation.

can be achieved after derivatization or doping [31]. Despite the narrower band gap obtained after N-doping (3.0 eV), the efficiency in degrading OMW organics was comparable to anatase TiO₂ (band gap 3.2 eV), as shown in Table 5.

This is reasonably attributable to the lower surface area of the N-doped particles that could be improved with further optimization of the synthesis. Anyway, as apparent from Table 5, both sol-gel semiconductors are attractive under solar light compared to commercial P25 TiO₂.

Further experiments were planned using a hybrid material able to join sorption capability and photocatalytic activity, that is, TiO₂@ZY. As shown in Table 5, TiO₂@ZY proved to be greatly advantageous because it allowed the same efficiency in terms of PP/COD abatement, compared to the sequential treatment entailing adsorption on ZY and photocatalytic steps. Use of this sorbent/photoreactive material provides those similar satisfying results by one-pot treatment and tenfold lower amount of material.

The overall abatement is indeed due to the sorption capacity of this composite (49% PP and 29% COD) combined with the photocatalytic properties (further abatement 28% PP and 10% COD). This behavior can be certainly explained by considering the physical-chemical properties of the composite. Indeed, among the many factors that may influence the photocatalytic activity, namely, crystal structure, energy gap, and surface area, TiO₂@ZY presents as well greater surface area with respect to pristine zeolite, anatase TiO₂, and N-doped TiO₂, due to the smaller regular dimension of grains combined with the high surface area of ZY.

4. Conclusions

A simple, working procedure for OMW treatment prior to final discharge, entailing adsorption onto Y zeolite followed by TiO₂ photocatalysis, is described here. The first step allowed relevant abatement of the organic load of OMW due to adsorption onto ZY, a largely available and costless material, providing an intermediated sample suitable to be submitted to photocatalytic treatment. This was studied under both UV and simulated solar light, in presence of various TiO₂-based photocatalysts, namely, commercial P25, sol-gel anatase, and sol-gel N-doped anatase TiO₂. Photocatalysis proved to degrade substantially OMW organic constituents, leading to a COD < 500 mg L⁻¹ and PP around 20 mg L⁻¹ in the final water. Considerable remediation was gained

also under simulated sunlight. As a remarkable advantage, a hybrid material made of ZY-supported anatase TiO₂ was for the first time applied for the *one-pot* treatment of OMW, under solar light. This material, combining solar light photocatalytic activity with sorption capacity, proved to be greatly advantageous in terms of efficiency, cost, ease of separation after use, and time-consumption.

Competing Interests

The authors declare that they have no competing interests.

Acknowledgments

The authors want to thank Dr. Alessandro Alloni for experimental support during his graduation thesis.

References

- [1] C. Pintucci, A. Giovannelli, M. L. Traversi, A. Ena, G. Padovani, and P. Carozzi, "Fresh olive mill waste deprived of polyphenols as feedstock for hydrogen photo-production by means of *Rhodospseudomonas palustris* 42OL," *Renewable Energy*, vol. 51, pp. 358–363, 2013.
- [2] I. Ntaikou, C. Kourmentza, E. C. Koutrouli et al., "Exploitation of olive oil mill wastewater for combined biohydrogen and biopolymers production," *Bioresource Technology*, vol. 100, no. 15, pp. 3724–3730, 2009.
- [3] S. Tosti, C. Accetta, M. Fabbicino, M. Sansovini, and L. Pontoni, "Reforming of olive mill wastewater through a Pd-membrane reactor," *International Journal of Hydrogen Energy*, vol. 38, no. 25, pp. 10252–10259, 2013.
- [4] G. Padovani, C. Pintucci, and P. Carozzi, "Dephenolization of stored olive-mill wastewater, using four different adsorbing matrices to attain a low-cost feedstock for hydrogen photo-production," *Bioresource Technology*, vol. 138, pp. 172–179, 2013.
- [5] P. Aytar, S. Gedikli, M. Sam, B. Farizoğlu, and A. Çabuk, "Sequential treatment of olive oil mill wastewater with adsorption and biological and photo-Fenton oxidation," *Environmental Science and Pollution Research*, vol. 20, no. 5, pp. 3060–3067, 2013.
- [6] E. De Marco, M. Savarese, A. Paduano, and R. Sacchi, "Characterization and fractionation of phenolic compounds extracted from olive oil mill wastewaters," *Food Chemistry*, vol. 104, no. 2, pp. 858–867, 2007.
- [7] L. Saez, J. Perez, and J. Martinez, "Low molecular weight phenolics attenuation during simulated treatment of wastewaters

- from olive oil mills in evaporation ponds,” *Water Research*, vol. 26, no. 9, pp. 1261–1266, 1992.
- [8] A. Speltini, M. Sturini, F. Maraschi et al., “Evaluation of UV-A and solar light photocatalytic hydrogen gas evolution from olive mill wastewater,” *International Journal of Hydrogen Energy*, vol. 40, no. 12, pp. 4303–4310, 2015.
- [9] M. O. J. Azzam, K. I. Al-Malah, and N. I. Abu-Lail, “Dynamic post-treatment response of olive mill effluent wastewater using activated carbon,” *Journal of Environmental Science and Health A*, vol. 39, no. 1, pp. 269–280, 2004.
- [10] C. C. Anastasiou, P. Christou, A. Michael, D. Nicolaidis, and T. P. Lambrou, “Approaches to olive mill wastewater treatment and disposal in Cyprus,” *Environmental Research Journal*, vol. 5, pp. 49–58, 2011.
- [11] P. S. Blika, K. Stamatelidou, M. Kornados, and G. Lyberatos, “Anaerobic digestion of olive mill wastewater,” *Global NEST Journal*, vol. 11, pp. 364–372, 2009.
- [12] R. C. Martins, A. M. Ferreira, L. M. Gando-Ferreira, and R. M. Quinta-Ferreira, “Ozonation and ultrafiltration for the treatment of olive mill wastewaters: effect of key operating conditions and integration schemes,” *Environmental Science and Pollution Research*, vol. 22, no. 20, pp. 15587–15597, 2015.
- [13] P. Canepa, F. Cauglia, P. Caviglia, and E. Chelossi, “Photo-Fenton oxidation of oil mill waste water: chemical degradation and biodegradability increase,” *Environmental Science and Pollution Research*, vol. 10, no. 4, pp. 217–220, 2003.
- [14] W. Gernjak, M. L. Maldonado, S. Malato et al., “Pilot-plant treatment of olive mill wastewater (OMW) by solar TiO₂ photocatalysis and solar photo-Fenton,” *Solar Energy*, vol. 77, no. 5, pp. 567–572, 2004.
- [15] L. Rizzo, G. Lofrano, M. Grassi, and V. Belgiorno, “Pre-treatment of olive mill wastewater by chitosan coagulation and advanced oxidation processes,” *Separation and Purification Technology*, vol. 63, no. 3, pp. 648–653, 2008.
- [16] C. I. Justino, K. Duarte, F. Loureiro et al., “Toxicity and organic content characterization of olive oil mill wastewater undergoing a sequential treatment with fungi and photo-Fenton oxidation,” *Journal of Hazardous Materials*, vol. 172, no. 2-3, pp. 1560–1572, 2009.
- [17] M. I. Badawy, F. E. Gohary, M. Y. Ghaly, and M. E. M. Ali, “Enhancement of olive mill wastewater biodegradation by homogeneous and heterogeneous photocatalytic oxidation,” *Journal of Hazardous Materials*, vol. 169, no. 1–3, pp. 673–679, 2009.
- [18] D. P. Zagklis, E. C. Arvaniti, V. P. Papadakis, and C. A. Paraskeva, “Sustainability analysis and benchmarking of olive mill wastewater treatment methods,” *Journal of Chemical Technology and Biotechnology*, vol. 88, no. 5, pp. 742–750, 2013.
- [19] M. Uğurlu and M. H. Karaoğlu, “TiO₂ supported on sepiolite: preparation, structural and thermal characterization and catalytic behaviour in photocatalytic treatment of phenol and lignin from olive mill wastewater,” *Chemical Engineering Journal*, vol. 166, no. 3, pp. 859–867, 2011.
- [20] E. Martini, M. Tomassetti, and L. Campanella, “Monitoring photocatalytic treatment of olive mill wastewater (OMW) in batch photoreactor using a tyrosinase biosensor and COD test,” in *Sensors and Microsystems*, vol. 268 of *Lecture Notes in Electrical Engineering*, pp. 169–173, Springer, 2014.
- [21] G. Rammohan and M. N. Nadagouda, “Green photocatalysis for degradation of organic contaminants: a review,” *Current Organic Chemistry*, vol. 17, no. 20, pp. 2338–2348, 2013.
- [22] M. Sturini, A. Speltini, F. Maraschi et al., “Photolytic and photocatalytic degradation of fluoroquinolones in untreated river water under natural sunlight,” *Applied Catalysis B: Environmental*, vol. 119–120, pp. 32–39, 2012.
- [23] M. Sturini, E. Rivagli, F. Maraschi, A. Speltini, A. Profumo, and A. Albini, “Photocatalytic reduction of vanadium(V) in TiO₂ suspension: chemometric optimization and application to wastewaters,” *Journal of Hazardous Materials*, vol. 254–255, no. 1, pp. 179–184, 2013.
- [24] A. A. Aly, Y. N. Y. Hasan, and A. S. Al-Farraj, “Olive mill wastewater treatment using a simple zeolite-based low-cost method,” *Journal of Environmental Management*, vol. 145, pp. 341–348, 2014.
- [25] J. Lin, Y. Zhan, Z. Zhu, and Y. Xing, “Adsorption of tannic acid from aqueous solution onto surfactant-modified zeolite,” *Journal of Hazardous Materials*, vol. 193, pp. 102–111, 2011.
- [26] V. Caratto, L. Setti, S. Campodonico, M. M. Carnasciali, R. Botter, and M. Ferretti, “Synthesis and characterization of nitrogen-doped TiO₂ nanoparticles prepared by sol-gel method,” *Journal of Sol-Gel Science and Technology*, vol. 63, no. 1, pp. 16–22, 2012.
- [27] F. Maraschi, M. Sturini, A. Speltini et al., “TiO₂-modified zeolites for fluoroquinolones removal from wastewaters and reuse after solar light regeneration,” *Journal of Environmental Chemical Engineering*, vol. 2, no. 4, pp. 2170–2176, 2014.
- [28] R. Asahi, T. Morikawa, T. Ohwaki, K. Aoki, and Y. Taga, “Visible-light photocatalysis in nitrogen-doped titanium oxides,” *Science*, vol. 293, no. 5528, pp. 269–271, 2001.
- [29] C. A. Santi, S. Cortes, L. P. D’Acqui, E. Sparvoli, and B. Pushparaj, “Reduction of organic pollutants in Olive Mill Wastewater by using different mineral substrates as adsorbents,” *Bioresource Technology*, vol. 99, no. 6, pp. 1945–1951, 2008.
- [30] E. Eroğlu, I. Eroğlu, U. Gündüz, and M. Yücel, “Effect of clay pretreatment on photofermentative hydrogen production from olive mill wastewater,” *Bioresource Technology*, vol. 99, no. 15, pp. 6799–6808, 2008.
- [31] V. Etacheri, C. Di Valentin, J. Schneider, D. Bahnemann, and S. C. Pillai, “Visible-light activation of TiO₂ photocatalysts: advances in theory and experiments,” *Journal of Photochemistry and Photobiology C: Photochemistry Reviews*, vol. 25, pp. 1–29, 2015.

Research Article

Photodegradation of 2,4-Dichlorophenol in Aqueous Systems under Simulated and Natural Sunlight

Dorota Gryglik,¹ Marta Gmurek,² Magdalena Foszpańczyk,² and Stanisław Ledakowicz²

¹Faculty of Civil Engineering, Architecture and Environmental Engineering, Lodz University of Technology, Aleja Politechniki 6, 90-924 Lodz, Poland

²Faculty of Process and Environmental Engineering, Lodz University of Technology, Ulica Wólczajska 213, 90-924 Lodz, Poland

Correspondence should be addressed to Dorota Gryglik; dorota.gryglik@p.lodz.pl

Received 26 February 2016; Revised 23 April 2016; Accepted 4 May 2016

Academic Editor: Irene Michael

Copyright © 2016 Dorota Gryglik et al. This is an open access article distributed under the Creative Commons Attribution License, which permits unrestricted use, distribution, and reproduction in any medium, provided the original work is properly cited.

The work presents results of studies on 2,4-dichlorophenol (2,4-DCP) degradation in aqueous solutions using photochemically initiated processes by simulated and natural sunlight. A number of possible substrate photodegradation routes were investigated, by both direct photolysis and photosensitized oxidation process. The major role of singlet oxygen in 2,4-DCP photodegradation was proved. Rose Bengal and derivatives of porphine and phthalocyanine were used as sensitizers. The influences of various process parameters on the reaction rate were investigated. On the basis of experimental data reaction rate constants of 2,4-DCP photosensitized oxidation were determined. The possibility of using natural sunlight to degrade 2,4-DCP in water in the middle latitudes was stated. The acute toxicity bioassay was conducted with the marine bacterium *Vibrio fischeri* as a bioluminescent indicator. The obtained results encourage further research on this process.

1. Introduction

The pollution of aquatic environment by trace amounts of anthropogenic chemical substances has a hazardous impact on the regular development of plants and animals as well as on the human health [1]. Dichlorophenols are widely used in organic synthesis for the production of pharmaceuticals, disinfectants, preservatives, insecticides, fungicides, and herbicides [2]. They are attractive initial substrates which are used in industry, for example, for the production of higher chlorophenols [3]. 2,4-Dichlorophenol (2,4-DCP) is a compound characterized by high toxicity to living organisms so even the small amount released into the environment can pose serious consequences [4, 5]. It is well known that very low levels of chlorophenols in water cause significant deterioration of its taste and smell. Contamination by 2,4-DCP in environment may occur as a result of degradation of herbicides, for example, 2,4-dichlorophenyl-p-nitrophenyl ether, from chlorination of drinking water and industrial and municipal waste water by water disinfection plants or from agricultural runoff or industrial waste discharges [2, 6, 7].

2,4-DCP has also been reported to be an endocrine disruptor [8]. Thus, it is important to protect the environment from the harmful effects of its presence. Unfortunately, the conventional treatment methods are not able to degrade these xenobiotics efficiently.

Recently the use of advanced oxidation processes using different chemical and photochemical processes for the purification of wastewater or water treatment has become very popular. The main mechanism of compound degradation by these methods is the hydroxyl radical generation and utilization. Thus, they are very effective in removing micropollutants (also microorganisms) present in the wastewater, especially when these are found in low concentrations [9, 10]. Moreover, among the photochemical routes of many xenobiotics degradation the most popular one is solar photocatalytic irradiation of the substrate in the presence of TiO₂ as a catalyst [11]. There are reports in this topic concerning 2,4-DCP degradation [12, 13]. However, in many cases, advanced oxidation processes have limited practical applications due to high cost and energy consumption and so forth.

An alternative process seems to be the photosensitized oxidation process, particularly using molecular oxygen. It involves the absorption of the visible light energy by the photosensitizer to bring it to a reactive excitation state, transferring its excitation energy to the surrounding molecules. It can occur according to two different photochemical mechanisms: type I (as electron or hydrogen atom transfer), type II photooxidation (as energy transfer to the oxygen molecule and generating reactive singlet oxygen form), or a combination of both. The domination of any of these mechanisms is dependent on many factors including the nature of the substrate and of the sensitizer and the properties of their microenvironment. Thus, the sensitizer acts here, in principle, as a specific kind of catalyst which enables the reaction to occur while remaining unchanged itself.

It is important to note that in this process the photosensitizer may be used in homogeneous solution or may be immobilized on various kinds of carriers [14, 15]. The use of a soluble form of the sensitizer is faster, simpler, and cheaper. However, it is associated with the introduction of a new component to the solution. It is, in fact, an additional "pollution" introduced into the water which may have itself more toxic properties or the products of its decomposition may be, for example, more toxic and so forth. Thus, by purifying the water environment it can cause unwanted damage the consequences of which can be unpredictable. The use of the sensitizer in the immobilized form can avoid the aforementioned drawbacks because it is easily separated after the reaction. Its additional useful and valuable quality is that it could be reused. Unfortunately, the use of the dye in the immobilized form is usually more difficult to implement, definitely more time-consuming, and generally more expensive.

Herein we present results of photooxidation of 2,4-dichlorophenol under simulated and natural sunlight via singlet oxygen generated by various excited photosensitizers in homogeneous solutions. The objective is to define the conditions that maximize the rate of photosensitized degradation of 2,4-DCP in the aquatic solution, to determine the kinetic constants, and to compare the photodegradation rate under simulated and natural sunlight.

2. Materials and Methods

All chemicals were commercially available products. The model pollutant 2,4-dichlorophenol ($\geq 99\%$) was purchased from Aldrich. Sodium azide (NaN_3) and *tert*-butanol (*t*-BuOH) were purchased from Fluka and superoxide dismutase (SOD) was purchased from Sigma Aldrich.

The pH of mixtures during experiments was maintained stable using a buffer solution (according to Britton-Robinson). All buffer reagents H_3PO_4 , H_3BO_3 , CH_3COOH , and NaOH were p.a. quality (POCH, Poland). Samples for chromatographic analysis were acidified with 0.5 M phosphoric(V) acid (p.a. POCH, Gliwice).

All reaction solutions were prepared in distilled water (Millipore Milli-Q Plus System, 18.2 M Ω).

2.1. The Sensitizers. The following dyes were used as photosensitizers:

- (i) Rose Bengal, RB, was purchased from Fluka;
- (ii) aluminum(III) phthalocyanine chloride tetrasulfonic acid, AlPcS₄, was purchased from Frontier Scientific Inc. (Logan, USA);
- (iii) mesotetrasulphonato phenyl porphyrin, TPPS₄, was purchased from Fluka (Steinheim, Germany);
- (iv) zinc(II) phthalocyanine tetrasulfonate tetrasodium salt, ZnPcS₄, was purchased from Frontier Scientific Inc. (Logan, USA).

The important physicochemical properties of the dyes which allow them to act as efficient photosensitizers (PS) are presented in Table 1.

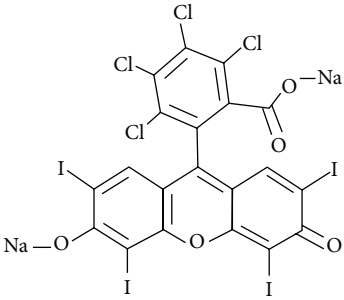
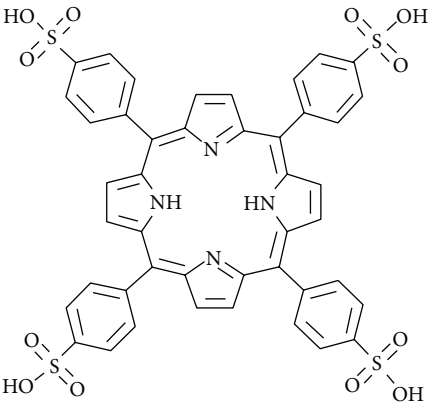
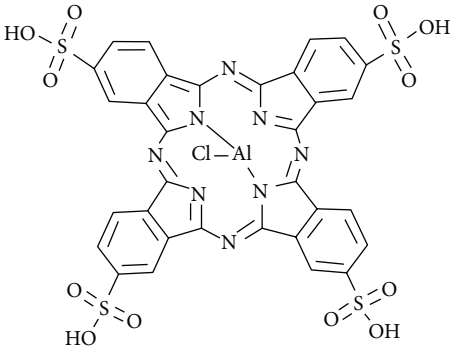
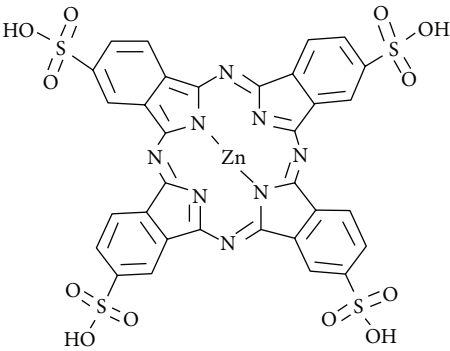
2.2. Lamp Irradiation Setup. The experiments were conducted in a semicontinuous system in flat reactors (0.06×0.10 m) of the volume of 0.01 dm^3 each one. Five reactors were symmetrically positioned around the xenon lamp (Osram 100 W, $E_0 = 324 \mu\text{Einstein s}^{-1} \text{ dm}^{-3}$), simulating solar radiation. The quantity of absorbed photons was calculated using Reinecke's actinometer for wavelengths ranging from 310 nm to 770 nm. The reaction mixture in each reactor was agitated by gentle air or oxygen stream. The initial concentration of 2,4-DCP was equal to 2×10^{-4} M and the sensitizers (RB, TPPS₄, AlPcS₄, and ZnPcS₄) were used at initial concentration equals 2×10^{-5} M.

2.3. Sunlight Irradiation Setup. The photochemical experimental setup with natural sunlight consisted of a glass reactor with a cooling jacket, equipped with a porous plate to deliver air into the reaction solution. Experiments were carried out in a semibatch mode. The volume of mixture was equal to 0.5 dm^3 and it was buffered to maintain constant pH during irradiation. Experiments were performed always at the same time of the day (between 10 a.m. and 2 p.m.) at various atmospheric conditions. The spectrum of light was collected with an Oceans Optics USB 4000 fiber optic spectrometer with an approximate resolution of 0.4 nm.

2.4. Analysis. The 2,4-DCP decay was monitored by HPLC (Waters) equipped with a UV diode array detector and a Nova-Pak 150/C18 column. The wavelength for the UV detection of 2,4-DCP was equal to 284 nm. A mixture of methanol and acidified water (0.01% H_3PO_4) was used as an eluent (70 : 30 vol./vol.) at the constant flow rate equal to 0.7 mL min^{-1} .

The acute toxicity bioassay was conducted using a Microtox® Model 500 analyzer (Modern Water, New Castle, DE, USA) with the marine bacterium *Vibrio fischeri* as a bioluminescent indicator. The Microtox 81.9% screening test and the 81.9% basic test protocols available with the MicrotoxOmni™ analyzer software were used for the toxicity assessment of the samples. The decrease in bacteria activity as function of the luminescence was measured after 15 minutes of exposure. The evaluation of the acute toxicity toward *V. fischeri* was presented as inhibition of the luminescence (screening test) as well as the standard index, median of the effective concentration (EC₅₀).

TABLE 1: The physicochemical properties of the dyes used in experiments [16–20].

PS	Structure	φ_{Δ}	φ_T
RB		0.76	0.98
TPPS ₄		0.62	0.78
AlPcS ₄		0.34	0.44
ZnPcS ₄		0.32	0.56

φ_{Δ} : singlet oxygen quantum yield; φ_T : photosensitizer triplet quantum yield.

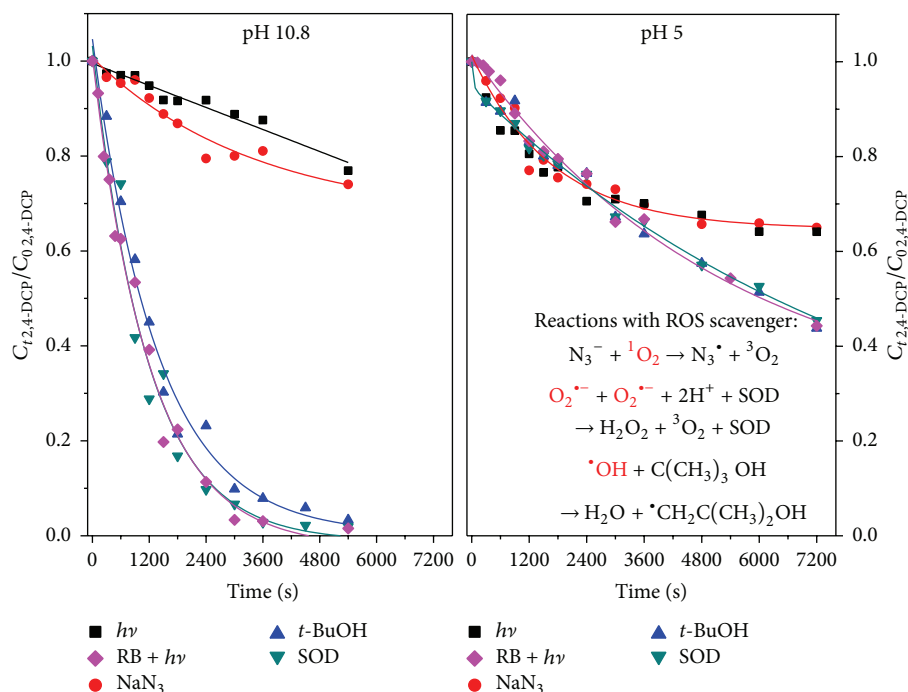


FIGURE 1: The dependence of 2,4-DCP relative concentrations decay on pH of reaction solution and presence of various ROS scavengers ($C_{0,2,4-DCP} = 2.4 \times 10^{-4}$ M, $C_{0,RB} = 2 \times 10^{-5}$ M, $C_{0,NaN_3} = 2.4 \times 10^{-4}$ M, $C_{0,t-BuOH} = 2.4 \times 10^{-4}$ M, $C_{0,SOD} = 2.4 \times 10^{-4}$ M, air bubbling, and xenon lamp irradiation).

3. Results and Discussion

3.1. Lamp Irradiation. In our previous experiments a large dependence of the sensitized oxidation reaction rate on pH of reaction mixture has been found. It is probably connected with pH-dependent degree of compound dissociation [14, 21]. Irradiation of 2,4-DCP in the presence of oxygen and a sensitizer confirmed these observations. It seems that the substrate degradation is fastest in taking place in alkaline solutions and the acidic medium does not increase the rate of the reaction. As shown in Figure 1 in pH 10.8 the 2,4-DCP concentration disappears after approx. 90 minutes of exposure in the presence of RB and air. At the same time in solution at pH 5 the concentration of 2,4-DCP disappears only approx. 45% relative to its initial value.

Following irradiation of 2,4-DCP by xenon lamp in the absence of the dye compound we recognized that the direct photolysis process is responsible for the disappearance of the substrate in about 20% (Figure 1).

To fully characterize the photosensitized oxidation of 2,4-DCP we have to take into account as much as possible reactions which can occur during irradiation of the solution in the presence of sensitizer and oxygen. It is well known that during photosensitized oxidation process also other *reactive oxygen species* (ROS) are produced such as the oxygen anion-radical ($O_2^{\bullet-}$) or the hydroxyl radical ($\bullet OH$). Therefore the special additives were added to the reaction solution to explain which way the reaction is undergoing. First the irradiation was conducted in the presence of 1O_2 scavenger, sodium

azide (NaN_3). The results of this experiment are presented in Figure 1. Evidently the reaction was stopped at photolysis level when NaN_3 was used. It suggests that the only reactive oxygen species present in the system are molecules of singlet oxygen and only they are responsible for degradation of the compound. To prove this hypothesis further experiments were carried out with addition of the $\bullet OH$ scavenger *tert*-butanol (*t*-BuOH) and superoxide dismutase (SOD) which removes $O_2^{\bullet-}$. In this case, the results are quite different: the presence of *t*-BuOH in the solution has little effect on slowing down reaction, while SOD has almost no influence on the course of the reaction, which only confirms our assumption.

Three factors must coexist in solution for the occurrence of photosensitized oxidation of a substrate: light, oxygen, and sensitizer. In the next series of experiments we tested whether the oxygen presence/concentration in the solution and type of photosensitizer really affect the reaction progress. As can be seen in Figure 2 the higher the concentration of oxygen in the solution is, the faster the 2,4-DCP concentration decreases.

As can be seen in Figure 2 the decay of 2,4-DCP is 3 times faster when pure oxygen was used. It should be noted that when the reaction solution was not bubbled (any oxygen was delivered), the reaction was inhibited. When the soluble oxygen was consumed the reaction was stopped.

In Figure 3, the influence of the photosensitizer is presented. In the optimum conditions, in which the decay rate of the substrate was fastest, the irradiations were carried out in the presence of various sensitizers. The best results

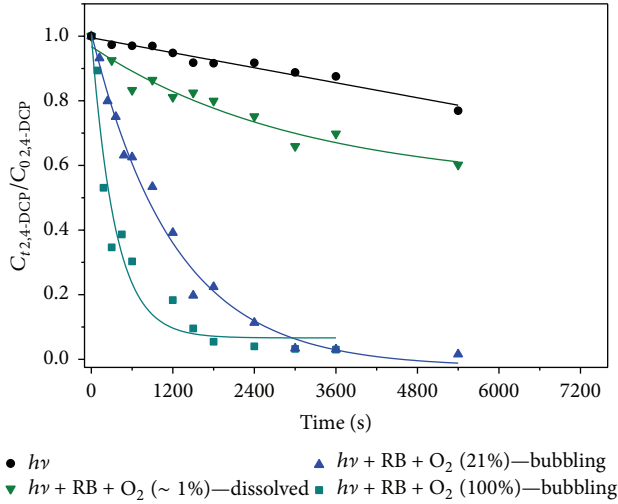


FIGURE 2: The dependence of 2,4-DCP relative concentrations decay on the concentrations of oxygen in the system ($C_{0,2,4-DCP} = 2.4 \times 10^{-4}$ M, $C_{0,RB} = 2 \times 10^{-5}$ M, pH = 10.8, and xenon lamp irradiation).

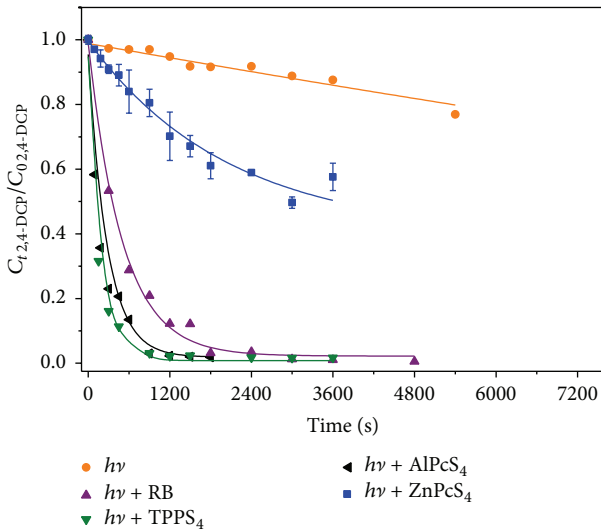


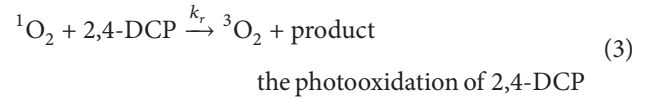
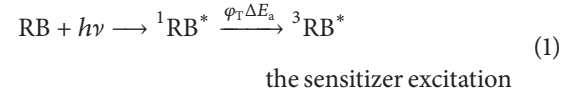
FIGURE 3: The dependence of 2,4-DCP relative concentrations decay on the type of used photosensitizer ($C_{0,2,4-DCP} = 2.4 \times 10^{-4}$ M, $C_{0,sens.} = 2 \times 10^{-5}$ M, pH = 10.8, oxygen bubbling, and xenon lamp irradiation).

were achieved for TPPS₄ while the slowest reaction progress was observed for ZnPcS₄. These results have not really confirmed any theoretical suppositions we could pull out on the basis of singlet oxygen quantum yields (φ_{Δ}) and triplet quantum yields (φ_T) of each sensitizer (Table 1). There are no explicit interactions between these values (which indicate the theoretical ability to generate singlet oxygen) and effectiveness of the dye as specific catalysts in photosensitized oxidation of 2,4-DCP. Interpretation of such results is difficult and additional research is required to fully understand the nature of this phenomenon.

TABLE 2: Determined constant values (mean) of pH dependence of the reaction.

Constant of reaction ($M^{-1} s^{-1}$)	pH 5	pH 10.8
k_r	1.65×10^6	3.64×10^7
k_t	1.05×10^8	4.95×10^8

3.2. *Kinetic Model.* We have tried to establish the kinetics of the 2,4-DCP photodegradation process. We have assumed that the following reactions occur during photosensitized oxidation of 2,4-DCP using RB as photosensitizer:



where $k_{\Delta}^{O_2}$ is rate constant for triplet RB reaction with oxygen resulting in 1O_2 , $M^{-1} s^{-1}$; k_r is rate constant for chemical reaction of singlet oxygen with 2,4-DCP, $M^{-1} s^{-1}$; E_a is flux of absorbed photon per unit of the reaction volume, $E s^{-1} dm^{-3}$.

The results shown in Figure 1 allow us to suppose that the main mechanism leading to the photodegradation of 2,4-DCP is a process based on a mechanism consisting in the transfer of energy to oxygen molecule. According to that this process can be described by the following equation [22]:

$$r = -\frac{dC}{dt} = \frac{k_r \cdot C \cdot E_a \cdot \phi_{\Delta}}{k_d + k_t \cdot C}, \quad (4)$$

where k_d is solvent quenching rate constant, $M^{-1} s^{-1}$; k_t is total rate constant for physical and chemical decay of 1O_2 with 2,4-DCP, $M^{-1} s^{-1}$.

To investigate the effect of the initial concentration of substrate on the rate of photosensitized oxidation process, the test was carried out for six initial concentrations of 2,4-DCP in different pH of the solution (for undissociated and dissociated form) (Figure 4).

The application of (4) for the initial period of reaction allowed us to estimate the values of the constant rate of chemical reaction of 1O_2 . The values are shown in Table 2.

Determined constants of chemical and physical quenching and chemical reaction rate constants have the same order obtained in our earlier research for butylparaben [14].

3.3. *Solar Irradiation.* Interesting results were obtained in experiments in which the solution containing 2,4-DCP, a sensitizer, and oxygen was exposed to natural sunlight.

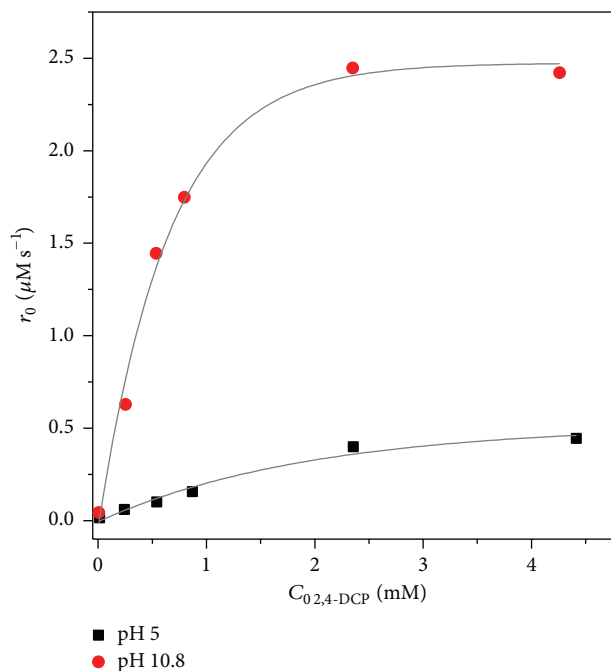


FIGURE 4: The dependence of the reaction rate photosensitized oxidation of the initial substrate concentration of 2,4-DCP using RB as a photosensitizer ($C_{0,\text{sens.}} = 2 \times 10^{-5}$ M, air bubbling, and xenon lamp irradiation).

The rate of the sensitized oxidation of 2,4-DCP was unexpectedly high. In sunny days complete disappearance of the substrate in alkaline solution in less than 10 minutes was achieved despite the fact that the mixture was bubbled only atmospheric air instead of pure oxygen (Figure 5).

The other observations are in agreement with the previous study with the experiments under the xenon lamp. The major role of singlet oxygen in the degradation of 2,4-DCP was also confirmed (the addition of sodium azide completely stopped the reaction). Similar results were observed in our previous studies with other substrates such as parabens [23], which confirms the applicability of singlet oxygen generated by excited photosensitizers for the photochemical oxidation of xenobiotics in water environments.

There were no marked differences in the substrate decay rate using TPPS₄, ALPcS₄, and RB (perhaps in such short reaction time these differences were difficult to notice) while the presence of ZnPcS₄ caused a significant inhibition of the degradation rate of 2,4-DCP (Figure 5).

The strong dependence of reaction progress on the pH of the environment in the range from 5 to 10.8 has also been proven. While in the alkaline solution (pH = 10.8) 2,4-DCP was almost completely removed after 10 minutes, at pH = 5 the photosensitized process resulted only in a 40% reduction of 2,4-DCP concentration after 2 hours of sunlight irradiation (Figure 6).

The long-term purpose of our work was also to assess the yield of the photosensitized oxidation of 2,4-DCP using natural sunlight in central Poland irradiation conditions.

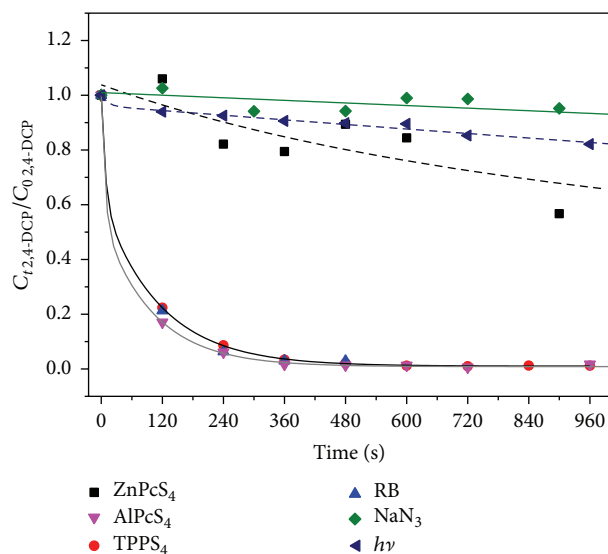


FIGURE 5: The dependence of 2,4-DCP relative concentrations decay on the type of used photosensitizer, in the absence of any sensitizer and in the presence of singlet oxygen scavenger, sodium azide ($C_{0,2,4\text{-DCP}} = 2.4 \times 10^{-4}$ M, $C_{0,\text{sens.}} = 2 \times 10^{-5}$ M, $C_{0,\text{NaN}_3} = 1 \times 10^{-1}$ M, pH = 10.8, air bubbling, and natural sunlight irradiation).

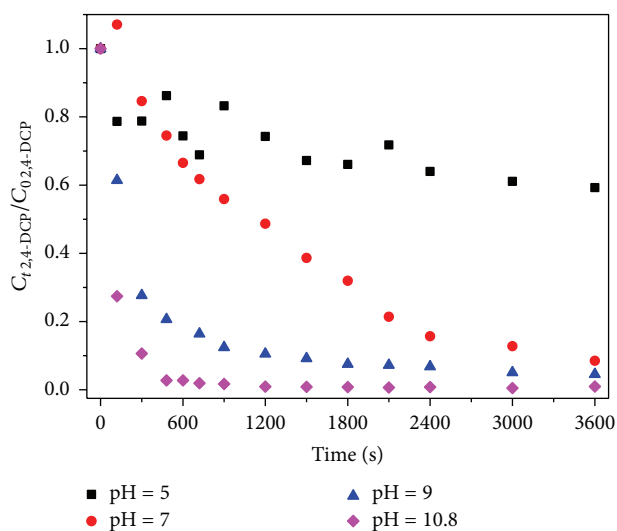


FIGURE 6: The dependence of 2,4-DCP relative concentrations decay on pH of solution ($C_{0,2,4\text{-DCP}} = 2.4 \times 10^{-4}$ M, $C_{0,\text{TPPS}_4} = 2 \times 10^{-5}$ M, air bubbling, and natural sunlight irradiation).

Conducting the experiments under various atmospheric conditions both in cloudless days and with semiclouded or completely clouded sky was therefore decided. These investigations were performed in a neutral pH in order to estimate theoretically the rate of this photoprocess which might occur in natural water due to sunlight in the presence of compounds which may act as sensitizers, for example, humic acids. Several experiments have been made under various weather conditions. The results are shown in Figure 7.

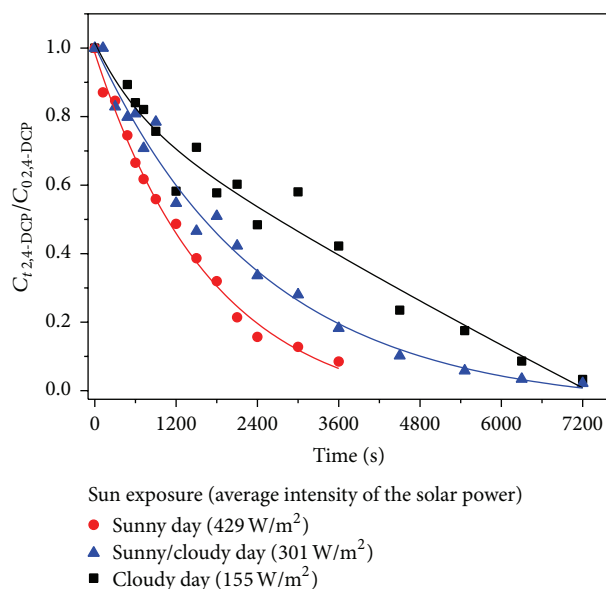


FIGURE 7: The dependence of 2,4-DCP relative concentrations decay under various sun insolation ($C_{0,2,4-DCP} = 2.4 \times 10^{-4} \text{ M}$, $C_{0,TPPS_4} = 2 \times 10^{-5} \text{ M}$, pH = 7, air bubbling, and natural sunlight irradiation).

It was observed that even in an “unfavorable” (not optimum) pH of the reaction medium the complete disappearance of 2,4-DCP was achieved after approx. 2 hours of exposure.

In view of obtained results we can state that photosensitized oxidation is effective method of xenobiotic degradation in water environments even in the middle latitude.

As can be seen in Figure 8 the photodegradation under sunlight is much effective than application of lamp as a light source, despite the smaller irradiance intensity. The photosensitized oxidation with TPPS₄ required the exposure to 725 kJ m^{-2} radiation to degrade 97% of initial 2,4-DCP concentration when xenon lamp was applied, whereas during natural sunlight irradiation only 526 kJ m^{-2} radiation was enough to degrade 99% of the same initial 2,4-DCP concentration. It should be noticed that from an economical point of view the use of natural sunlight can generate smaller technology costs.

3.4. Acute Toxicity Analysis. The toxicity assessment was conducted by a screening test and an EC₅₀ test for the photosensitized oxidation of 2,4-DCP in homogenous aqueous solutions under lamp irradiation. The results of the screening test during treatment time are shown in Figure 9. Based on the toxicity test performed for pure 2,4-DCP the EC₅₀ value was determined to be $2.92 \pm 0.96 \text{ mg L}^{-1}$. The available literature EC₅₀ values toward luminescent bacteria for 2,4-DCP range from 1.24 to 6.06 mg L^{-1} [24, 25]. As can be seen in Figure 9, the inhibition of luminescence of *V. fischeri* decreased during the photosensitized oxidation of 2,4-DCP. Although after 10 minutes of the treatment in the reaction mixture 2,4-DCP was very low, the inhibition of the *V. fischeri* luminescence is still high ($\approx 90\%$).

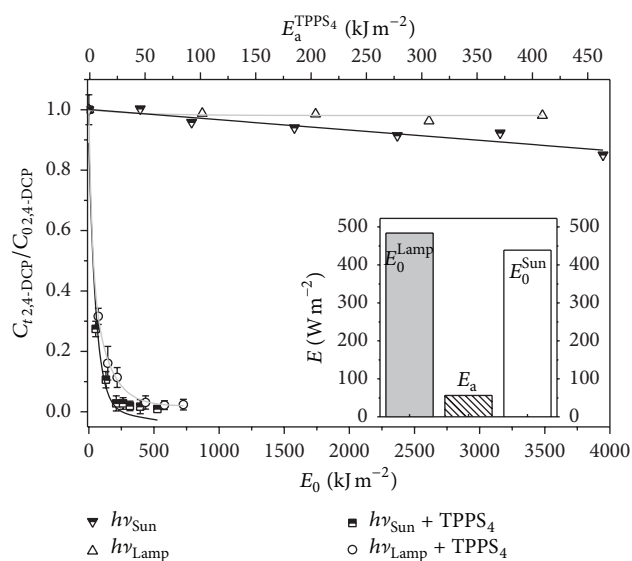


FIGURE 8: Variation in the concentration of 2,4-DCP during photodegradation experiments mediated by TPPS₄ and without TPPS₄ and induced by solar and lamp radiation. Insert: incident energy (E_0) of radiation for sunlight and lamp and energy absorbed (E_a) by TPPS₄.

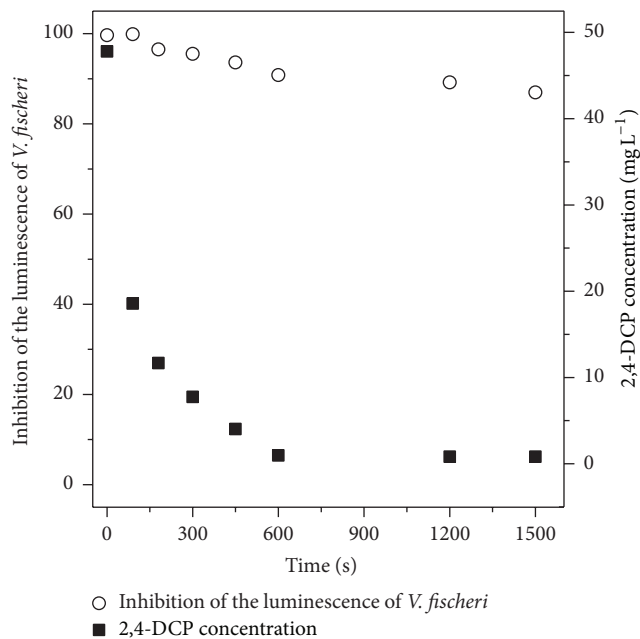


FIGURE 9: Toxicity analysis of 2,4-DCP photosensitized oxidation.

The determined EC₅₀ values are presented in Table 3. The reaction solution after photosensitized oxidation in homogenous solution indicated lower toxicity. It can be assumed that during photosensitized oxidation less toxic degradation products are formed compared with 2,4-DCP.

TABLE 3: Determined values of EC_{50} , the effective concentration of the sample that causes 50% decrease in the light output of the *Vibrio fischeri* organism under 15 minutes.

Time (min)	EC_{50} (%)	2,4-DCP conc. in reaction solution ($mg\ L^{-1}$)
0	2.69	47.80
5	4.05	7.74
10	6.06	0.96
25	9.64	0.81

However, it should be noticed that despite a large decrease in the 2,4-DCP concentration (about 60 times) EC_{50} value has increased slightly (only about 3.5 times). That unfortunately shows that although the transformation products are less toxic than 2,4-DCP, they are still characterized by very high toxicity.

4. Conclusion

Degradation of 2,4-DCP in the aqueous solution by photosensitized oxidation in a homogeneous aqueous solution under visible light irradiation is effective. The degradation occurs mainly due to the reaction with a singlet oxygen and to a small extent due to photolysis. The experimental evidence shows that this pathway of 2,4-DCP decomposition can appear to have a higher rate in the alkaline medium. The efficiency of the 2,4-DCP photodegradation strongly depends on the type of photosensitizer, initial concentration of 2,4-DCP, and oxygen content in reaction mixture. The toxicity assessment showed that photosensitized oxidation of 2,4-DCP resulted in a toxicity decrease.

In our opinion the photooxidation of phenolic compounds by singlet oxygen appears to be an interesting option from both the scientific and technological points of view due to its advantage of using ubiquitous substrates: oxygen from air and solar radiation. The interaction between them frequently occurs in nature, for example, in surface water, where the humic acids could act as the sensitizers.

The possibility of use of air and sunlight creates great opportunities of practical applications. The application of this process for large scale wastewater treatment would require the use of optimum sensitizer concentration, pH adjustment, and optimization of all other reaction conditions.

Competing Interests

The authors declare that there are no competing interests regarding the publication of this paper.

Acknowledgments

This research was supported by the National Science Centre (NCN) in Poland within research project 2012/07/B/ST8/03787. Marta Gmurek acknowledges the support from Foundation for Polish Science within the START scholarship.

References

- [1] D. Fatta-Kassinos, I. K. Kalavrouziotis, P. H. Koukoulakis, and M. I. Vasquez, "The risks associated with wastewater reuse and xenobiotics in the agroecological environment," *Science of the Total Environment*, vol. 409, no. 19, pp. 3555–3563, 2011.
- [2] M. Czaplicka, "Sources and transformations of chlorophenols in the natural environment," *Science of the Total Environment*, vol. 322, no. 1–3, pp. 21–39, 2004.
- [3] A. Białek and W. Moszczyński, "Technological aspects of the synthesis of 2,4-dichlorophenol," *Polish Journal of Chemical Technology*, vol. 11, no. 2, pp. 21–30, 2009.
- [4] F. Kargi and S. Eker, "Toxicity and batch biodegradation kinetics of 2,4 dichlorophenol by pure *Pseudomonas putida* culture," *Enzyme and Microbial Technology*, vol. 35, no. 5, pp. 424–428, 2004.
- [5] X. Jin, J. Zha, Y. Xu, Z. Wang, and S. S. Kumaran, "Derivation of aquatic predicted no-effect concentration (PNEC) for 2,4-dichlorophenol: comparing native species data with non-native species data," *Chemosphere*, vol. 84, no. 10, pp. 1506–1511, 2011.
- [6] U. G. Ahlborg, T. M. Thunberg, and H. C. Spencer, "Chlorinated phenols: occurrence, toxicity, metabolism, and environmental impact," *Critical Reviews in Toxicology*, vol. 7, no. 1, pp. 1–35, 1980.
- [7] US Environmental Protection Agency (USEPA), "Ambient water quality criteria for 2,4-dichlorophenol," Tech. Rep. EPA/440/5-80-042, USEPA, Washington, Wash, USA, 1980.
- [8] X. Y. Zhang, J. M. Zha, W. Li, L. H. Yang, and Z. J. Wang, "Effects of 2,4-dichlorophenol on the expression of vitellogenin and estrogen receptor genes and physiology impairments in Chinese rare minnow (*Gobiocypris rarus*)," *Environmental Toxicology*, vol. 23, no. 6, pp. 694–701, 2008.
- [9] S. Jiang, J. Zhu, Y. Ding, S. Bai, Y. Guan, and Q. Ye, "Effectiveness and mechanisms of fenton-like Si-FeOOH/H₂O₂ in 2,4-dichlorophenol wastewater treatment," *Ozone: Science & Engineering*, vol. 37, no. 6, pp. 495–502, 2015.
- [10] Y. Qiu, C.-H. Kuo, and M. E. Zappi, "Ozonation kinetics of six dichlorophenol isomers," *Ozone: Science & Engineering*, vol. 24, no. 2, pp. 123–131, 2002.
- [11] I. Dobrosz-Gómez, M. Á. Gómez-García, S. M. López Zamora et al., "Transition metal loaded TiO₂ for phenol photo-degradation," *Comptes Rendus Chimie*, vol. 18, no. 10, pp. 1170–1182, 2015.
- [12] A. M. Abeish, H. M. Ang, and H. Znad, "Solar photocatalytic degradation of chlorophenols mixture (4-CP and 2,4-DCP): mechanism and kinetic modelling," *Journal of Environmental Science and Health, Part A: Toxic/Hazardous Substances and Environmental Engineering*, vol. 50, no. 2, pp. 125–134, 2015.
- [13] J.-C. Sin, S.-M. Lam, A. R. Mohamed, and K.-T. Lee, "Degrading endocrine disrupting chemicals from wastewater by TiO₂ photocatalysis: a review," *International Journal of Photoenergy*, vol. 2012, Article ID 185159, 23 pages, 2012.
- [14] D. Gryglik, J. S. Miller, and S. Ledakowicz, "Singlet molecular oxygen application for 2-chlorophenol removal," *Journal of Hazardous Materials*, vol. 146, no. 3, pp. 502–507, 2007.
- [15] M. Gmurek, M. Bizukojć, J. Mosinger, and S. Ledakowicz, "Application of photoactive electrospun nanofiber materials with immobilized meso-tetraphenylporphyrin for parabens photodegradation," *Catalysis Today*, vol. 240, pp. 160–167, 2015.

- [16] F. Wilkinson, W. P. Helman, and A. B. Ross, "Quantum yields for the photosensitized formation of the lowest electronically excited singlet state of molecular oxygen in solution," *Journal of Physical and Chemical Reference Data*, vol. 22, no. 1, pp. 113–262, 1993.
- [17] J. M. Larkin, W. R. Donaldson, T. H. Foster, and R. S. Knox, "Reverse intersystem crossing from a triplet state of rose bengal populated by sequential 532- +1064-nm laser excitation," *Chemical Physics*, vol. 244, no. 2-3, pp. 319–330, 1999.
- [18] T. Nyokong, "Effects of substituents on the photochemical and photophysical properties of main group metal phthalocyanines," *Coordination Chemistry Reviews*, vol. 251, no. 13-14, pp. 1707–1722, 2007.
- [19] L. P. F. Aggarwal, M. S. Baptista, and I. E. Borissevitch, "Effects of NaCl upon TPPS4 triplet state characteristics and singlet oxygen formation," *Journal of Photochemistry and Photobiology A: Chemistry*, vol. 186, no. 2-3, pp. 187–193, 2007.
- [20] T. Gensch and S. E. Braslavsky, "Volume changes related to triplet formation of water-soluble porphyrins. A laser-induced optoacoustic spectroscopy (LIOAS) study," *The Journal of Physical Chemistry B*, vol. 101, no. 1, pp. 101–108, 1997.
- [21] D. Gryglik, M. Lach, and J. S. Miller, "The aqueous photosensitized degradation of butylparaben," *Photochemical & Photobiological Sciences*, vol. 8, no. 4, pp. 549–555, 2009.
- [22] J. S. Miller, "Rose bengal-sensitized photooxidation of 2-chlorophenol in water using solar simulated light," *Water Research*, vol. 39, no. 2-3, pp. 412–422, 2005.
- [23] D. Gryglik and M. Gmurek, "The photosensitized oxidation of mixture of parabens in aqueous solution," *Environmental Science and Pollution Research*, pp. 1–11, 2015.
- [24] K. L. E. Kaiser and V. S. Palabrica, "Photobacterium phosphoreum toxicity data index," *Water Pollution Research Journal of Canada*, vol. 26, no. 3, pp. 361–431, 1991.
- [25] R. Zona, S. Schmid, and S. Solar, "Detoxification of aqueous chlorophenol solutions by ionizing radiation," *Water Research*, vol. 33, no. 5, pp. 1314–1319, 1999.

Research Article

Design and Performance Evaluation of a Solar Assisted Heat Pump Dryer Integrated with Biomass Furnace for Red Chilli

M. Yahya

Fakultas Teknologi Industri, Institut Teknologi Padang, Padang, West Sumatra 25132, Indonesia

Correspondence should be addressed to M. Yahya; yahya@itp.ac.id

Received 20 January 2016; Accepted 7 March 2016

Academic Editor: Daniele Dondi

Copyright © 2016 M. Yahya. This is an open access article distributed under the Creative Commons Attribution License, which permits unrestricted use, distribution, and reproduction in any medium, provided the original work is properly cited.

The performance of a solar assisted heat pump dryer integrated with biomass furnace has been designed and evaluated for drying red chillies, and drying kinetics of red chillies were evaluated. The red chillies were dried from 22 kg with moisture content of 4.26 db to moisture content of 0.08 db which needed 11 hours, with the average drying chamber temperature, drying chamber relative humidity, and an air mass flow rate of 70.5°C, 10.1%, and 0.124 kg/s, respectively, while the open sun drying needed 62 hours. Compared to open sun drying, this dryer yielded 82% saving in drying time. The drying rate, the specific moisture extraction rate, and thermal efficiency of the dryer were estimated in average to be about 1.57 kg/h, 0.14 kg/kWh, and 9.03%, respectively. Three mathematical models, the Newton, Henderson-Pabis, and Page models, were fitted to the experimental data on red chillies dried by solar assisted heat pump dryer integrated with biomass furnace and open sun drying. The performance of these models was evaluated by comparing the coefficient of determination (R^2), mean bias error (MBE), and root mean-square error (RMSE). The Page model gave the best results for representing drying kinetics of red chillies.

1. Introduction

Indonesia is an agricultural country and produced 1,075,000 tons chilli in the year 2014, including red chilli [1]. Red chilli is an important ingredient in daily cuisine in Indonesia. It is consumed as fresh, dried, and powder forms. Red chilli is rich in protein, carbohydrates, calcium, phosphorus, vitamins A and C. It can be used to prevent heart diseases by dilating blood vessels and antioxidant [2, 3].

Commonly, fresh red chillies are dried using open sun drying. It is very simple and has low investment and operating costs. However, the open sun drying has disadvantages such as depending on the weather conditions, low quality products, and slow drying rate or long drying times. Solar dryer is one of the alternatives to solve this problem.

Some researchers have developed and tested several types of solar dryer to reduce drying time and to maintain the quality of red chillies obtained by open sun drying. Fudholi et al. [2, 4] reported that by using an indirect forced convection solar dryer for drying red chilli with a drying capacity of 40 kg the dryer was able to reduce the moisture content of 80% (wet basis) to 10% (wet basis) during 10 hours, while the open sun

drying needed 65 hours. Also, they reported that the dryer can save the drying time of approximately 49% compared to open sun drying. Kaewkiew et al. [5] found that by using a large-scale greenhouse type solar dryer for drying red chilli with a drying capacity of 500 kg this dryer only takes 3 days to reduce moisture content as much as 74% (wet basis) to 9% (wet basis), whereas open sun drying takes 5 days. Solar dryer was estimated which can save the drying time of about 40% compared to open sun drying. In addition, good quality of red chilli was obtained. Palled et al. [6] evaluated the performance of a solar tunnel dryer for drying red chilli. The result showed that the drying of 350 kg red chilli using this dryer needs 50 hours for reducing its moisture content from 76% (wet basis) to 9% (wet basis), while the open sun drying needs 105 hours. They found that the solar dryer saves 52.38% in the drying time compared to open sun drying. Banout et al. [7] reported the use of a double-pass solar dryer for drying red chilli. Drying 40 kg of red chilli using this dryer, the moisture content reduced from approximately 90% (wet basis) to 10% (wet basis) within 32 hours, while open sun drying took 93 hours. Also, they found that by using this dryer we can save the drying time about 65.59% compared to open sun drying.

Good quality products were obtained. Furthermore, Janjai et al. [3] found that by using a large-scale solar greenhouse using polycarbonate cover dryer for drying chilli with a drying capacity of 300 kg the dryer requires drying time for 3 days to reduce the moisture content from 75% (wet basis) to 15% (wet basis), while open sun drying takes 5 days. Also, solar dryer can save the drying time of approximately 40% over open sun drying. In addition, good quality dried product was obtained. Based on the results of the testing several researchers conclude that the solar dryers save over 39% of drying time of red chillies compared to open sun drying. However, the drying process can not be conducted or continued during the cloudy, rainy days and the night time because there is either no or low sunlight. Therefore, it is necessary to provide the solar dryers with an auxiliary heater, such as biomass furnace by using biomass as heat energy sources. Leon and Kumar [8] have evaluated the performance of a solar assisted biomass drying system with thermal storage for drying red chilli. They found that the drying of 22 kg red chilli using this dryer needs 32.5 hours of continuous drying for reducing its moisture content from 76.7% (wet basis) to 8.4% (wet basis), with the air drying temperature of 60°C and air flow rate of $90\text{ m}^3/\text{h}$, while the open sun drying needs 4 days. They found that the solar dryer saves 66% in the drying time compared to open sun drying. The solar assisted biomass drying system with thermal storage is also known as hot dryer because to decrease the drying time is done by increasing the air temperature. The high drying temperature causes damage to the flavour, colour, and nutrients of the dried chillies [9]. To overcome this problem, the drying time can be shortened by decreasing the air humidity. It can be done by removing or dehumidifying of the water vapor in the air by using dehumidifier such as heat pump. Dezfouli et al. [10] have evaluated the performance of a solar assisted heat pump dryer for drying red chilli. The result showed that the drying of 15 kg red chilli using this dryer needs 32 hours for reducing its moisture content from 4 on dry basis to 0.08 on dry basis, with an average temperature of 46°C , relative humidity of 27%, and air mass flow rate of 0.15 kg/h , while the open sun drying needs 64 hours. They found that the solar dryer saves 50% in the drying time compared to open sun drying. However, the drying air temperature is low at cloudy, rainy days and the night time. This will lead to long drying time because it limited the heat pump operating temperature refrigerant and compressor operating conditions.

Solar assisted heat pump dryer integrated with biomass furnace can be used for drying red chillies to resolve the disadvantages of the current drying techniques. It has many advantages such as low relative humidity, and the drying processes can be conducted at cloudy, rainy days and the night time.

Indonesia is a tropical country and is located in the equator line. The country receives a daily average solar radiation about 4 kWh/m^2 [11]. Also, Indonesia is one of the largest biomass producing countries in the world with its production of approximately 236 million tons of biomass per year, equivalent to about 756.083 mill GJ per year [12]. Therefore, the purpose of this paper is to design and to evaluate performance of a solar assisted heat pump dryer integrated with



FIGURE 1: Photograph of the solar assisted heat pump drying integrated with biomass furnace.

biomass furnace for drying red chilli in Indonesia and to investigate the drying characteristics of red chilli in a solar assisted heat pump dryer integrated with biomass furnace and open sun drying and to fit the experimental data to select the best mathematical models.

2. Material and Methods

2.1. Experimental Set-Up. A solar assisted heat pump dryer integrated with biomass furnace was designed and installed at the Institute of Technology, Padang, West Sumatra, Indonesia. The drying system consists of solar collector array, heat pump, biomass furnace, drying chamber, and blower shown in Figures 1 and 2. The solar collector is equipped with transparent cover glass material, absorber plate finned used aluminum and black painted opaque, angle iron frame, inside and outside the collector coated with aluminum 1 mm thick, and insulation using glass fiber materials. Two solar collectors are connected in series with an area of 1.8 m^2 each, shown in Figure 3. The heat pump consists of several main parts: evaporator, condenser, compressor, and expansion valve. The working fluid of the heat pump is R-22. Compressor use of electrical capacity is 0.746 kW. The dimension of evaporator and condenser of the heat pump is shown in Figure 4. The biomass furnace consists of several main parts such as the combustion chamber, heat exchanger, chimney, and blower. The wall of the combustion chamber uses brick, cement, and steel plate materials and heat exchanger pipes using mild steel with diameter of 2 inch and number of pipes is 16 units, dimension of biomass furnace shown in Figure 5. The drying chamber uses the cabinet type and contains the drying trays with adjustable racks to place the red chilli. Its walls consist of triple layers, an outside layer which uses aluminum sheet, a middle one insulated with glass fiber materials, and inner layer which uses of aluminum sheet, dimension of drying chamber shown in Figure 6. The drying air is circulated by using blower with electrical capacity of 0.75 kW.

2.2. Experimental Procedure. The experiments were carried out at Padang Institute of Technology, West Sumatra, Indonesia. Fresh red chilli was purchased at the local market in

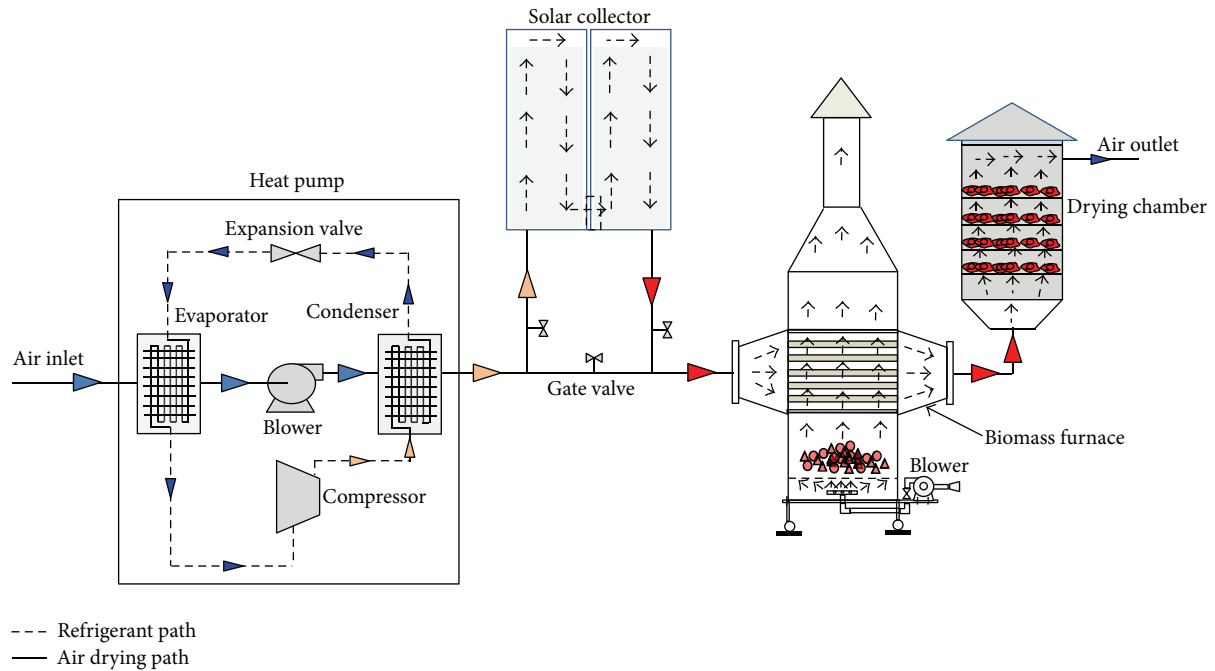


FIGURE 2: Schematic diagram of the solar assisted heat pump drying integrated with biomass furnace.

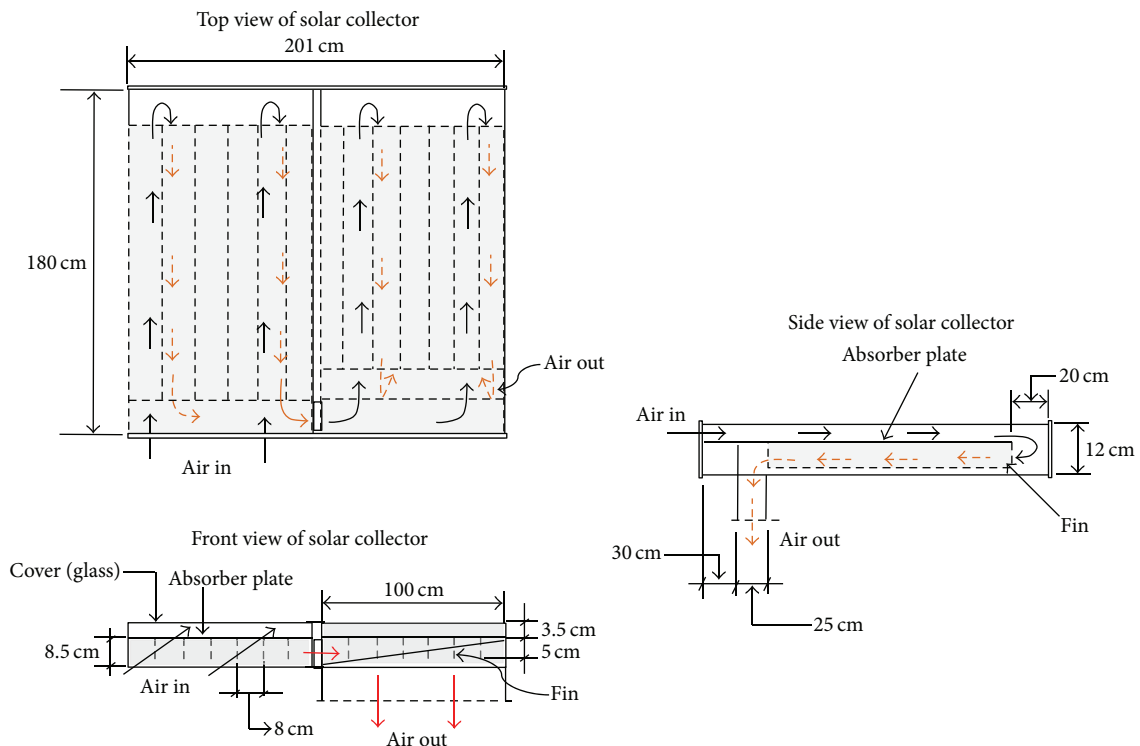


FIGURE 3: Dimensions of a double-pass solar collector with fin.

Padang. As much as 22 kg was placed into the drying chamber for the drying process shown in Figure 7.

Incoming and outgoing air temperature of solar collector, heat pump, biomass furnace, and drying chamber during the operation of the drying system were measured by using T

type copper-constantan thermocouples with an accuracy of $\pm 0.1^\circ\text{C}$ and operating temperature range (-200°C to 400°C). The solar radiation was measured by an LI-200 pyranometer in $\pm 0.1 \text{ Wm}^{-2}$ accuracy and with maximum solar radiation of 2000 Wm^{-2} , operating temperature range (-40°C to 400°C)

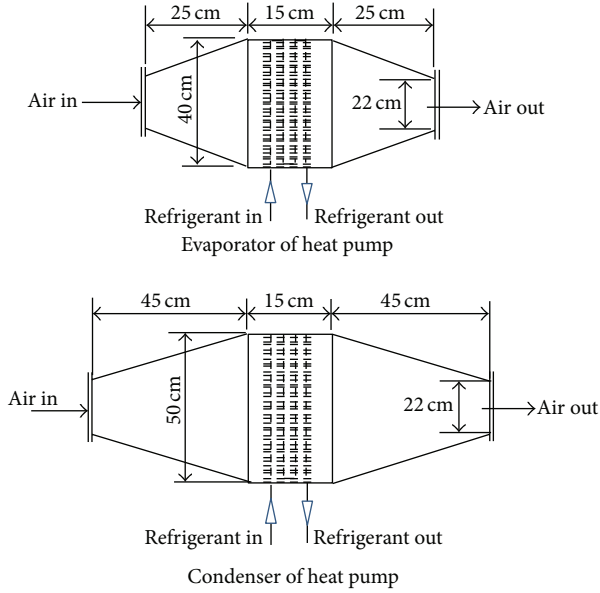


FIGURE 4: Dimensions of evaporator and condenser of heat pump.

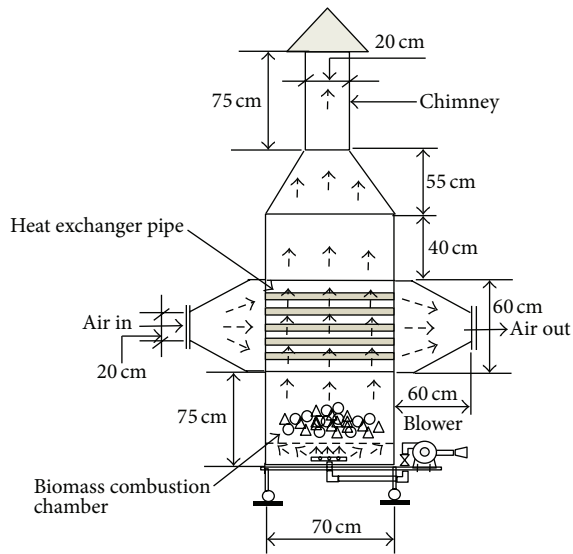


FIGURE 5: Dimensions of biomass furnace.

and operating relative humidity range (0% to 100%). The air velocity was measured with 0–30 ms^{-1} range, an HT-383 anemometer, an accuracy of $\pm 0.2 \text{ms}^{-1}$, and operation temperature range (-10°C to 45°C). The air temperature and the solar radiation were recorded by an AH4000 data logger with reading accuracy of $\pm 0.1^\circ\text{C}$. The weight change of the red chilli was measured by 0–15 kg range, an TKB-0.15 weighing scale, an accuracy $\pm 0.05 \text{kg}$. Red chillies were weighed every 60 minutes and temperature was measured every 30 minutes.

2.3. Experimental Data Analysis

2.3.1. Performance of Drying System. The performance of solar assisted heat pump dryer integrated with biomass

furnace is characterized by drying rate, specific moisture extraction rate, and dryer thermal efficiency. It is highly depending on the performance of each of the drying system components such as solar collector, heat pump, and biomass furnace.

The thermal efficiency of a solar collector is the ratio of useful heat gain by solar collector to the energy incident in the plane of the collector. It is calculated as [13]

$$\eta_{\text{coll}} = \frac{\dot{m}_{\text{air}} C_{P\text{air}} (T_{o,\text{coll}} - T_{i,\text{coll}})}{I_T A_C} \times 100\%, \quad (1)$$

where \dot{m}_{air} is air mass flow rate, $C_{P\text{air}}$ is specific heat of air, and $T_{i,\text{coll}}$ and $T_{o,\text{coll}}$ are inlet and outlet air temperatures of solar collector, respectively. A_C is an area of collector and I_T is solar radiation incident in the collector.

The coefficient of performance of a heat pump is the ratio of useful heat or heat energy released by the refrigerant in the condenser to the electrical energy consumed by compressor. It is calculated as [14]

$$\text{COP}_{\text{hp}} = \frac{\dot{m}_{\text{air}} C_{P\text{air}} (T_{o,\text{cond}} - T_{i,\text{cond}})}{E_{\text{comp}}}, \quad (2)$$

where $T_{i,\text{cond}}$ and $T_{o,\text{cond}}$ are inlet and outlet air temperatures of condenser, respectively, and E_{comp} is the electrical energy consumed by the compressor.

The electrical energy consumed by compressor was calculated using the following equation [15]:

$$E_{\text{comp}} = VI \cos \varphi, \quad (3)$$

where V is the line voltage, I is the line current, and $\cos \varphi$ is the power factor.

The thermal efficiency of a biomass furnace is the ratio of useful heat by biomass furnace to the heat energy generated by the combustion of the biomass fuel. It is calculated as [16]

$$\eta_{\text{bf}} = \frac{\dot{m}_{\text{air}} C_{P\text{air}} (T_{o,\text{bf}} - T_{i,\text{bf}})}{\dot{m}_{\text{bmf}} CV_{\text{bmf}}} \times 100\%, \quad (4)$$

where $T_{i,\text{bf}}$ and $T_{o,\text{bf}}$ are the inlet and outlet air temperatures of biomass furnace, respectively, \dot{m}_{bmf} is biomass fuel consumption rate, and CV_{bmf} is caloric value of biomass fuel. The biomass fuel uses coconut shell charcoal with a caloric value of about 7600 kcal/kg [17].

The moisture content of the red chillies can be estimated by two methods such as wet and dry basis using the following equation [10].

The moisture content wet basis was calculated as

$$\text{MC}_{\text{wb}} = \frac{m_w}{m_w + m_d}. \quad (5)$$

The moisture content dry basis was calculated as

$$\text{MC}_{\text{db}} = \frac{m_{\text{wetrc}} - m_d}{\dot{m}_d}, \quad (6)$$

where m_w is the mass of water of the red chillies, m_d is the mass of bone dry of the red chillies, and m_{wetrc} is mass of wet red chillies.

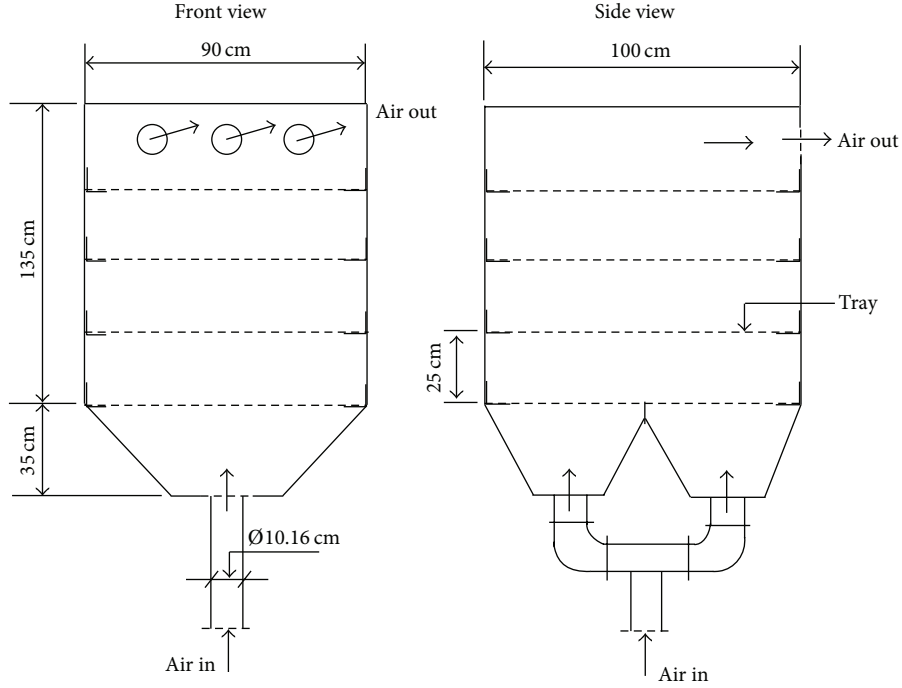


FIGURE 6: Dimensions of drying chamber.



FIGURE 7: Photograph of red chilli in drying chamber.

The drying rate is the mass of water evaporated from the wet red chillies per unit time. It is calculated using the following equation [2]:

$$DR = \dot{m}_{\text{water}} = \frac{m_{\text{water}}}{t}, \quad (7)$$

where m_{water} is the mass of water evaporated and t is drying time.

The mass of the water evaporated (m_{water}) from the wet red chillies can be calculated as [18]

$$m_{\text{water}} = \frac{m_{\text{wetrc}} (M_i - M_f)}{(100 - M_f)}, \quad (8)$$

where m_{wetrc} is initial mass of wet red chillies, M_i is initial moisture content on wet basis, and M_f is final moisture content on the wet basis.

The specific moisture extraction rate (SMER) is the ratio of the moisture evaporated from wet red chillies to the energy input to drying system. It is calculated as [19]

$$SMER = \frac{\dot{m}_{\text{water}}}{E_s + E_{\text{bmf}} + E_{\text{comp}} + E_{\text{bl}}}, \quad (9)$$

where E_s is energy incident in the plane of the solar collector and E_{bmf} is heat energy generated by the combustion of biomass fuel. E_{comp} and E_{bl} are electrical energy consumed by compressor and blower, respectively.

The thermal efficiency of dryer is the ratio of the energy used for moisture evaporation to the energy input to drying system. It is calculated as [20]

$$\eta_{\text{dryer}} = \frac{\dot{m}_{\text{water}} H_{\text{fg}}}{E_s + E_{\text{bmf}} + E_{\text{comp}} + E_{\text{bl}}}, \quad (10)$$

where H_{fg} is the latent heat of vaporization of water.

The heat energy used by the drying system for drying red chillies is a contribution from the drying system components such as solar collector, condenser, and biomass furnace. The percentage of heat energy contribution by the solar collector, condenser, and biomass furnace is calculated using (11), (12), and (13), respectively [8].

The percentage of heat energy contribution by solar collector can be calculated as follows:

$$HEC_{\text{coll}} = \frac{Q_{\text{Ucoll}}}{Q_{\text{Ucoll}} + Q_{\text{Ucond}} + Q_{\text{Ubf}}}. \quad (11)$$

TABLE 1: Mathematical models used for drying curves.

Model name	Model	References
Newton	$MR = \exp(-kt)$	[23, 24]
Henderson and Pabis	$MR = a \exp(-kt)$	[25, 26]
Page	$MR = \exp(-kt^n)$	[27, 28]

The percentage of heat energy contribution by condenser can be calculated as follows:

$$HEC_{\text{cond}} = \frac{Q_{U\text{cond}}}{Q_{U\text{cond}} + Q_{U\text{coll}} + Q_{U\text{bf}}}. \quad (12)$$

The percentage of heat energy contribution by biomass furnace can be calculated as follows:

$$HEC_{\text{bf}} = \frac{Q_{U\text{bf}}}{Q_{U\text{bf}} + Q_{U\text{coll}} + Q_{U\text{cond}}}, \quad (13)$$

where $Q_{U\text{coll}}$ is the useful heat gain by solar collector, $Q_{U\text{cond}}$ is the useful heat or heat energy released by refrigerant in the condenser, and $Q_{U\text{bf}}$ is the useful heat by biomass furnace.

2.3.2. Mathematical Modelling of Drying Curves. The experimental drying data obtained were fitted to the three best drying models given in Table 1. The dimensionless moisture content was calculated as follows [21]:

$$MR = \frac{(M_t - M_e)}{(M_o - M_e)}, \quad (14)$$

where MR is the dimensionless moisture content and M_e , M_o , and M_t are the equilibrium moisture content, the initial moisture content, and the moisture content at any time on dry basis, respectively.

The regression analysis was performed using Statistica computer program. The correlation coefficient (R^2) was primary criterion for selecting the best equation to describe the drying curve equation. The values of the coefficient of determination (R^2), mean bias error (MBE), and root mean-square error (RMSE) were used to analyze the relative goodness of the fit. These parameters can be calculated as follows [22]:

$$MBE = \frac{1}{N} \sum_{i=1}^N (MR_{\text{pre},i} - MR_{\text{exp},i})^2, \quad (15)$$

$$RMSE = \left[\frac{1}{N} \sum_{i=1}^N (MR_{\text{pre},i} - MR_{\text{exp},i})^2 \right]^{1/2},$$

where $MR_{\text{exp},i}$ is the i th experimental dimensionless moisture content, $MR_{\text{pre},i}$ is the i th predicted dimensionless moisture content, N is the number of observations, and n is the number constants.

2.4. Experimental Uncertainty. In the drying experiments of the red chillies the data was obtained by appropriate instrument; however, errors and uncertainties can arise because

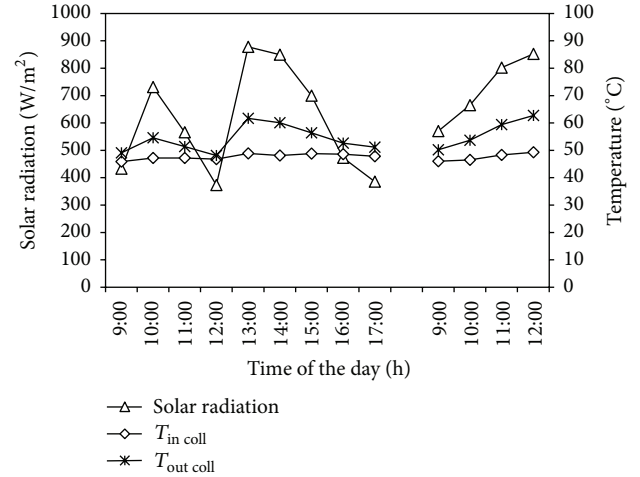


FIGURE 8: The variation of solar radiation and temperature with time of the day.

of the situations such as instrument selection, condition, environment, observation, reading, and test planning. Uncertainty was calculated using the following equation [29, 30]:

$$W_R = \left[\left(\frac{\partial R}{\partial x_1} w_1 \right)^2 + \left(\frac{\partial R}{\partial x_2} w_2 \right)^2 + \dots + \left(\frac{\partial R}{\partial x_n} w_n \right)^2 \right]^{1/2}. \quad (16)$$

3. Results and Discussion

The variations of solar radiation and inlet and outlet air temperatures of the solar collector with time of the day are shown in Figure 8. As seen from the figure the weather is quite bright with an average solar radiation of 637 Wm^{-2} which was observed. The inlet air temperature of the solar collector is varied between 45.9°C and 49.3°C and in average is 47.6°C . Meanwhile, the outlet air temperature of the solar collector is varied between 49.1°C and 62.7°C and in average is 54.7°C . Also it is observed from the figure that the outlet air temperature of the solar collector is very dependent on the solar radiation; when solar radiation is high, the outlet air temperature of the solar collector is also high, and vice versa. The evaluation of the uncertainty of dryer performance is presented in Table 2.

The variations of solar radiation and efficiency of solar collector with time of the day are shown in Figure 9. The maximum, minimum, and average of the solar collector efficiency were estimated to be about 12.0%, 54.6%, and 35.1%, respectively, with an air mass flow rate being about 0.1254 kg s^{-1} . As observed from the figure the solar collector is very sensitive to solar radiation; if the solar radiation fluctuates, the solar collector efficiency also fluctuates.

The variations of air temperatures and relative humidities inlet and outlet of the heat pump are shown in Figure 10. The inlet and outlet air temperature of the heat pump are varied between 31.2°C and 37.2°C and 47.5°C and 50.3°C and in average are about 34.1°C and 49.1°C , respectively. Meanwhile,

TABLE 2: Uncertainties of the parameters during drying experiment of red chilli.

Parameters	Unit	Uncertainty comment
<i>Measured</i>		
Ambient air temperature	°C	±0.17
Inlet air temperature of heat pump	°C	±0.17
Outlet air temperature of heat pump	°C	±0.17
Inlet air temperature of condenser	°C	±0.17
Outlet air temperature of condenser	°C	±0.17
Inlet air temperature of solar collector	°C	±0.17
Outlet air temperature of solar collector	°C	±0.17
Inlet air temperature of biomass furnace	°C	±0.17
Outlet air temperature of biomass furnace	°C	±0.17
Inlet air temperature of drying chamber	°C	±0.17
Outlet air temperature of drying chamber	°C	±0.17
Ambient air relative humidity	%	±0.22
Inlet air relative humidity of heat pump	%	±0.22
Outlet air relative humidity of heat pump	%	±0.22
Inlet air relative humidity of drying chamber	%	±0.22
Outlet air relative humidity of drying chamber	%	±0.22
Solar radiation	W/m ²	±0.14
Air velocity	m/s	±0.24
Mass loss of samples	g	±0.014
Mass loss of products	kg	±0.11
Reading values of table (ρ , C_p , CV, and H_{fg})	—	±0.1–0.2
Time measurement	min	±0.1
<i>Calculated</i>		
Air mass flow rate	kg/s	±0.26
Power consumption of compressor	kW	±0.056
Power consumption of blower	kW	±0.037
Thermal efficiency of solar collector	%	±0.39
Coefficient of performance of heat pump	—	±0.37
Thermal efficiency of biomass furnace	%	±0.458
Moisture content	g water/g wet material	±0.024
Drying rate	kg/h	±0.18
Specific moisture extraction rate	kg/kWh	±0.336
Thermal efficiency of dryer	%	±0.350
Contribution heat energy by condenser	%	±0.736
Contribution heat energy by solar collector	%	±0.736
Contribution heat energy by biomass furnace	%	±0.736

inlet and outlet air relative humidity of heat pump are varied between 50.3% and 62.7% and 26.2% and 32.7% and in average are about 57.4% and 28.8%, respectively. The heat pump can increase the air temperature and can decrease the relative humidity with an average of about 15.0°C and 28.8%, respectively.

The variations of inlet and outlet air temperatures and COP of the heat pump are shown in Figure 11. The average inlet and outlet temperatures of the condenser of about 26.9°C and 49.1°C were recorded. Meanwhile, the minimum, maximum, and average of the COP of the heat pump were estimated to be about 3.76, 3.95, and 3.84, respectively, with an air mass flow rate being about 0.124 kgs⁻¹.

The variations of inlet and outlet air temperatures and efficiency of the biomass furnace are shown in Figure 12. The inlet and outlet air temperatures of the biomass furnace varied between 47.6°C and 61.2°C and 70.5°C and 75.3°C with an average of about 53.2°C and 72.8°C, respectively. The minimum, maximum, and average of the efficiency of biomass furnace were estimated to be about 15%, 43.5%, and 30.7%, respectively, with an air mass flow rate of about 0.124 kgs⁻¹. As seen from the figure the biomass furnace efficiency achieved is quite low, because of a lot of heat loss to the environment.

The variations of air temperature and ambient, inlet, and outlet relative humidity of the drying chamber with drying

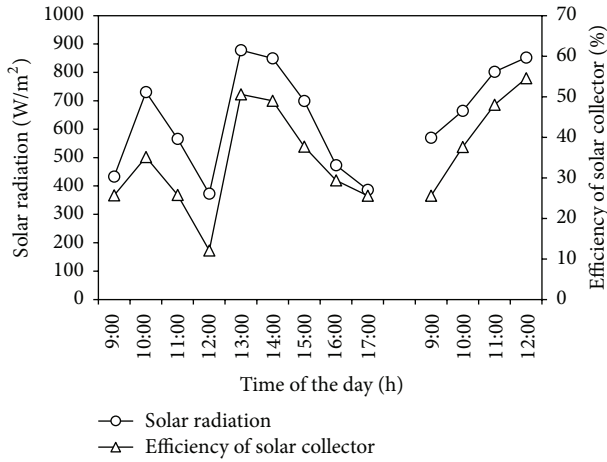


FIGURE 9: The variations of solar radiation and efficiency of solar collector with time of the day.

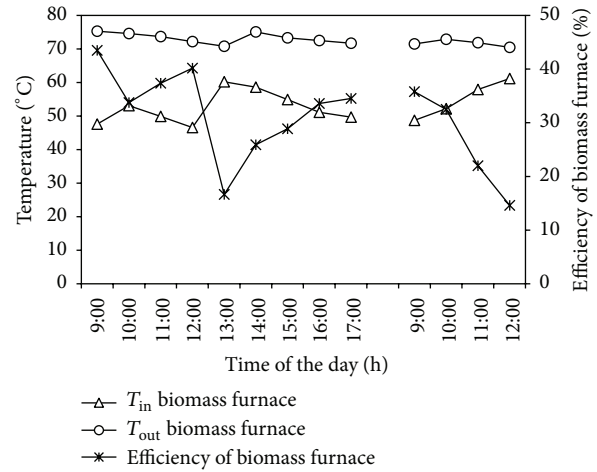


FIGURE 12: The variation of temperature and efficiency of the biomass furnace with time of the day.

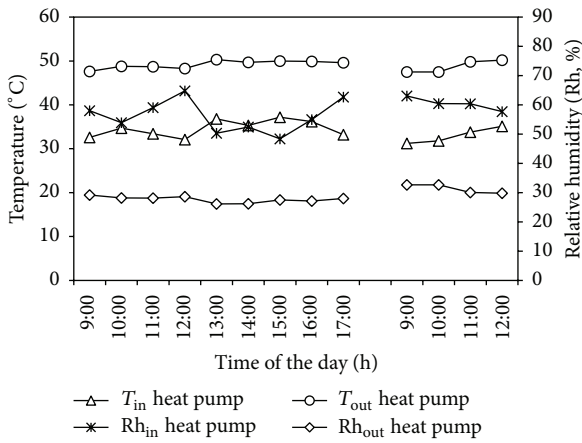


FIGURE 10: The variation of temperature and relative humidity with time of the day.

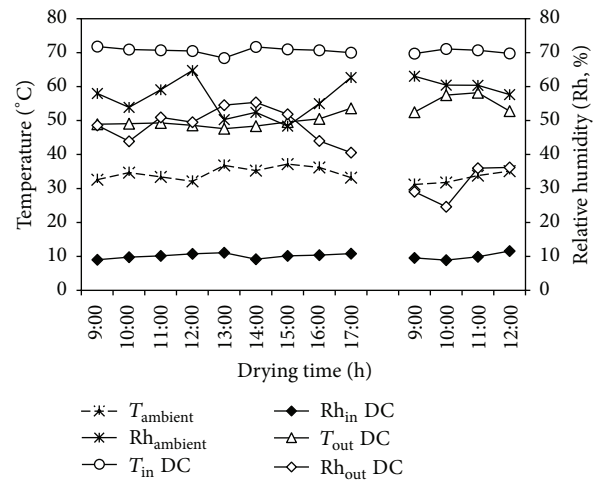


FIGURE 13: The variation of temperature and relative humidity with drying time.

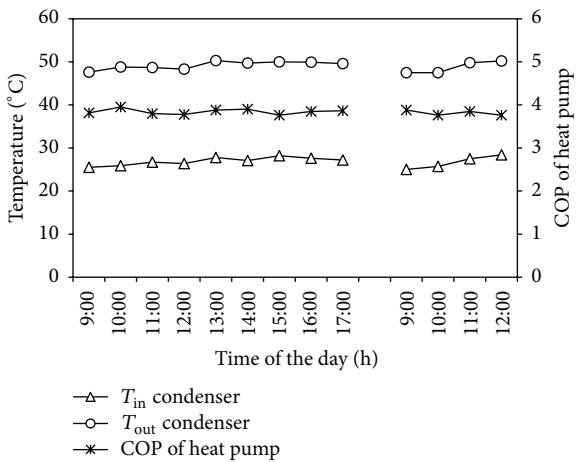


FIGURE 11: The variation of temperature and COP of the heat pump with time of the day.

time are shown in Figure 13. The drying chamber inlet temperature, drying chamber outlet temperature, drying chamber inlet relative humidity, and drying chamber outlet relative humidity are varied between 68.4°C and 71.8°C, 47.6°C and 58.2°C, 9.0% and 11.6%, and 24.6% and 55.4%, respectively, with corresponding average values of 70.5°C, 51.3°C, 10.1%, and 43.5%. The temperature ambient and relative humidity ambient are varied between 31.2°C and 33.8°C and 48.4% and 63.1%, respectively, with corresponding average values of 34.1°C and 57.4%. The results indicated that the air drying temperatures in solar assisted heat pump integrated with biomass furnace were higher than the ambient temperature; meanwhile the relative humidity in this dryer was lower than the ambient relative humidity. The difference values of air temperature and relative humidity were estimated to be about 36.4°C and 47.3%, respectively, in the 11-hour drying period. It can be stated that the drying rate in the dryer is higher than in open sun drying. As seen from figure the drying chamber outlet air temperature increased and the drying chamber

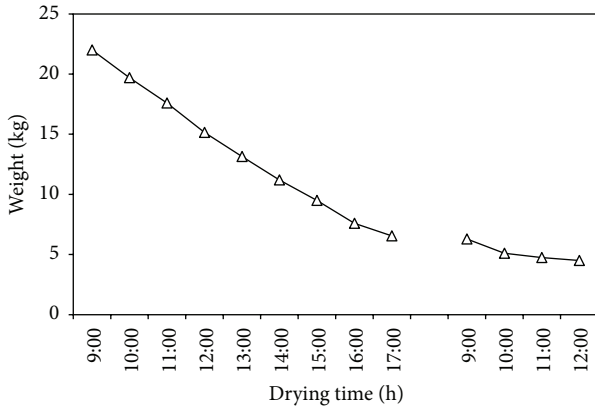


FIGURE 14: The variation of weight change of red chillies with drying time.

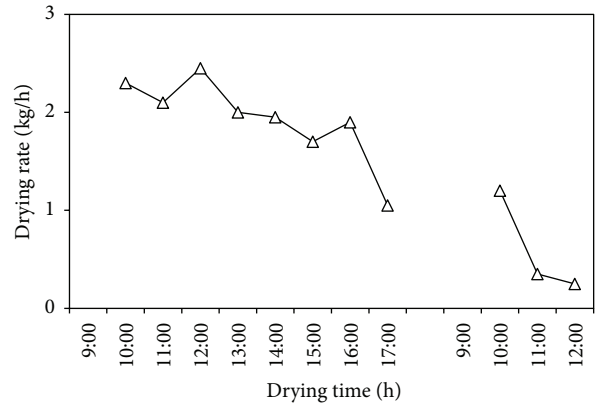


FIGURE 16: The variation of drying rate with drying time.

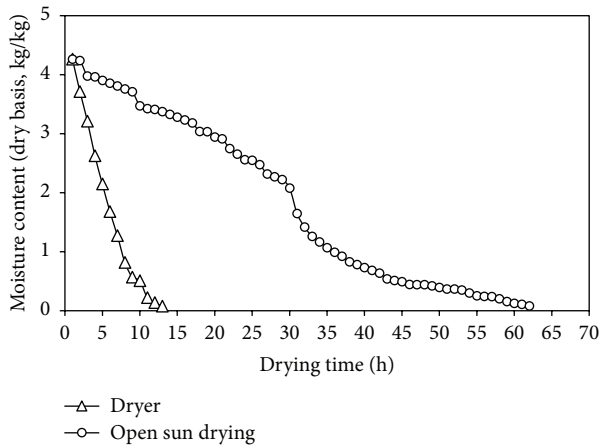


FIGURE 15: The variation of moisture content of dried red chilli in the solar assisted heat pump integrated with biomass furnace and open sun drying with drying time.

outlet relative humidity decreased with increasing in drying time. Due to these, the heat and mass transfer coefficients decreased in the drying time. Also it is observed from the figure that the air temperature of the outlet of the drying chamber is high, whereas the air relative humidity of the outlet of the drying chamber is low, and it is potential for recirculating to dry the red chilli.

The variation of weight change of red chillies with drying time is shown in Figure 14. As observed from the figure the weight of red chillies was reduced continuously with increasing in drying time. The weight of red chillies was reduced from 22 kg to 4.5 kg in 11 hours, with an air mass flow rate of 0.124 kgs^{-1} and an averages drying air temperature and relative humidity of about 70.5°C and 10.1% , respectively.

The variations of moisture content of dried red chilli in the solar assisted heat pump integrated with biomass furnace and open sun drying with drying time are shown in Figure 15. The moisture content was dried of red chilli to final moisture content of about 0.08 on dry basis from 4.26 on dry basis. The time to reach the final moisture content for solar assisted heat pump integrated with biomass furnace

was found to be about 11 hours, with an air mass flow rate of 0.124 kgs^{-1} and an average drying air temperature and relative humidity of about 70.5°C and 10.1% , respectively. Meanwhile, the drying time of open sun drying was found to be about 62 hours, with an average ambient air temperature and ambient relative humidity of about 34.1°C and 57.4% , respectively. The solar assisted heat pump integrated with biomass furnace had a shorter drying time compared to open sun drying. In other words, the dryer reduced the drying time or saved the drying time of about 82% compared to open sun drying. The decrease in drying time could be due to the values of higher temperature and lower relative humidity obtained in the dryer. At higher temperature and lower relative humidity, the difference in the partial vapor pressure between red chilli and the drying air is higher than at lower temperature and higher relative humidity. Hence, the moisture content transfer rate was more with higher air drying temperature.

The variation of drying rate with drying time is shown in Figure 16. The minimum, maximum, and average of the drying rate were estimated to be about 0.25 kg/h , 2.45 kg/h , and 1.57 kg/h , respectively. As observed from the figure the drying rate decreased with increase in drying time. Due to this, the evaporation rate of moisture decreased in the drying time.

The variations of SMER and dryer thermal efficiency with drying time are shown in Figures 17 and 18. Figure 17 shows the variation of SMER with drying time. The minimum, maximum, and average of the SMER were estimated to be about 0.02, 0.24 kg/kWh , and 0.14 kg/kWh , respectively. Figure 18 shows the variation of dryer thermal efficiency with drying time. The thermal efficiency varies from 1.34% to 15.36% with an average of 9.03%, respectively. As observed from Figures 18 and 19 the SMER and the dryer thermal efficiency also decreased with increase in drying time. Due to these, the evaporation rate of moisture decreased in the drying time.

The variations of the contribution of heat energy with drying time are shown in Figure 19. The contribution of heat energy by the collector varies from about 2.7% to 30.0% and with average of 14.74%, respectively. The contribution of heat energy by the condenser varies from about 43.7% to 50.4% and with average of 47.39%, respectively. Meanwhile,

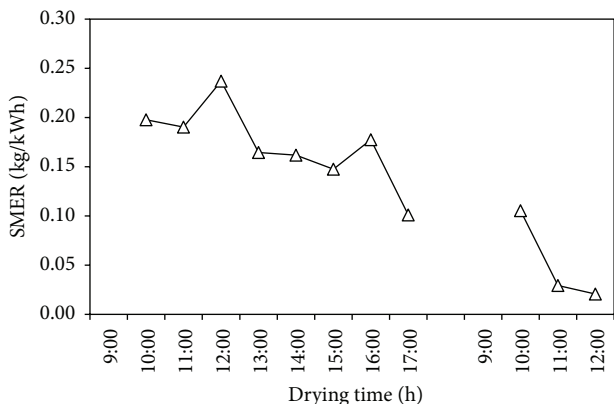


FIGURE 17: The variation of SMER with drying time.

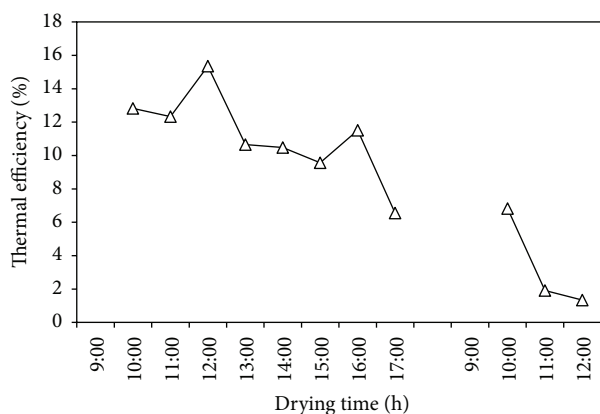


FIGURE 18: The variation of dryer thermal efficiency with drying time.

the contribution of heat energy by the biomass furnace varies from about 19.6% to 50.3% and with average of 37.87%, respectively. Also it is observed from the figure that the contribution of heat energy by the condenser of heat pump is greater than the solar collector and biomass furnace, because the condenser can improve the drying air temperature reached with average value of 49.1°C.

The experimental results of drying of red chilli using a solar assisted heat pump integrated with biomass furnace were compared with open sun drying and several types of solar dryers in references are shown in Table 3. In this dryer, the red chillies were dried from moisture content of 4.26 on dry basis to moisture content of 0.08 on dry basis which needed drying time 11 hours, with the average drying chamber temperature, drying chamber relative humidity, and an air mass flow rate of 70.5°C, 10.1%, and 0.124 kg/s, respectively. Meanwhile, the drying time in several types of solar dryers in the references was varied from 32 hours to 50 hours. The results revealed that this dryer is better than several types of solar dryers in the references. This is because the drying time is lower than the several types of solar dryers in the references.

The variations of dimensionless moisture content data of dried red chilli in a solar assisted heat pump integrated

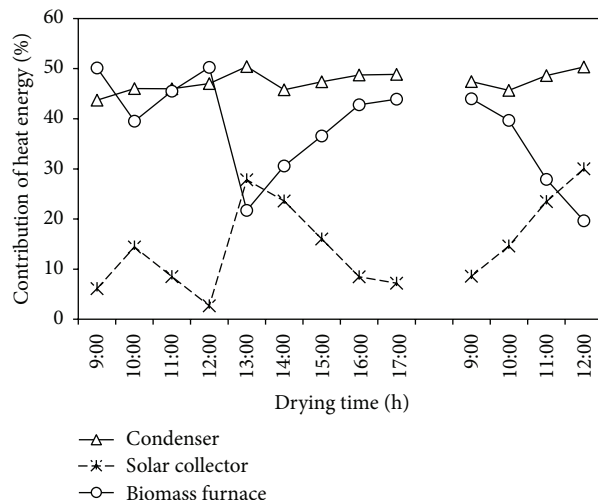


FIGURE 19: The variation of the contribution of heat energy with drying time.

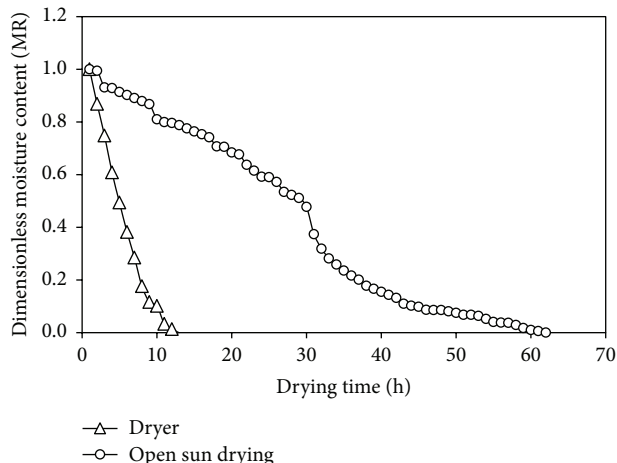


FIGURE 20: The variation of dimensionless moisture content data of dried red chilli in a solar assisted heat pump integrated with biomass furnace and open sun drying with drying time.

with biomass furnace and open sun drying with drying time are shown in Figure 20. The dimensionless moisture content of red chilli reduced exponentially as the drying time increased. Continuous decrease in dimensionless moisture content indicates that diffusion has governed the internal mass transfer. As seen from the figure the reduction of moisture content of red chilli dried using a solar assisted heat pump integrated with biomass furnace is faster than the open sun drying; this is because the air drying temperature is higher, and air drying relative humidity is lower than the open sun drying. At high air drying temperature and low relative humidity, the difference in partial vapor pressure between red chilli and the air drying is high; thereby the acceleration of moisture migration is also high.

The dimensionless moisture content data of dried red chilli in a solar assisted heat pump integrated with biomass furnace and open sun drying were fitted in three drying

TABLE 3: Performances of solar assisted heat pump integrated with biomass furnace compared with open sun drying and several types of solar dryers in references.

Number	Type of dryer	Drying capacity (kg)	Moisture content (% wb)	M_i	M_f	Drying time	Saving in time (%)	Thermal efficiency (%)	SMER (kg/kWh)	Refs.
1	Open sun drying	—	80	10	10	65 h	—	—	—	[4]
	Solar drying	40	80	10	10	33 h	49	28	0.19	
2	Open sun drying	—	74	9	9	5 days	—	—	—	[5]
	Solar greenhouse dryer	500	74	9	9	3 days	40	—	—	
3	Open sun drying	—	76	9	9	105 h	—	—	—	[6]
	Solar tunnel dryer	350	76	9	9	50 h	52.38	—	—	
4	Open sun drying	—	90	10	10	93 h	—	—	—	[7]
	Double-pass solar dryer	40	90	10	10	32 h	65.59	—	—	
5	Open sun drying	—	75	15	15	5 days	—	—	—	[3]
	Solar greenhouse dryer	300	75	15	15	3 days	40	—	—	
6	Open sun drying	—	76.7	8.4	8.4	4 days	—	—	—	[8]
	Solar assisted biomass drying	22	76.7	8.4	8.4	32.5 h	66	—	—	
7	Open sun drying	—	4 db	0.08 db	0.08 db	64 h	—	—	—	[9]
	Solar assisted heat pump dryer	15	4 db	0.05 db	0.05 db	32 h	50	—	—	
8	Open sun drying	7.5	4.26 db	0.08 db	0.08 db	62 h	—	—	—	Present study
	Solar assisted heat pump dryer integrated with biomass furnace	22	4.26 db	0.08 db	0.08 db	11 h	82	9.03	0.14	

TABLE 4: Statistical results mathematical modelling of drying curves.

Model	Method of drying	Model coefficients and constants	R^2	MBE	RMSE
Newton	Open sun drying	$k = 0.0560$	0.7235	0.0376	0.1939
	Dryer	$k = 0.2900$	0.8687	0.0137	0.1172
Henderson and Pabis	Open sun drying	$k = 0.0756; a = 2.2246$	0.7946	0.0662	0.2574
	Dryer	$k = 0.3576; a = 1.6335$	0.9093	0.0037	0.0609
Page	Open sun drying	$k = 1.4873; n = 0.0072$	0.9410	0.0051	0.0713
	Dryer	$k = 1.4080; n = 0.1140$	0.9822	0.0008	0.0278

models such as the Newton model, Henderson-Pabis model, and the Page model. The regression constant, the values of the coefficient of determination (R^2), the mean bias error (MBE), and the root mean-square error (RMSE) for these drying models are given in Table 4. It can be observed in Table 3 that the Page model fitted best with the experimental data compared with the Newton and Henderson-Pabis drying models; this is because the value of R^2 is higher, and MBE and RMSE are lower than the Newton and Henderson-Pabis drying models. Page model for drying of red chilli using a solar assisted heat pump integrated with biomass furnace gave $R^2 = 0.9822$, MBE = 0.0008, and RMSE = 0.0278. Meanwhile, Page model for drying of red chilli using open sun drying gave $R^2 = 0.9410$, MBE = 0.0051, and RMSE = 0.0713.

The variations of dimensionless moisture content data of dried red chilli in a solar assisted heat pump integrated with biomass furnace and open sun drying with drying time fitted with the Page model are shown in Figure 21. It can be seen from this that there was a better fit between experimental data and predicted dimensionless moisture ratios.

The variation of drying rate with dimensionless moisture content of dried red chilli in a solar assisted heat pump integrated with biomass furnace is shown in Figure 22. Drying of red chilli occurred in falling rate period; constant drying rate period was not observed. During the falling rate period, the drying rate decreased continuously with decreasing dimensionless moisture content and increasing drying time. These are similar results as the observation of earlier researchers [7, 31]. From the curve of drying rate with dimensionless moisture content of red chillies, the regression equation was created as

$$DR = 2.4456 + 0.5449 \ln(MR); \quad R^2 = 0.9267. \quad (17)$$

4. Conclusion

The performance of a solar assisted heat pump dryer integrated with biomass furnace has been designed and evaluated for drying red chillies, and drying kinetics of red chillies were evaluated. The averages of the solar collector efficiency, COP of the heat pump, and the efficiency of biomass furnace were estimated to be about 35.1%, 3.84, and 30.7%, respectively. The red chillies were dried from 22 kg with moisture content of 4.26 db to moisture content of 0.08 db which needed 11 hours, with the average drying chamber temperature, drying chamber relative humidity, and an air mass flow rate of

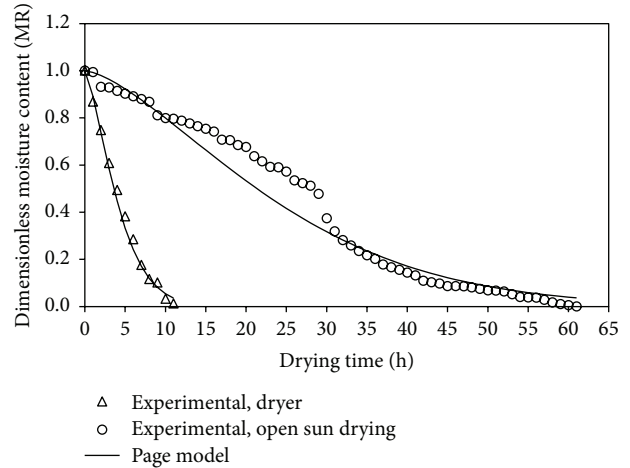


FIGURE 21: The variation of dimensionless moisture content data of dried red chilli in a solar assisted heat pump integrated with biomass furnace and open sun drying and Page model with drying time.

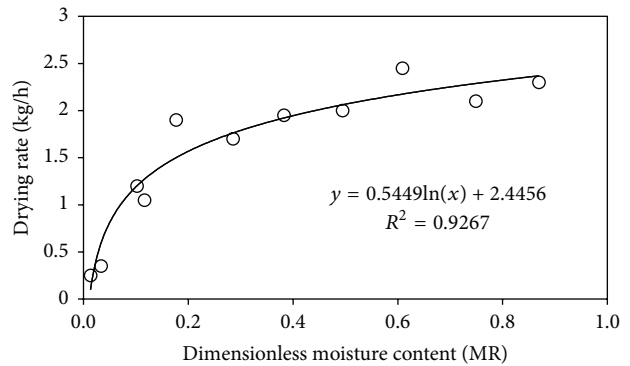


FIGURE 22: The variation of drying rate with dimensionless moisture content of dried red chilli in a solar assisted heat pump integrated with biomass furnace.

70.5°C, 10.1%, and 0.124 kg s^{-1} , respectively, while the open sun drying needed 62 hours. Compared to open sun drying, this dryer yielded a 82% saving in drying time. The drying rate was estimated in average to be about 1.57 kg/h, while the specific moisture extraction rate and thermal efficiency of the dryer were estimated in average to be about 0.14 kg/kWh and 9.03%, respectively. The contributions of heat energy by the collector, condenser, and biomass furnace were estimated in

average to be about 14.74%, 47.39%, and 37.87%, respectively. The biomass fuel (coconut shell charcoal) was needed during drying of about 11 kg. Drying of red chilli occurred in falling rate period; constant drying rate period was not observed. The Page model fitted best with the experimental data compared with the Newton and Henderson-Pabis drying models. It resulted in the highest R^2 and the lowest MBE and RMSE. Result shows that this dryer is capable of drying red chillies quickly because of the high drying rate.

Nomenclature

A_C :	Area of collector (m^2)
$\cos \phi$:	Power factor
a :	Drying constant
MBE:	Mean bias error
$C_{p,air}$:	Specific heat of air ($Jkg^{-1}C^{-1}$)
I :	Line current (ampere)
I_T :	Solar radiation (Wm^{-2})
\dot{m}_{air} :	Air mass flow rate (kg/s)
\dot{m}_{bmf} :	Biomass fuel consumption rate (kg/h)
\dot{m}_{water} :	Mass of water evaporation rate (kg/h)
m_{wetrc} :	Mass of wet red chillies (kg)
E_s :	Energy incident in the plane of the solar collector (kW)
V :	Line voltage (Volt)
CV_{bmf} :	Caloric value of biomass fuel (kcal/kg)
E_{bl} :	Electrical energy consumed by blower (kW)
E_{bmf} :	Heat energy generated by the combustion of biomass fuel (kW)
E_{comp} :	Electrical energy consumed by compressor (kW)
HEC:	Percentage of heat energy contribution (%)
H_{fg} :	Latent heat of vaporization of water (J/kg)
m_d :	Mass of bone dry of the red chillies
M_e :	Equilibrium moisture content on dry basis
M_f :	Final moisture content on wet basis (%)
M_i :	Initial moisture content on wet basis (%)
M_o :	Initial moisture content on dry basis
M_t :	Moisture content at any time on dry basis
m_w :	Mass of water of the red chillies (kg)
N :	Number of observations
n :	Drying constant
Q_u :	Useful energy (kW)
R^2 :	Coefficient of determination
RMSE:	Root mean-square error
T :	Temperature ($^{\circ}C$).

Subscripts

bf:	Biomass furnace
coll:	Solar collector
comp:	Compressor
cond:	Condenser
hp:	Heat pump
i :	Inlet
o :	Outlet.

Competing Interests

The author declared that this current paper has no competing interests.

Acknowledgments

The author would like to thank to Higher Education Directorate of Education and Cultural Ministry of Indonesia (DIKTI) for research funding through the Hibah Bersaing Research Grant scheme.

References

- [1] *Statistical Yearbook of Indonesia*, 2015.
- [2] A. Fudholi, M. Y. Othman, M. H. Ruslan, and K. Sopian, "Drying of Malaysian *Capsicum annum* L. (Red Chili) dried by open and solar drying," *International Journal of Photoenergy*, vol. 2013, Article ID 167895, 9 pages, 2013.
- [3] S. Janjai, P. Intawee, J. Kaewkiew, C. Sritus, and V. Khamvongsa, "A large-scale solar greenhouse dryer using polycarbonate cover: modeling and testing in a tropical environment of Lao People's Democratic Republic," *Renewable Energy*, vol. 36, no. 3, pp. 1053–1062, 2011.
- [4] A. Fudholi, K. Sopian, M. H. Yazdi, M. H. Ruslan, M. Gabbasa, and H. A. Kazem, "Performance analysis of solar drying system for red chili," *Solar Energy*, vol. 99, pp. 47–54, 2014.
- [5] J. Kaewkiew, S. Nabneaan, and S. Janjai, "Experimental investigation of the performance of a large-scale greenhouse type solar dryer for drying chilli in Thailand," *Procedia Engineering*, vol. 32, pp. 433–439, 2012.
- [6] V. Palled, S. R. Desai, and M. Anantachar, "Performance evaluation of solar tunnel dryer for chilly drying," *Karnataka Journal of Agricultural Sciences*, vol. 25, no. 4, pp. 472–474, 2012.
- [7] J. Banout, P. Ehl, J. Havlik, B. Lojka, Z. Polesny, and V. Verner, "Design and performance evaluation of a Double-pass solar drier for drying of red chilli (*Capsicum annum* L.)," *Solar Energy*, vol. 85, no. 3, pp. 506–515, 2011.
- [8] A. M. Leon and S. Kumar, "Design and performance evaluation of a solar-assisted biomass drying system with thermal storage," *Drying Technology*, vol. 26, no. 7, pp. 936–947, 2008.
- [9] A. Artnaseaw, S. Theerakulpisut, and C. Benjapayaporn, "Development of a vacuum heat pump dryer for drying chilli," *Biosystems Engineering*, vol. 105, no. 1, pp. 130–138, 2010.
- [10] M. M. S. Dezfouli, S. Mat, M. H. Ruslan, and K. Sopian, "Evaluation of drying chili by two methods: solar assisted heat pump dryer and open sun drying," in *Proceeding of the 1st International Conference on Environmental Informatics (ENINF '13)*, pp. 112–116, Kuala Lumpur, Malaysia, 2013.
- [11] N. A. Handayani and D. Ariyanti, "Potency of solar energy application in Indonesia," *International Journal of Renewable Energy Development*, vol. 1, no. 2, pp. 33–38, 2012.
- [12] B. Prastowo, "Biomass resource in Indonesia: Indonesia's solid biomass energy potential," in *Proceedings of the Indonesia-German Workshop and Seminar*, pp. 1–15, Institute Technology of Bandung, September 2011.
- [13] B. M. A. Amer, M. A. Hossain, and K. Gottschalk, "Design and performance evaluation of a new hybrid solar dryer for banana," *Energy Conversion and Management*, vol. 51, no. 4, pp. 813–820, 2010.

- [14] M. N. A. Hawlader, S. K. Chou, and M. Z. Ullah, "The performance of a solar assisted heat pump water heating system," *Applied Thermal Engineering*, vol. 21, no. 10, pp. 1049–1065, 2001.
- [15] M. N. Ibrahim, M. S. H. Sarker, A. B. Azizn, and S. P. Mohd, "Drying performance and overall energy requisite of industrial inclined bed paddy drying in Malaysia," *Journal of Engineering Science and Technology*, vol. 9, no. 3, pp. 398–409, 2014.
- [16] T. Swasdisevi, S. Soponronnarit, A. Shujinda, S. Wetchacama, and V. Thepent, "Rice husk furnace for fluidized bed paddy dryer," in *Proceeding of the 2nd Asean Renewable Energy Conference*, pp. 603–612, Puket, Thailand, 1997.
- [17] A. Triyono, *Skripsi: Karakteristik Briket Arang Dari Campuran Serbuk Gergajian Kayu Afrika Dan Sengon Dengan Penambahan Tempurung Kelapa*, Fakultas Kehutanan, Institut Pertanian Bogor, Bogor, Indonesia, 2006.
- [18] N. Srisittipokakun, K. Kirdsiri, and J. Kaewkhao, "Solar drying of andrographis paniculata using a parabolic-shaped solar tunnel dryer," *Procedia Engineering*, vol. 32, pp. 839–846, 2012.
- [19] M. N. A. Hawlader and K. A. Jahangeer, "Solar heat pump drying and water heating in the tropics," *Solar Energy*, vol. 80, no. 5, pp. 492–499, 2006.
- [20] V. Shanmugam and E. Natarajan, "Experimental study of regenerative desiccant integrated solar dryer with and without reflective mirror," *Applied Thermal Engineering*, vol. 27, no. 8-9, pp. 1543–1551, 2007.
- [21] K. Sacilik, A. K. Elicin, and G. Unal, "Drying kinetics of Üryani plum in a convective hot-air dryer," *Journal of Food Engineering*, vol. 76, no. 3, pp. 362–368, 2006.
- [22] E. K. Akpınar, "Drying of mint leaves in a solar dryer and under open sun: modelling, performance analyses," *Energy Conversion and Management*, vol. 51, no. 12, pp. 2407–2418, 2010.
- [23] R. K. Goyal, A. R. P. Kingsly, M. R. Manikantan, and S. M. Ilyas, "Mathematical modelling of thin layer drying kinetics of plum in a tunnel dryer," *Journal of Food Engineering*, vol. 79, no. 1, pp. 176–180, 2007.
- [24] M. Aktaş, I. Ceylan, and S. Yılmaz, "Determination of drying characteristics of apples in a heat pump and solar dryer," *Desalination*, vol. 238, no. 1–3, pp. 266–275, 2009.
- [25] K. Sacilik, R. Keskin, and A. K. Elicin, "Mathematical modelling of solar tunnel drying of thin layer organic tomato," *Journal of Food Engineering*, vol. 73, no. 3, pp. 231–238, 2006.
- [26] I. Ceylan, M. Aktaş, and H. Doğan, "Mathematical modeling of drying characteristics of tropical fruits," *Applied Thermal Engineering*, vol. 27, no. 11-12, pp. 1931–1936, 2007.
- [27] S. Arora, S. Bharti, and V. K. Sehgal, "Convective drying kinetics of red chillies," *Drying Technology*, vol. 24, no. 2, pp. 189–193, 2006.
- [28] S. Kaleemullah and R. Kailappan, "Drying kinetics of red chillies in a rotary dryer," *Biosystems Engineering*, vol. 92, no. 1, pp. 15–23, 2005.
- [29] S. Şevik, "Experimental investigation of a new design solar-heat pump dryer under the different climatic conditions and drying behavior of selected products," *Solar Energy*, vol. 105, pp. 190–205, 2014.
- [30] E. K. Akpınar and Y. Bicer, "Mathematical modelling of thin layer drying process of long green pepper in solar dryer and under open sun," *Energy Conversion and Management*, vol. 49, no. 6, pp. 1367–1375, 2008.
- [31] S. Kaleemullah and R. Kailappan, "Modelling of thin-layer drying kinetics of red chillies," *Journal of Food Engineering*, vol. 76, no. 4, pp. 531–537, 2006.

Research Article

Flexible Bench-Scale Recirculating Flow CPC Photoreactor for Solar Photocatalytic Degradation of Methylene Blue Using Removable TiO₂ Immobilized on PET Sheets

Doaa M. EL-Mekkawi,¹ Norhan Nady,² Nourelhoda A. Abdelwahab,³
Walied A. A. Mohamed,⁴ and M. S. A. Abdel-Mottaleb⁵

¹Physical Chemistry Department, National Research Centre (NRC), 33 Elbohouth Street, P.O. Box 12622, Dokki, Giza, Egypt

²Polymeric Materials Research Department, Advanced Technology and New Materials Research Institute (ATNMRI),
City of Scientific Research and Technological Applications (SRTA-City), New Borg El-Arab City, Alexandria 21934, Egypt

³Polymers and Pigments Department, National Research Centre (NRC), 33 Elbohouth Street, P.O. Box 12622, Dokki, Giza, Egypt

⁴Inorganic Chemistry Department, National Research Centre, 33 Elbohouth Street, P.O. Box 12622, Dokki, Giza, Egypt

⁵Nano-Photochemistry and Solar Chemistry Department, Laboratory of Chemistry, Faculty of Science, Ain Shams University,
Abbassia, 11566 Cairo, Egypt

Correspondence should be addressed to Doaa M. EL-Mekkawi; doaa_egypt@yahoo.com

Received 30 December 2015; Revised 8 February 2016; Accepted 10 February 2016

Academic Editor: Giovanni Palmisano

Copyright © 2016 Doaa M. EL-Mekkawi et al. This is an open access article distributed under the Creative Commons Attribution License, which permits unrestricted use, distribution, and reproduction in any medium, provided the original work is properly cited.

TiO₂ immobilized on polyethylene (PET) nonwoven sheet was used in the solar photocatalytic degradation of methylene blue (MB). TiO₂ Evonik Aeroxide P25 was used in this study. The amount of loaded TiO₂ on PET was approximately 24%. Immobilization of TiO₂ on PET was conducted by dip coating process followed by exposing to mild heat and pressure. TiO₂/PET sheets were wrapped on removable Teflon rods inside home-made bench-scale recirculating flow Compound Parabolic Concentrator (CPC) photoreactor prototype (platform 0.7 × 0.2 × 0.4 m³). CPC photoreactor is made up of seven low iron borosilicate glass tubes connected in series. CPC reflectors are made of stainless steel 304. The prototype was mounted on a platform tilted at 30°N local latitude in Cairo. A centrifugal pump was used to circulate water containing methylene blue (MB) dye inside the glass tubes. Efficient photocatalytic degradation of MB using TiO₂/PET was achieved upon the exposure to direct sunlight. Chemical oxygen demand (COD) analyses reveal the complete mineralization of MB. Durability of TiO₂/PET composite was also tested under sunlight irradiation. Results indicate only 6% reduction in the amount of TiO₂ after seven cycles. No significant change was observed for the physicochemical characteristics of TiO₂/PET after the successive irradiation processes.

1. Introduction

Semiconductor photocatalysis is a fast growing area in terms of both research and commercial activities [1]. In recent years, supported TiO₂ materials have been widely studied for the application on both indoor and outdoor air and water purification [2–5] disinfection and antibacteria [6, 7], as well as self-cleaning surface [8, 9].

Generally, photocatalytic oxidation follows the absorption of energy photons by semiconductors such as TiO₂. Each photon should have energy ($h\nu$) more than or equal to the bandgap energy of TiO₂. The absorbed photon then

promotes the excitation of electron (e⁻) from valence band to conduction band. The generated electrons on conduction band and holes on valence band (h⁺) would then directly or indirectly interact with adsorbed organic pollutants causing their destruction. UVA light energy (wavelength between 300 and 400 nm) is adequate to perform the photocatalytic oxidations on TiO₂ surfaces. Solar energy is a free sustainable source UVA light energy. Egypt has UVA irradiances that reach 40 W/m² or even higher on sunny days [10].

Compound Parabolic Concentrator (CPC) has been extensively interpreted as a good option for solar photochemical applications [11–16]. CPC reactor consists of cylindrical

absorber, on a combined reflecting profile. The reflector geometry mixes two parabolas and one involute whose curves relate to the diameter of the circle and to the concentration ratio.

Titanium dioxide can be used as slurry or fixed inside the CPC photocatalytic reactors. The major obstacle for the practical use of TiO₂ slurries in water treatment was the requirement for the expensive liquid-solid separation. This would consume more efforts, money, and time. In addition, the recovery loss of catalyst might be high [17]. Therefore, catalyst immobilization is the key for successful implementation of heterogeneous photocatalytic oxidation of organic pollutants in water [18, 19].

Some commonly used substrates such as glass, aluminum, and stainless steel are suitable for high temperature annealing treatment after the photocatalyst loading. However, the stiffness and weight of the materials impose limitations for large-scale implementation.

Different methods have been developed on loading of TiO₂ on polymeric sheets from photocatalyst suspensions [20]. All these approaches have to fulfill at least three main needs: the long term stability of the photocatalyst immobilization, its availability for heterogeneous photocatalysis, and the low cost of the deposition procedure, in view of a practical application.

Loading methods, such as sputtering [21, 22], electrochemical deposition [23], spin coating [24], and electrophoretic coating [25], have been previously utilized for the preparation of titania supported thin films. However, these methods are often complicated, costly, and difficult for practical application [26, 27]. Large-scale application of photocatalytic oxidation for water purification can be achieved through direct coating of commercial photocatalysts such as Degussa P25 TiO₂ [28]. When using direct coating, the primary issue of interest is the stability of the coating. Poor adhesions have been reported by direct coating method such as dip coating or spin coating [29, 30], where even slight mechanical abrasion may remove the photocatalyst from the substrate surface. Thus, a binding agent is usually necessary for direct coating in order to form solid adhesion between catalyst and substrate. Either organic polymer or inorganic binding materials have been used for photocatalyst immobilization [31–33]. However, the binder amount may affect the photocatalytic oxidation activity and stability of the coating [34].

Evaluation of the photocatalytic activity of surfaces modified photocatalysts is a crucial point. The dye method is one of the most commonly used methods for the evaluation of the photocatalytically active surfaces. Methylene blue (MB) has been widely addressed as a test pollutant in the evaluation of the photocatalytic activity of semiconductors. MB is extensively used as textile and leather and paper dye. It has been previously demonstrated that films of titania were able to mediate the complete photomineralization of MB [35]. With MB as a highly colored organic material, all what is required for the evaluation process is following up its rate of photocatalytic bleaching via UV/vis spectrophotometry [36, 37]. Recently, the international standards organization (ISO) released a technical standard (ISO 10678:2010) for

“determination of photocatalytic activity of surfaces in an aqueous medium by degradation of methylene blue” [1].

In this work, a bench-scale solar CPC photoreactor has been designed and fabricated for testing the photocatalytic oxidation of organic pollutants. TiO₂ Evonik Aeroxide P25 (previously known as Degussa P25) supported on PET sheets was used as a photocatalytically active surface inside the reactor. Immobilization of TiO₂ on PET was conducted by a simple and cost effective method. MB aqueous solutions were used to study the photocatalytic activity of TiO₂/PET sheets under sunlight. COD analyses were conducted to test the complete mineralization of MB. Durability of TiO₂/PET composite was also tested under sunlight irradiation. The physicochemical characterizations of the prepared TiO₂/PET composite before and after degradation processes were also investigated.

2. Materials and Methods

2.1. Chemicals. TiO₂ Evonik Aeroxide P25 (surface area 50 m²/g) is used as photocatalyst and was provided by Evonik Industries AG, Germany. Polyethylene terephthalate substrates used in this work are nonwoven fabrics, with overall packing density of 0.055 g/cm³. Methylene blue (MB), C₁₆H₁₈ClN₃S·xH₂O, 96%, provided by Fluka, was used as received.

2.2. Preparation of PET/TiO₂ Composite. PET/TiO₂ composite was prepared by dip coating of PET textile substrate with TiO₂. In this study, strips of dimensions (0.2 × 0.7 m²) were cut, weighed, and then immersed in double distilled water for 20 min. Concentrated TiO₂ Aeroxide P25 solution in double distilled water was prepared. The preweighed samples were immersed separately in this solution for 1 h. The wet TiO₂-loaded PET substrates were pressed at 60°C for 20 min. The percentage of loaded TiO₂ was determined and the samples were washed with distilled water several times, and after each time the TiO₂ content was calculated as follows:

$$\text{TiO}_2 \text{ content\%} = \frac{W_2 - W_1}{W_1} \times 100, \quad (1)$$

where W_1 and W_2 are the weights of PET substrate before and after TiO₂ loading.

2.3. Characterizations of PET/TiO₂ Composite

2.3.1. Fourier Transform Infrared (FT-IR) Spectra. The characteristic functional groups of TiO₂ and PET and PET/TiO₂ composite and UV-irradiated PET/TiO₂ composite were investigated by Jasco 3400 FT-IR spectrophotometer, in the range of 4000–400 cm⁻¹.

2.3.2. Scanning Electron Microscope (SEM). In SEM measurements, an electron beam was passed through the specimens followed by scattering them back as electrons and secondary electrons. Backscattered secondary electrons were used to form the image on the computer monitor. The acceleration of the electron beam was 10 kV. This was carried out on Quanta FEG250 Instrument.

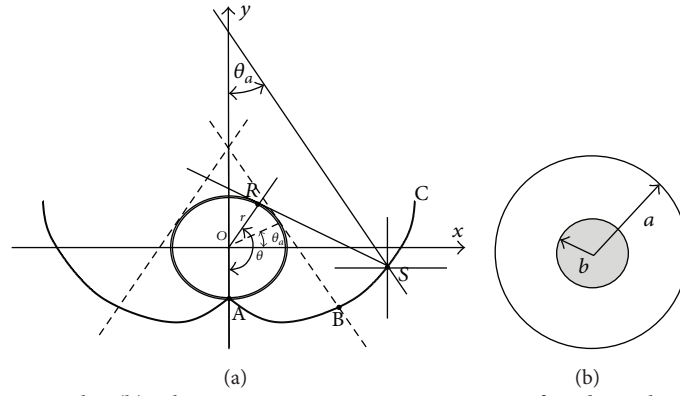


FIGURE 1: (a) CPC acceptance angles, (b) Schematic cross section representation of used annulus to flow the wastewater [38].

2.3.3. Energy Dispersive X-Ray (EDX). The spectra of TiO_2 coated PET fabrics before and after UV irradiation were obtained by EDX measurements. A field emission scanning electron microscope (QUANTA FEG 250) coupled with an energy dispersive X-ray spectrometer (EDX) unit was employed to evaluate the elemental composition of TiO_2/PET sheets. Semiquantitative analyses in the inspection field were conducted using ZFA software where the energy of the emitted electrons for each element was counted in units of weight percent.

2.4. CPC Design

2.4.1. Pipeline Calculations. Compound Parabolic Concentrator (CPC) prototype is made up of seven tubes connected in series, and water would flow from the lowest (the nearest to the ground) to the highest tube and then to a tank. It has been mounted on a platform tilted (30°N local latitude in Cairo). A centrifuge pump was used to circulate wastewater. Rods of temperature-resistant Teflon were used as support for titanium dioxide immobilized in polymer films. These rods were fitted in the middle of glass tubes used to flow the wastewater. As shown in Figure 1(b), the cross-sectional area of annulus A was calculated using $\pi(a^2 - b^2)$, while the wetted perimeter was $2\pi(a + b)$. So, the equivalent diameter is $D_e = 4(\pi(a^2 - b^2))/2\pi(a + b) = 2(a - b)$. The values of $2a$ (the inner diameter of glass tube) and $2b$ (the diameter of support Teflon rod) are specified depending on the required productivity and the limits of light penetration. The Reynolds number can be calculated using equivalent diameter D_e from $R_e = D_e V \rho / \mu$ in which ρ is the density and μ is the dynamic viscosity of used wastewater [39, 40]. The flow is specified in laminar region, and the friction factor f (for plastic surface) can be calculated from $= C/R_e$, where C is a constant, which depends on the ratio a/b [41]. The glass surface is smooth. The head loss is obtained by using $h_f = 2f(L/D_e)(V^2/g)$ and $\Delta P = 2f(L/D_e)(\rho V^2)$. Power to fluid is calculated from $mh_f g$ in which mass flow rate \dot{m} can be obtained from $\dot{m} = \rho V A$. Minor losses of connectors (T and U elbows) between tubes and inlet and outlet were included. The expansion and contraction effects were kept at minimum. The efficiency of the used pump was assumed to be 0.85.

Each tube with 0.25 m length (0.18 m exposed to the sunlight) was made from low iron borosilicate glass

[[$(3 \times 10^{-6})/K$] coefficient of thermal expansion and 1.51–1.54 refractive index]. Seven tubes were connected in series with total irradiated surface 1.26 m^2 and volume equal to $0.723 \times 10^{-3} \text{ m}^3$. The inner diameter of each borosilicate tube is 0.025 m (with 0.015 m glass thickness) and the diameter of the Teflon rod is 0.01 m. The Reynolds number is specified as 700 with average velocity 0.031 m/s. Total volume of the system is $2.5 \times 10^{-3} \text{ m}^3$. The used volumetric flow rate using a centrifugal pump was $0.072 \text{ m}^3/\text{s}$ and the irradiation time per cycle was about 4900 s.

2.4.2. Reflector Design. The reflectors of CPC were designed using the general equation of acceptance angles [38]:

$$\delta = r\theta \quad \text{For } |\theta| \leq \theta_a + \frac{\pi}{2} \quad \text{Part AB in Figure 1(a)} \quad (2a)$$

$$\delta = r \frac{\theta + \theta_a + \pi/2 - \cos(\theta - \theta_a)}{1 + \sin(\theta - \theta_a)} \quad (2b)$$

$$\text{For } \theta_a + \frac{\pi}{2} \leq |\theta| \leq \frac{3\pi}{2} - \theta_a \quad \text{Part BC in Figure 1(a).}$$

δ is the distance of \overline{RS} , θ_a is the half angle of acceptance, and the CPC concentration ratio is given by:

$$C_{\text{cpc}} = \frac{1}{\sin \theta_a}. \quad (3)$$

The reflectors are made of stainless steel 304 with $8 \times 10^{-4} \text{ m}$ thickness. Concentration ratio that equals one and 90 degrees' acceptance half angle (θ_a) were used. Dimension of the collector is 0.17 m width and 0.2 m length.

2.4.3. The Fabricated Bench-Scale Recirculating Flow CPC. The photoreactor has been designed in small bench-scale dimensions (platform = $0.7 \times 0.2 \times 0.4 \text{ m}^3$), so it facilitates conducting lab-scale experiments (see Figure 2). Almost all the parts are flexible. The Teflon rods are removable so several kinds of supported photocatalysts can be used. Moreover, experiments containing slurry photocatalysts can also be conducted. T connectors were used to obtain a flexible lab-scale system (use only one tube or more and withdrawing sample at any tube is possible).

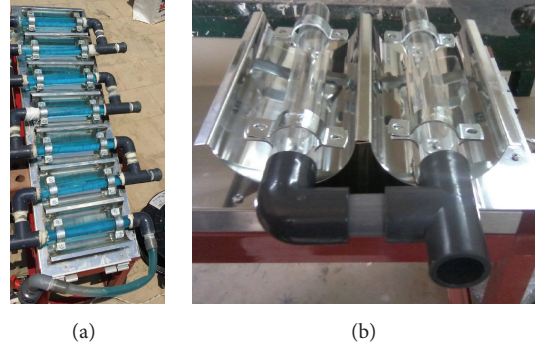


FIGURE 2: Fabricated bench-scale CPC photoreactor was used in this work. It contains seven low iron borosilicate tubes connected in series (a). Each tube was fixed on a reflector fabricated from stainless steel grade 304 (b). T connectors were used to obtain a flexible lab-scale system (use only one tube or more and withdrawing sample at any tube is possible). The simulated wastewater is fed from the lower tube to the upper one against the gravity using centrifuge pump connected to 4-L stirrer tank (not shown). The output treated wastewater was circulated to the tank (closed system). TiO_2 immobilized on PET sheets were wrapped on temperature-resistant removable Teflon rods hanged in the middle of each glass tube.

2.5. Measurement of Solar UV Irradiance. The UV light intensity was measured by YK-35UV radiometer, Taiwan. The radiometer had the same inclination as that of the platform where experiments were conducted.

2.6. Photocatalytic Degradation Experiments. All the experiments were carried out under direct sun irradiation at the roof of the National Research Centre, Cairo, Egypt (latitude 30°N , longitude 31°E) [10]. The initial concentration of MB solution was $1.5 \times 10^{-5}\text{M}$. The total volume (V_T) of the treated MB solution was 2.5 L. This volume is divided into two parts: the total irradiated volume (in glass tubes) (V_i) is 0.723 L and the dead reactor volume (i.e., connectors, tank, pipes, etc.). Prior to the degradation experiments, the photoreactor was covered with black plastic to permit the dark adsorption equilibrium of MB onto TiO_2/PET . After 30 min the plastic cover is removed and the reactor was exposed to the sunlight. The total exposure time for each experiment was approximately 7 hours, with exposure started at 9:00 and finishing at 16:00. During experiments, the MB solution was pumped at flow rate of 1.2 L/min through the glass tubes and finally into the recirculating tank. 4 mL of MB solution was collected for analysis from the reactor tank at timed intervals (1 h) during the degradation experiment.

Durability of the TiO_2/PET sheets was also tested for seven days. The photocatalytic degradation experiment was repeated as mentioned previously using the same TiO_2/PET sheets. Fresh solutions of MB were used at each repetition. The collected data at each day were interpreted using the following equation [42]:

$$t_{30\text{w},n} = t_{30\text{w},n-1} + \Delta t_n \left(\frac{\overline{\text{UV}}}{30} \right) \left(\frac{V_i}{V_t} \right), \quad (4)$$

$$\Delta t_n = t_n - t_{n-1},$$

where t_n is the experimental time for each sample, $\overline{\text{UV}}$ is the average solar ultraviolet radiation measured during Δt_n , and $t_{30\text{w}}$ is a normalized illumination time. In this case, time refers to a constant solar UV power of 30 W/m^2 (typical solar UV power on a perfectly sunny day around noon).

The initial amounts of adsorbed MB molecules on TiO_2/PET sheets at each repetition were calculated as follows:

$$\text{Amount of adsorbed MB} = \frac{C_{0B} - C_{0A}}{SN}, \quad (5)$$

where C_{0B} and C_{0A} are the concentrations of MB in solution before and after the dark adsorption, respectively. The values of C_{0B} and C_{0A} of MB solutions are spectrophotometrically measured at $\lambda_{\text{max}} = 665\text{ nm}$. S is the area of PET strip and N is the number of strips (seven strips).

2.7. UV/Visible Measurements. The change in MB color during the degradation experiments was followed up using UV-visible spectrophotometer, Lambda 40, PerkinElmer, Germany.

2.8. COD Measurements. Hanna COD Meter and Multiparameter Photometer Model HI 83099 was used for the Chemical Oxygen Demand (COD) measurements. The percentages of the COD removal of MB were calculated by applying the following equation:

$$\% \text{ COD} = 100 \times \frac{(C_0 - C_t)}{C_0}, \quad (6)$$

where C_0 is the initial COD value of MB and C_t is the COD value at each time interval of sunlight irradiation.

2.9. Temperature Measurements. The temperature of the treated water was measured during the degradation experiments using Scichem Tech infrared thermometer, gun type professional, SCT658, USA. The maximum temperature achieved inside the reactor during the experiments is 50°C .

3. Results and Discussion

3.1. Preparation and Characterization of TiO_2/PET Sheets. Coating of PET with TiO_2 was conducted by dip coating method followed by exposing to mild heat and pressure. Wet PET polymeric sheets were first immersed in concentrated

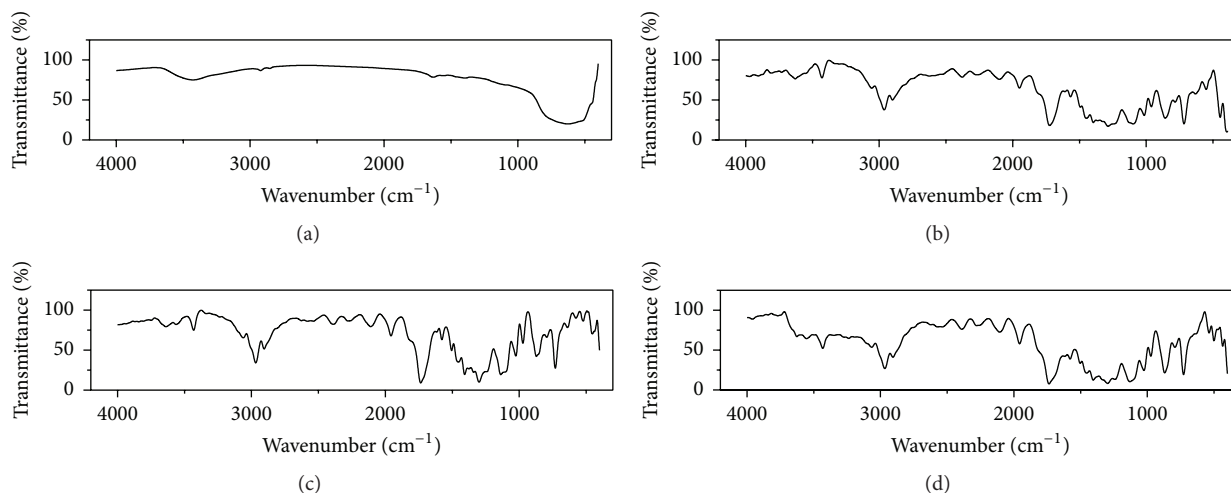


FIGURE 3: FT-IR spectra of (a) TiO_2 , (b) pristine PET, (c) TiO_2 coated PET, and (d) solar irradiated TiO_2 coated PET.

TiO_2 solution. The TiO_2/PET sheets were then heated at 60°C under mild pressure. The mild temperature and pressure result in the dehydration of water molecules formed by the -OH groups at both PET and TiO_2 surfaces leading to successful binding between the adsorbed TiO_2 and PET substrate.

After coating PET sheet with TiO_2 for the first time, the TiO_2 content was found to be 30.5%. Washing with water reduced the TiO_2 content to 26.4% and 25% for one and two times, respectively. From the third to fifth washing, the TiO_2 content decreased slightly from 24.8% to 24.1%. Further washings result in no further leaching.

The FT-IR spectra of TiO_2 and pristine PET and TiO_2 and coated PET are given in Figures 3(a)–3(c). As shown in Figure 3(a), the primary O-H stretching of the hydroxyl functional group appeared at 3427 cm^{-1} . Besides, the band around 1630 cm^{-1} is attributed to the bending vibration H-OH groups. For pristine PET (Figure 2(b)), the main characteristic peaks are as follows: (a) strong peak at 1731 is due to carbonyl group, (b) peak at 3630 cm^{-1} is assigned to end hydroxyl group, and (c) the peak at 3431 cm^{-1} is attributed to overtone vibration of carbonyl group. After coating with TiO_2 (Figure 3(c)), the peak assigned to hydroxyl group was shifted to 3639 cm^{-1} due to bonding with PET.

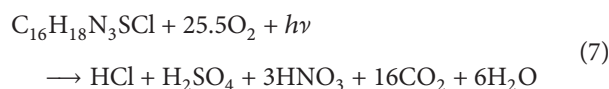
In addition, SEM measurements also reveal the successful preparation of TiO_2/PET sheets. SEM images of TiO_2 , pristine PET, and TiO_2 coated PET are depicted in Figures 4(a)–4(c). As shown in Figure 4(b), pristine PET appeared as smooth yarns. However, after coating (Figure 4(c)), TiO_2 nanoparticles appeared to be homogeneously distributed on PET yarns.

3.2. Solar Photocatalytic Degradation of MB. Under the sunlight irradiation, remarkable changes in the color of MB solution were noticed. Complete decolorization was achieved within 5 hours of light illumination. The change in color was followed up spectrophotometrically. Figure 5(a) shows the change in the absorption spectrum of MB solution with time of illumination. The corresponding measured solar UV doses

during the whole experiment are indicated in Figure 5(b). As shown in Figure 5(a), all peaks in the absorption spectrum of MB decrease as the time of illumination increases suggesting the complete mineralization of MB molecules. It is also worthy to mention that the treated MB solutions were clear during the whole degradation experiment. No suspended TiO_2 particles were observed and consequently there is no need for the separation step. This indicates the efficient performance of the prepared TiO_2/PET sheets.

After complete decolorization, the recirculating colorless MB solution was left for 2 hours for further sunlight exposure. COD of all collected samples were then measured. The results indicated the complete mineralization of the MB molecules (Figure 6).

The complete photomineralization of MB using films of titania has been demonstrated as given in the following equation [35]:



It is clear from Figures 5 and 6 that the mineralization process occurs on a longer time than the oxidative photobleaching of MB. It has been previously also found that the measurement of the rate of photobleaching of MB is expected not to be equivalent to the rate of mineralization of the dye, which is usually a slower process [1].

3.3. Durability of the TiO_2/PET Sheets. Reuse of TiO_2/PET sheets for the photocatalytic degradation of MB inside the CPC reactor was investigated. The solar photodegradation experiments using the same TiO_2/PET sheets were repeated using fresh MB solutions. TiO_2/PET showed a high durability for 7 repetitions at 7 daylight. Comparison between the different photocatalytic experiments during the 7 days was made using the normalized illumination time (t_{30w}) as shown previously in (4). Complete decolorization of fresh MB solutions occurred at approximately $t_{30w} = 300$ min at the first 5 days (Figure 7). The rates of MB photobleaching during

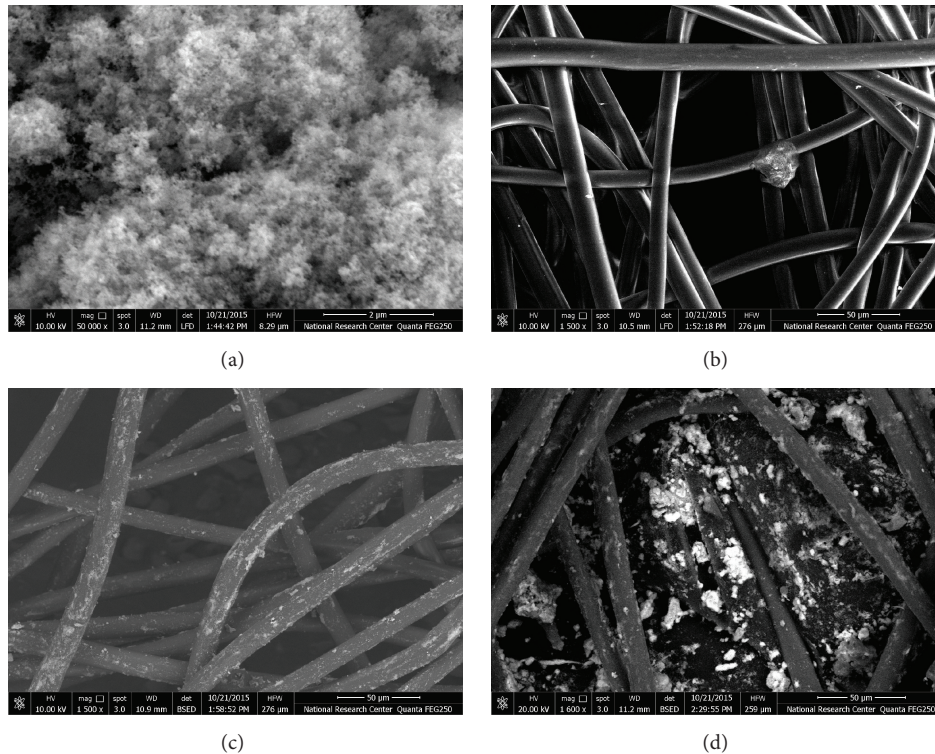


FIGURE 4: SEM images of (a) TiO_2 , (b) pristine PET, (c) TiO_2 coated PET, and (d) solar irradiated TiO_2 coated PET. Bars in (a) and (b)–(d) = $2\ \mu\text{m}$ and $50\ \mu\text{m}$, respectively.

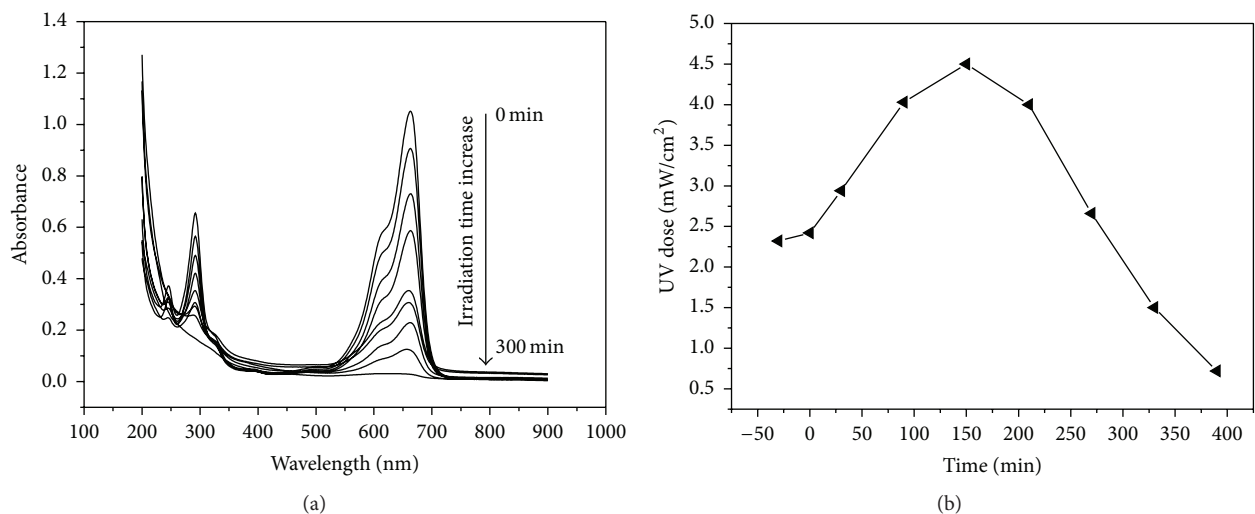


FIGURE 5: (a) Change in the absorption spectrum of MB solution within 5 hours of illumination and (b) the measured solar UV doses at different time intervals of the degradation experiment.

the first to the fifth runs nearly coincided (not shown here). However, as shown in Figure 7, at runs 6 and 7, the rate of photobleaching became slower. No more decolorization was observed for MB solutions after 7 repetitions. On the other side, the color of TiO_2/PET sheets appeared white after first 3 repetitions. This means that, at early use of TiO_2/PET sheets, both adsorbed and dissolved MB molecules were involved in the photooxidative reactions. However, as the number of repetitions increases, the sheets' color turns toward deep blue. The initial amounts of adsorbed MB molecules on TiO_2/PET

sheets at each repetition were calculated according to (5) and listed in Table 1. These experimental and visual observations suggest that the extra adsorption of MB dye on TiO_2/PET sheets results in blocking the photocatalytically active sites of TiO_2 particles.

The physicochemical characteristics of TiO_2/PET sheets were investigated before and after the solar photodegradation experiments. Figure 3(d) represents the IR spectrum of TiO_2/PET sheets after 7 repetitions. As shown in Figure 3(d), no change was observed in the main characteristic peaks of

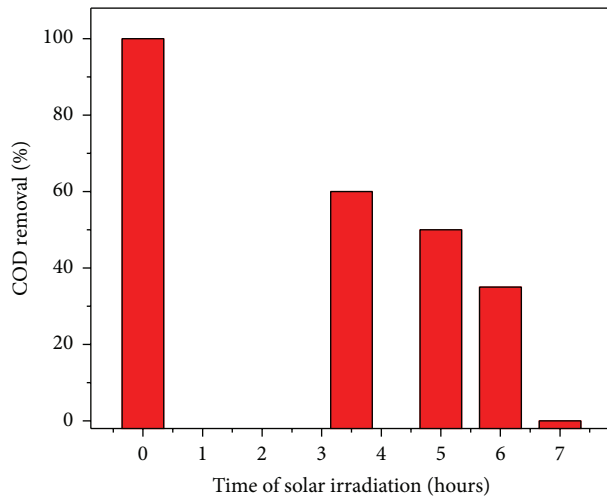


FIGURE 6: The change in the COD removal percentage at different intervals of irradiation time.

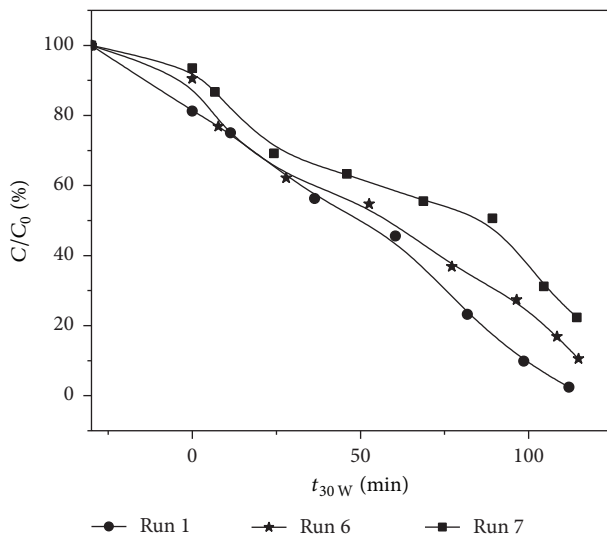
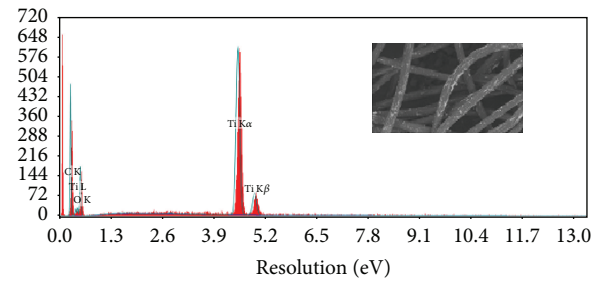


FIGURE 7: Decolorization of MB as a function of t_{30W} (illumination time) on TiO_2/PET surface at different repetitions.

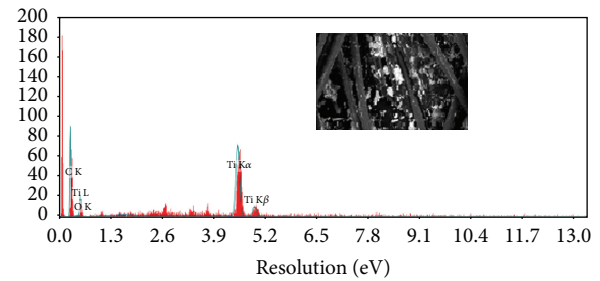
TABLE 1: The initial amount of adsorbed MB molecules on TiO_2/PET sheets at different repetitions.

Number of repetitions	Amount of adsorbed MB (mg/m^2)
1	24.4
2	24.1
3	23.9
4	18.2
5	18.5
6	12.1
7	8.3

the composite. However, the vibrational peak of carbonyl group in PET at 869 cm^{-1} is slightly shifted to 871 cm^{-1} . This shift corresponds to the surface complexation of MB and PET through functional groups ($-\text{CO}$) via hydrogen bonding.



(a)



(b)

FIGURE 8: EDX spectra of (a) TiO_2 coated PET and (b) solar irradiated TiO_2 coated PET.

Besides, some agglomeration for TiO_2 particles was observed by SEM measurements on PET surfaces after 7 repetitions (Figure 4(d)). On the other hand, EDX spectroscopy reveals the good binding of TiO_2 to PET surfaces. As shown in Figures 8(a) and 8(b), the two characteristic signals of Ti atom at 4.6 and 5 eV were observed in the EDX spectra of TiO_2/PET sheets. EDX data indicated that the percentage amounts of TiO_2 on PET surfaces were 42.17 and 36.54%, respectively. This means that only 6% of TiO_2 was lost after seven cycles giving rise to both the high performance and durability of the prepared composite.

4. Conclusions

A home-made designed and fabricated bench-scale solar CPC recirculating photocatalytic reactor has been utilized for the photocatalytic oxidation of organic pollutants. Evonik TiO_2 Aeroxide P25 immobilized on PET was prepared via an effective cost method. The photocatalytic performance of TiO_2/PET sheets was tested using MB as a model pollutant. COD analyses reveal the complete mineralization of MB. Durability of TiO_2/PET composite was also tested under sunlight irradiation. TiO_2/PET showed good durability. Results indicate only 6% reduction in the amount of TiO_2 after seven cycles. No remarkable change was observed for the physicochemical characteristics of TiO_2/PET after the irradiation processes.

Abbreviations

- A: The cross-sectional area of the annulus, m^2
- a : Inner radius of used glass tube, m
- b : Radius of used Teflon rode, m
- C: A constant, which depends on the ratio a/b , dimensionless

C_{cpc} : The CPC concentration ratio, dimensionless
 COD: Chemical oxygen demand, mg/L
 D_e : Equivalent diameter, m
 C_0 : The initial COD value of MB, mg/L
 C_{0A} : Concentration of MB in solution after the dark adsorption, mg
 C_{0B} : Concentration of MB in solution before the dark adsorption, mg
 C_t : The COD value at each time interval of sunlight irradiation, mg/L
 EDX: Energy dispersive X-ray
 f : The friction factor, dimensionless
 FT-IR: Fourier transform infrared
 g : The local acceleration due to gravity, m/s^2
 h_f : The head loss due to friction, m
 k : Kelvin temperature, degree
 L : The length of the pipe, m
 \dot{m} : The mass flow rate, kg/s
 N : Number of PET strips
 MB: Methylene blue
 PET: Polyethylene terephthalate
 R_e : Reynolds number, which is a quantity used to characterize different flow regimes (laminar or turbulent), dimensionless
 t_n : The experimental time for each withdrawn sample, min
 t_{30w} : Normalized illumination time at UV power of 30 W/m^2
 S : Area of PET strip, m^2
 SEM: Scanning electron microscope
 UV: Ultraviolet
 \overline{UV} : The average solar ultraviolet radiation, W/m^2
 V : The mean velocity of the fluid, m/s
 V_f : The irradiated volume of the MB solution, L
 V_T : The total volume of the treated MB solution, L
 W_1 : Weights of PET substrate before loading with TiO_2 , g
 W_2 : Weights of PET substrate after loading with TiO_2 , g
 ρ : The density of the fluid, kg/m^3
 μ : The dynamic viscosity of the fluid $kg/(m\cdot s)$
 π : A mathematical constant, the ratio of a circle's circumference to its diameter, commonly approximated as 3.14159
 δ : The distance of CPC arc, m
 θ_a : The half angle of acceptance, degree
 λ_{max} : Wavelength at the maximum absorption value of MB, nm.

Conflict of Interests

The authors declare that there is no conflict of interests regarding the publication of this paper.

Acknowledgments

The Science and Technology Development Fund (STDF), Egypt, Grant no. 4746, supports this work financially.

References

- [1] A. Mills, C. Hill, and P. K. J. Robertson, "Overview of the current ISO tests for photocatalytic materials," *Journal of Photochemistry and Photobiology A: Chemistry*, vol. 237, pp. 7–23, 2012.
- [2] Y. Dong, Z. Bai, R. Liu, and T. Zhu, "Preparation of fibrous TiO_2 photocatalyst and its optimization towards the decomposition of indoor ammonia under illumination," *Catalysis Today*, vol. 126, no. 3–4, pp. 320–327, 2007.
- [3] O.-H. Park and H.-Y. Na, "Photocatalytic degradation of toluene vapour using fixed bed multichannel photoreactors equipped with TiO_2 -coated fabrics," *Environmental Technology*, vol. 29, no. 9, pp. 1001–1007, 2008.
- [4] D. M. EL-Mekki and H. R. Galal, "Removal of a synthetic dye "Direct Fast Blue B2RL" via adsorption and photocatalytic degradation using low cost rutile and Degussa P25 titanium dioxide," *Journal of Hydro-Environment Research*, vol. 7, no. 3, pp. 219–226, 2013.
- [5] M. Saif, S. M. K. Aboul-Fotouh, S. A. El-Molla, M. M. Ibrahim, and L. F. M. Ismail, "Improvement of the structural, morphology, and optical properties of TiO_2 for solar treatment of industrial wastewater," *Journal of Nanoparticle Research*, vol. 14, article 1227, 2012.
- [6] M. P. Paschoalino and W. F. Jardim, "Indoor air disinfection using a polyester supported TiO_2 photo-reactor," *Indoor Air*, vol. 18, no. 6, pp. 473–479, 2008.
- [7] D. Mihailović, Z. Šaponjić, M. Radoičić et al., "Functionalization of polyester fabrics with alginates and TiO_2 nanoparticles," *Carbohydrate Polymers*, vol. 79, no. 3, pp. 526–532, 2010.
- [8] K. Sawada, M. Sugimoto, M. Ueda, and C. H. Park, "Hydrophilic treatment of polyester surfaces using TiO_2 photocatalytic reactions," *Textile Research Journal*, vol. 73, no. 9, pp. 819–822, 2003.
- [9] M. Saif, S. A. El-Molla, S. M. K. Aboul-Fotouh et al., "Synthesis of highly active thin film based on TiO_2 nanomaterial for self-cleaning application," *Spectrochimica Acta Part A: Molecular and Biomolecular Spectroscopy*, vol. 112, pp. 46–51, 2013.
- [10] S. A. Khalil and A. M. Shaffie, "Prediction of clear-sky biologically effective erythemal radiation (EER) from global solar radiation (250–2800 nm) at Cairo, Egypt," *Advances in Space Research*, vol. 51, no. 9, pp. 1727–1733, 2013.
- [11] J. I. Ajona and A. Vidal, "The use of CPC collectors for detoxification of contaminated water: design, construction and preliminary results," *Solar Energy*, vol. 68, no. 1, pp. 109–120, 2004.
- [12] E. R. Bandala, C. A. Arancibia-Bulnes, S. L. Orozco, and C. A. Estrada, "Solar photoreactors comparison based on oxalic acid photocatalytic degradation," *Solar Energy*, vol. 77, no. 5, pp. 503–512, 2004.
- [13] M. Kus, W. Gernjak, P. F. Ibáñez, S. M. Rodríguez, J. B. Gálvez, and S. Icli, "A comparative study of supported TiO_2 as photocatalyst in water decontamination at solar pilot plant scale," *Journal of Solar Energy Engineering*, vol. 128, no. 3, pp. 331–337, 2006.
- [14] A. M. Amat, A. Arques, F. López, and M. A. Miranda, "Solar photo-catalysis to remove paper mill wastewater pollutants," *Solar Energy*, vol. 79, no. 4, pp. 393–401, 2005.
- [15] O. Prieto, J. Feroso, Y. Nuñez, J. L. del Valle, and R. Irusta, "Decolouration of textile dyes in wastewaters by photocatalysis with TiO_2 ," *Solar Energy*, vol. 79, no. 4, pp. 376–383, 2005.
- [16] S. Malato, J. Blanco, D. C. Alarcón, M. I. Maldonado, P. Fernández-Ibáñez, and W. Gernjak, "Photocatalytic decontamination and disinfection of water with solar collectors," *Catalysis Today*, vol. 122, no. 1–2, pp. 137–149, 2007.

- [17] S. Singh, H. Mahalingam, and P. K. Singh, "Polymer-supported titanium dioxide photocatalysts for environmental remediation: a review," *Applied Catalysis A: General*, vol. 462-463, pp. 178-195, 2013.
- [18] H. S. Hafez, A. El-Hag Ali, and M. S. A. Abdel-Mottaleb, "Photocatalytic efficiency of titanium dioxide immobilized on PVP/AAC hydrogel membranes: a comparative study for safe disposal of wastewater of Remazol Red RB-133 textile dye," *International Journal of Photoenergy*, vol. 7, no. 4, pp. 181-185, 2005.
- [19] A. A. Essawy, A. E.-H. Ali, and M. S. A. Abdel-Mottaleb, "Application of novel copolymer-TiO₂ membranes for some textile dyes adsorptive removal from aqueous solution and photocatalytic decolorization," *Journal of Hazardous Materials*, vol. 157, no. 2-3, pp. 547-552, 2008.
- [20] Y. Ma and J.-N. Yao, "Comparison of photodegradative rate of rhodamine B assisted by two kinds of TiO₂ films," *Chemosphere*, vol. 38, no. 10, pp. 2407-2414, 1999.
- [21] B. Henkel, T. Neubert, S. Zabel et al., "Photocatalytic properties of titania thin films prepared by sputtering versus evaporation and aging of induced oxygen vacancy defects," *Applied Catalysis B: Environmental*, vol. 180, pp. 362-371, 2016.
- [22] Z.-A. Lin, W.-C. Lu, C.-Y. Wu, and K.-S. Chang, "Facile fabrication and tuning of TiO₂ nanoarchitected morphology using magnetron sputtering and its applications to photocatalysis," *Ceramics International*, vol. 40, no. 10, pp. 15523-15529, 2014.
- [23] Y. Yin, R. Huang, W. Zhang, M. Zhang, and C. Wang, "Superhydrophobic-superhydrophilic switchable wettability via TiO₂ photoinduction electrochemical deposition on cellulose substrate," *Chemical Engineering Journal*, vol. 289, pp. 99-105, 2016.
- [24] W. Mekprasart, T. Khumtong, J. Rattanarak, W. Techitdheera, and W. Pecharapa, "Effect of nitrogen Doping on optical and photocatalytic properties of TiO₂ thin film prepared by spin coating process," *Energy Procedia*, vol. 34, pp. 746-750, 2013.
- [25] S. Cabanas-Polo and A. R. Boccaccini, "Electrophoretic deposition of nanoscale TiO₂: technology and applications," *Journal of the European Ceramic Society*, vol. 36, no. 2, pp. 265-283, 2016.
- [26] J. A. Byrne, B. R. Eggins, N. M. D. Brown, B. McKinney, and M. Rouse, "Immobilisation of TiO₂ powder for the treatment of polluted water," *Applied Catalysis B: Environmental*, vol. 17, no. 1-2, pp. 25-36, 1998.
- [27] J. Kasanen, M. Suvanto, and T. T. Pakkanen, "UV stability of polyurethane binding agent on multilayer photocatalytic TiO₂ coating," *Polymer Testing*, vol. 30, no. 4, pp. 381-389, 2011.
- [28] Y. Paz, "Application of TiO₂ photocatalysis for air treatment: patents' overview," *Applied Catalysis B: Environmental*, vol. 99, no. 3-4, pp. 448-460, 2010.
- [29] A. Mills, N. Elliott, I. P. Parkin, S. A. O'Neill, and R. J. Clark, "Novel TiO₂ CVD films for semiconductor photocatalysis," *Journal of Photochemistry and Photobiology A: Chemistry*, vol. 151, no. 1-3, pp. 171-179, 2002.
- [30] M. Keshmiri, M. Mohseni, and T. Troczynski, "Development of novel TiO₂ sol-gel-derived composite and its photocatalytic activities for trichloroethylene oxidation," *Applied Catalysis B: Environmental*, vol. 53, no. 4, pp. 209-219, 2004.
- [31] P. Du, J. T. Carneiro, J. A. Moulijn, and G. Mul, "A novel photocatalytic monolith reactor for multiphase heterogeneous photocatalysis," *Applied Catalysis A: General*, vol. 334, no. 1-2, pp. 119-128, 2008.
- [32] L. L. P. Lim, R. J. Lynch, and S.-I. In, "Comparison of simple and economical photocatalyst immobilisation procedures," *Applied Catalysis A: General*, vol. 365, no. 2, pp. 214-221, 2009.
- [33] M. A. Henderson, "A surface science perspective on TiO₂ photocatalysis," *Surface Science Reports*, vol. 66, no. 6-7, pp. 185-297, 2011.
- [34] I. Sopyan, M. Watanabe, S. Murasawa, K. Hashimoto, and A. Fujishima, "A film-type photocatalyst incorporating highly active TiO₂ powder and fluororesin binder: photocatalytic activity and long-term stability," *Journal of Electroanalytical Chemistry*, vol. 415, no. 1-2, pp. 183-186, 1996.
- [35] R. W. Matthews, "Photocatalytic oxidation and adsorption of methylene blue on thin films of near-ultraviolet-illuminated TiO₂," *Journal of the Chemical Society, Faraday Transactions 1: Physical Chemistry in Condensed Phases*, vol. 85, no. 6, pp. 1291-1302, 1989.
- [36] J. Ryu and W. Choi, "Substrate-specific photocatalytic activities of TiO₂ and multiactivity test for water treatment application," *Environmental Science & Technology*, vol. 42, no. 1, pp. 294-300, 2008.
- [37] B. Tryba, M. Toyoda, A. W. Morawski, R. Nonaka, and M. Inagaki, "Photocatalytic activity and OH radical formation on TiO₂ in the relation to crystallinity," *Applied Catalysis B: Environmental*, vol. 71, no. 3-4, pp. 163-168, 2007.
- [38] J. B. Galvez and S. Malato, *Solar Detoxification*, UNESCO Publishing, Paris, France, 2003.
- [39] P. Ellenberger, *Piping and Pipeline Calculations Manual: Construction, Design Fabrication and Examination*, Elsevier, Philadelphia, Pa, USA, 2014.
- [40] R. H. Perry and D. W. Green, *Perry's Chemical Engineers Handbook*, vol. 6, McGraw-Hill, 1984.
- [41] F. M. White, *Fluid Mechanics*, McGraw-Hill, New York, NY, USA, 7th edition, 2011.
- [42] S. Malato, J. Blanco, A. Vidal et al., "Applied studies in solar photocatalytic detoxification: an overview," *Solar Energy*, vol. 75, no. 4, pp. 329-336, 2003.

Research Article

Noble Metal Decoration and Presulfation on TiO₂: Increased Photocatalytic Activity and Efficient Esterification of *n*-Butanol with Citric Acid

Yu Niu,^{1,2} Pan Huang,^{1,3} Fuying Li,^{2,3} Kai Yang,³ Jinbei Yang,¹ Renzhang Wang,² Cheng Lin,¹ and Ting Qiu¹

¹School of Chemical Engineering, Fuzhou University, Fuzhou 350116, China

²Collaborative Innovation Center of Clean Coal Gasification Technology, Sanming University, Sanming 365004, China

³Research Institute of Photocatalysis, State Key Laboratory of Photocatalysis on Energy and Environment, Fuzhou University, Fuzhou 350002, China

Correspondence should be addressed to Ting Qiu; tingqiu@fzu.edu.cn

Received 5 January 2016; Accepted 11 February 2016

Academic Editor: Andrea Speltini

Copyright © 2016 Yu Niu et al. This is an open access article distributed under the Creative Commons Attribution License, which permits unrestricted use, distribution, and reproduction in any medium, provided the original work is properly cited.

TiO₂ has been widely used as a key catalyst in photocatalytic reactions; it also shows good catalytic activity for esterification reactions. Different sulfated M-TiO₂ nanoparticles (M = Ag, Au, Rh, and Pt) were prepared by photodeposition and ultrasonic methods. The results show that the noble metal nanoparticles, which were loaded onto a TiO₂ surface, slightly affected the crystal phase and particle size of TiO₂. Among all the catalysts, SO₄²⁻/Au-TiO₂ exhibited the best catalytic activity in the esterification reaction for the synthesis of citric acid *n*-butyl acetate and in the decomposition of methyl orange, as confirmed by a high conversion rate of up to 98.2% and 100% degradation rate, respectively. This can be attributed to an increase in the Lewis acidity of the catalyst and increased separation efficiency of electron-hole pairs. This superior catalyst has great potential applications in esterification reactions and wastewater treatments.

1. Introduction

TiO₂ has received much attention because of its superior photocatalytic activity, chemical stability, low cost, and non-toxicity [1–3]. However, pure TiO₂ is not effective for solar-driven applications. This can be achieved by the modification of semiconductors [4, 5], addition of transition metals [6], nonmetal doping [7–10], and use of coupled semiconductors. Several studies have been reported using noble metals as the cocatalysts for the decomposition of dyes [11–13]. The role of noble metals in the acceleration of dye degradation is twofold: (i) the injected electrons from TiO₂ are easily trapped by noble metals, thus achieving more efficient charge separation; (ii) noble metals are excellent catalysts for the reduction of O₂ because of easy activation and adsorption; they can absorb more low-energy visible light. The confined electrons on the surface of noble metal nanoparticles can be rapidly scavenged by O₂, thus avoiding the accumulation of

electrons on noble metals and also increasing the formation of superoxide radical anions [14].

Furthermore, acid-modified titania has great potential as a catalyst [15–18]. SO₄²⁻ modified TiO₂ solid acid nanoparticles exhibited better catalytic activity than pure TiO₂ nanomaterials, because of the coexistence of both Brønsted and Lewis acid sites and many other unique properties [19, 20]. In recent years, various studies have reported the extensive use of SO₄²⁻/TiO₂ solid acid catalyst, an environmentally friendly catalyst, in many catalytic reactions such as esterification and also in the efficient degradation of organic dyes [11, 12, 21]. For example, Wind et al. [22] used sulfated TiO₂ nanotubes as the catalyst for the esterification of acetic acid with cyclohexanol. It showed a high catalytic activity for acetic acid conversion, whereas anatase TiO₂ showed no catalytic activity. Muggli and Ding [12] reported that sulfated TiO₂ was more active and deactivated more slowly than

P-25 during the photocatalytic oxidation of acetaldehyde above 373 K. Sulfate doping has been shown to strengthen visible absorption, thus accelerating the degradation reactions [23].

Although esterification and degradation of organic dyes are seemingly very different, similar catalysts are used in both the reactions and widely used in various industries. Therefore, the utility and versatility of the $\text{SO}_4^{2-}/\text{M-TiO}_2$ catalysts can be verified by using these two very different types of reaction systems; relevant common factors can also be identified to help in the design and preparation of catalysts.

Based on the above considerations, in this study, Ag, Au, Rh, and Pt were selected as the model noble metals to modify a sulfated TiO_2 solid acid composite by a photodeposition method. The synthesized noble metal-modified $\text{SO}_4^{2-}/\text{M-TiO}_2$ ($\text{M} = \text{Ag}, \text{Au}, \text{Rh}, \text{and Pt}$) solid-acid catalysts were characterized by X-ray diffraction (XRD), Brunauer-Emmett-Teller (BET), transmission electron microscopy (TEM), X-ray photoelectron spectroscopy (XPS), Fourier transform infrared spectroscopy (FT-IR), electron spin resonance (ESR), and electrochemical impedance spectroscopy (EIS) analyses. The $\text{SO}_4^{2-}/\text{Au-TiO}_2$ catalyst showed the best catalytic activity for the synthesis of citric acid *n*-butyl acetate (CABu) in the esterification reaction of citric acid (CA) with *n*-butyl alcohol (*n*BuOH) and in the decomposition of methyl orange (MO). Among all the samples, the $\text{SO}_4^{2-}/\text{Au-TiO}_2$ catalyst showed the largest BET specific surface area, strongest intensity of surface-adsorbed sulfate groups in the FT-IR spectrum, highest transient photocurrent response, and smallest EIS radius in the photoelectric chemical test, and strongest signal intensities of the $\text{DMPO}\cdot\text{OH}$ and $\text{DMPO}\cdot\text{O}_2^-$ adducts in the ESR spectrum. The $\text{SO}_4^{2-}/\text{Au-TiO}_2$ catalyst was simultaneously used to esterification reactions and decomposition of organic dyes for industrial applications.

2. Experimental

2.1. Catalyst Preparation. All the chemicals including TiO_2 (pure anatase phase, 99% content, 15 nm, 170 m^2/g , Alfa Aesar) were of reagent grade and were used as received without any further purification.

The noble metal-loaded TiO_2 samples were prepared by the photodeposition method. The TiO_2 powder and a certain amount of noble metal salt were mixed in deionized water; a 300 W Xenon arc lamp (PLS-SXE 300, Beijing Perfectlight) was used as the light source. After irradiating for 5 h, the mixture was filtered, washed, and dried. Then, the resulting solid was filtered and washed twice with deionized water.

The sulfated TiO_2 was prepared by the ultrasonic method. In a typical synthesis, 1 g of TiO_2 powder was dissolved in 15 mL of 1 M H_2SO_4 , and the mixture was sonicated for 1 h. The solid products were collected after filtration, and then dried in an oven at 60 °C for 12 h, and finally calcined in air at 500 °C for 3 h.

The procedure for the preparation of sulfated $\text{SO}_4^{2-}/\text{M-TiO}_2$ ($\text{M} = \text{Ag}, \text{Au}, \text{Rh}, \text{and Pt}$) was the same as that for sulfated TiO_2 ; only TiO_2 was changed to M-TiO_2 .

2.2. Characterization of Catalysts. The phase composition of the samples and crystallite size were determined from their XRD patterns, which were obtained using an X'Pert X-ray diffractometer (PANalytical, Netherlands) using $\text{Cu K}\alpha$ radiation ($\lambda = 0.15406 \text{ nm}$) at a scan rate of $2^\circ/\text{min}$ from 20° to 90° (2θ). The accelerating voltage and applied current were 40 kV and 40 mA, respectively. The crystallite size was calculated from the X-ray line-broadening analysis using the Scherrer formula.

The BET surface areas of the samples were obtained from the N_2 adsorption/desorption isotherms determined at liquid nitrogen temperature (77 K) using an automatic analyzer ASAP 2010 (Micromeritics, China). The samples were degassed for 2 h under vacuum at 350 °C prior to adsorption. The equilibrium time for each point of the BET was 30 min.

The microstructures of the samples were determined by TEM and high-resolution TEM (HRTEM) images at an accelerating voltage of 200 kV using an EM 2010 EX instrument (Jeol, Japan). The samples were deposited on TiO_2 nanoparticles supported by copper grids from the ultrasonically processed ethanol solutions of the products.

The UV-vis diffuse reflection spectra (DRS) were recorded using a Varian Cary 500 Scan UV-vis-NIR spectrometer with BaSO_4 as the reference sample.

The XPS spectra were recorded using a VG ESCALAB 250 XPS system (Thermo Fisher Scientific, USA) using a monochromated $\text{Al K}\alpha$ X-ray source (15 kV, 200 W, 500 mm pass energy = 20 eV) and a charge neutralizer. All the binding energies were referenced to the C 1s peak at 284.6 eV of surface adventitious carbon.

The FT-IR spectra were recorded using a Nicolet 670 FT-IR spectrometer (Nicolet, USA). The samples were pressed using a KBr disk (18 mm diameter, 25–30 mg) preparation apparatus. The samples were dried at 250 °C for 2 h prior to pressing. The FT-IR spectra were recorded using a Nicolet 670 FT-IR spectrometer using a deuterated triglycine sulfate (DTGS) detector at a resolution of 4 cm^{-1} and for 32 scans.

The light/dark short-circuit photocurrent response was recorded using the Epsilon electrochemical workstation (BAS, USA) equipped with a Pt foil counter electrode and saturated calomel electrode (SCE) as the reference electrode. A size of $0.5 \times 0.5 \text{ cm}^2$ sample was coated on a fluorine-doped FTO glass as the working electrode. The three electrodes were immersed in a Na_2SO_4 electrolyte solution (0.5 M), and the working electrode was irradiated by a 365 nm light irradiation (Hamamatsu, LC8). The properties of the catalysts under AC polarization were evaluated by EIS experiments using a potentiostat (Zahner-IM6, Zahner, Germany).

The electron paramagnetic resonance (EPR) spectra were recorded using a Bruker A-300-EPR X-band spectrometer. The $\cdot\text{OH}$ radicals were detected in a dimethyl pyridine *N*-oxide (DMPO)/catalyst/water suspension, and the $\cdot\text{O}_2^-$ radicals in a DMPO/catalyst/methanol suspension (DMPO = 0.05 M, mass of samples = 3 mg, volume of solvent = 0.5 mL, and wavelength of excitation = 365 nm).

TABLE 1: Physicochemical characteristics of as-prepared samples.

Sample	Crystal size (nm) ^a	Pore volume (mL/g)	Pore size (nm)	SBET (m ² /g)
TiO ₂	15.40	0.38	9.04	168.69
SO ₄ ²⁻ /TiO ₂	15.92	0.38	17.10	190.03
SO ₄ ²⁻ /Ag-TiO ₂	15.90	0.40	16.98	193.26
SO ₄ ²⁻ /Au-TiO ₂	15.84	0.41	16.60	198.85
SO ₄ ²⁻ /Rh-TiO ₂	15.86	0.40	16.64	196.08
SO ₄ ²⁻ /Pt-TiO ₂	15.87	0.39	16.92	194.32

^aCalculated from the XRD results.

2.3. Catalytic Performance. The catalytic performance of the solid-acid samples was investigated by evaluating their catalytic activity in the esterification reaction of CA and *n*BuOH to synthesize CABu. The reaction was carried out in a well-stirred oil batch reactor and conducted in a liquid phase. A predetermined amount (12.6 g CA, 27.5 mL *n*BuOH, and 0.25 g catalyst) of the reagents was loaded into the reactor and heated to 400 K for 6 h. The liquid products were analyzed by gas chromatography (GC 7900, Techcomp, China) after each 30 min of the reaction.

The photocatalytic performances of the samples were evaluated from their activities in the decomposition of MO in an aqueous solution; a halogen lamp was used as the light source. Each of these catalysts (100 mg) was added to 100 mL of an aqueous MO solution (20 ppm) at room temperature. To achieve the adsorption-desorption equilibrium, the solution was continuously stirred for 30 min in the dark before the light was turned on. At a specific time interval (15 min) of irradiation, 2 mL aliquots were withdrawn and centrifuged to separate the catalysts. The degradation rate (*D*) of MO was calculated using the equation: $D = (A_0 - A)/A_0 \times 100\%$ (A_0 : initial absorbance; A : final absorbance), by measuring its absorbance at 664 nm using a BK UV-1600 UV-vis spectrometer (Biobase, China).

3. Results and Discussion

3.1. Crystalline Phases and Texture of Samples. The crystalline phases and texture of the samples were characterized by their XRD and N₂ adsorption. Figure 1(a) shows the XRD patterns of TiO₂ and SO₄²⁻/M-TiO₂ (M = Ag, Au, Rh, and Pt) nanoparticles. For all the samples, the peaks at $2\theta = 25.1^\circ$, 37.6° , 48.0° , 53.8° , 55.0° , and 62.7° can be attributed to the typical anatase phase of TiO₂ (JCPDS: 21-1272) [24]. The peaks at $2\theta = 27.4^\circ$, 36.1° , and 54.3° with a lower intensity can be attributed to the rutile crystal structure. The XRD patterns show that the loading of noble metal nanoparticles did not change the crystal structure of TiO₂. For Au-TiO₂, four additional peaks at $2\theta = 38.185^\circ$, 44.381° , 64.571° , and 77.566° were observed; they can be attributed to Au (JCPDS: 04-0784). This indicates that a small amount of Au was formed during the synthesis. Similarly, the corresponding peaks for noble metal-modified nanoparticles were observed corresponding to Ag (JCPDS: 65-2871), Rh (JCPDS: 05-0685), and Pt (JCPDS: 65-2868) in the Ag-TiO₂, Rh-TiO₂, and Pt-TiO₂ powders, respectively (Figure 1(b)).

The change in the physic-chemical properties of the samples was studied by N₂ adsorption-desorption at 77 K. Figure 2 shows the N₂-sorption isotherms (Figure 2(a)) and the corresponding pore-size distribution curves (Figure 2(b)) of TiO₂, SO₄²⁻/TiO₂, and SO₄²⁻/M-TiO₂ (M = Ag, Au, Rh and Pt); their pore sizes are shown in Table 1. It can be seen obviously that they exhibited the typical type-IV adsorption curves with an hysteresis loop between the partial pressure $P/P_0 = 0.45-1.0$, suggesting that TiO₂, SO₄²⁻/TiO₂ and SO₄²⁻/M-TiO₂ maintained the mesoporous structure of the TiO₂ support. The BET surface areas of pure TiO₂, SO₄²⁻/TiO₂, and SO₄²⁻/M-TiO₂ samples were 168.69 m²/g, 190.03 m²/g, and 193.26–198.85 m²/g, respectively. Although the pore sizes increased, the SO₄²⁻/TiO₂ and SO₄²⁻/M-TiO₂ samples still exhibited much higher BET surface areas than TiO₂, possibly because of the reservation of the porous structure inside the particles under supercritical conditions [25]. Even the S-modification further increased the crystal sizes, because the O atom in the O–Ti–O network was replaced with the S atom with a relatively large atomic radius [26]. The results show that all the samples modified with noble metals maintained the mesoporous structure of the TiO₂ support, and noble metal nanoparticles were well dispersed on the surface of TiO₂.

3.2. Morphologies of Samples. The TEM and HRTEM analyses showed the morphologies and distributions of noble metal-modified nanoparticles in the solid samples. The TEM and HRTEM images of TiO₂, SO₄²⁻/TiO₂ and SO₄²⁻/M-TiO₂ (M = Ag, Au, Rh, and Pt) are shown in Figures 3(a1)–3(f1) and 3(a2)–3(f2), respectively. Small noble metal nanoparticles homogeneously dispersed on the surface of a larger TiO₂ phase [27]. No obvious difference was observed in the morphology of these nanoparticles, indicating that the particle dispersion of noble metals cannot change the lattice spacing of TiO₂ (101). The lattice spacing at 0.234 nm, 0.232 nm, 0.232 nm, and 0.209 nm can be attributed to Ag (111), Au (111), Rh (111), and Pt (200), respectively. Au nanoparticles showed the best dispersion on the surface of TiO₂ among all the samples.

3.3. UV-Vis Diffuse Reflection Spectra (DRS). Figure 4 shows the DRS of TiO₂, SO₄²⁻/TiO₂, and SO₄²⁻/M-TiO₂ (M = Ag, Au, Rh, and Pt) samples. An optical absorption threshold was observed at 383 nm, corresponding to the band gap of TiO₂ at 3.2 eV. This value is consistent with the reported value of

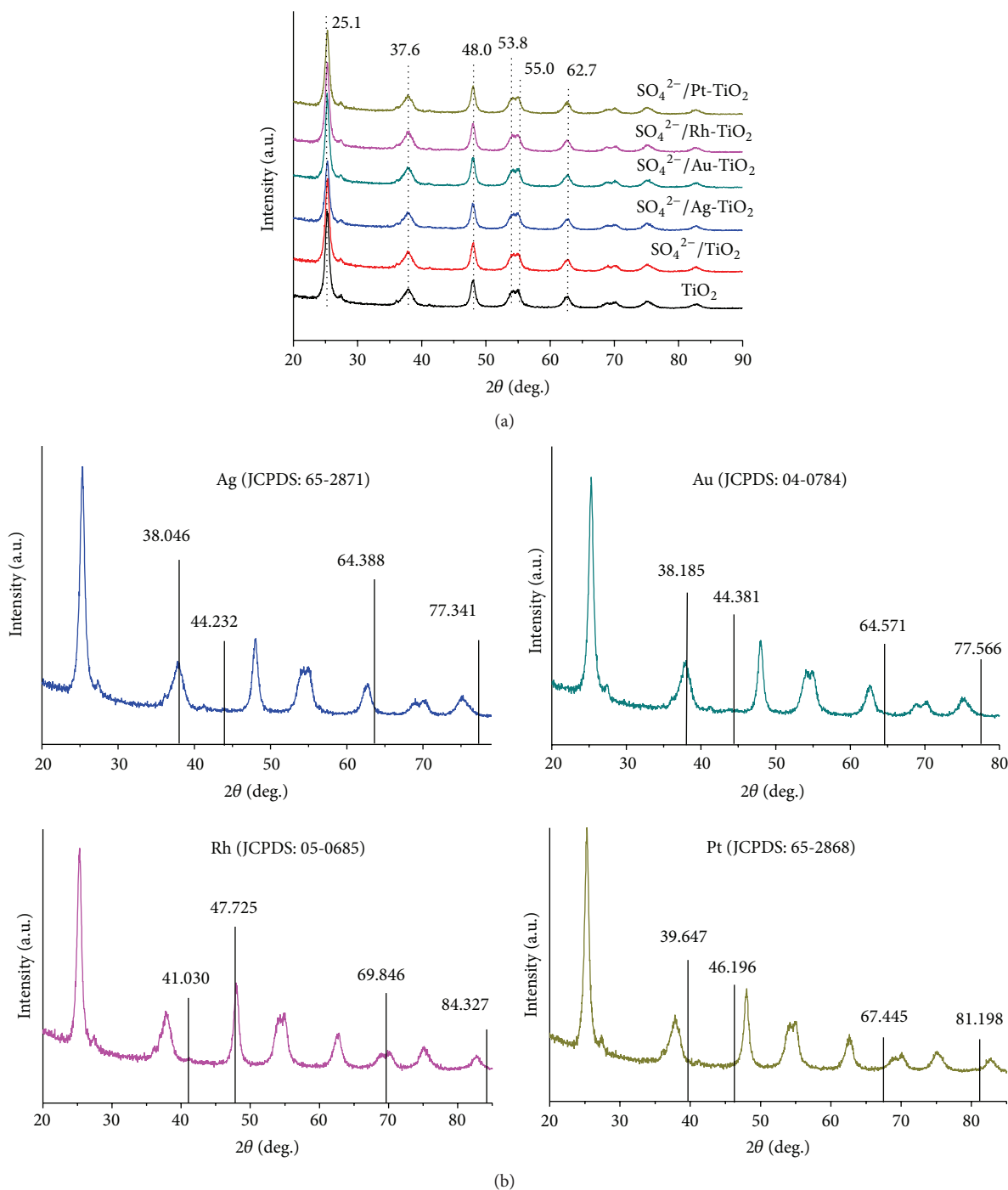


FIGURE 1: (a) XRD patterns of the samples (b) JCPDS of $\text{SO}_4^{2-}/\text{M-TiO}_2$ ($\text{M} = \text{Ag, Au, Rh, and Pt}$) samples.

anatase TiO_2 [28]. Compared to pure TiO_2 and $\text{SO}_4^{2-}/\text{TiO}_2$, the broad absorption bands of $\text{SO}_4^{2-}/\text{M-TiO}_2$ ($\text{M} = \text{Ag, Au, Rh, and Pt}$) can be attributed to the type of loaded noble metal nanoparticles. Clearly, a special strong absorption band was present in the range 450–650 nm for $\text{SO}_4^{2-}/\text{Au-TiO}_2$, corresponding to the located surface plasmon resonance of Au nanoparticles [29]. Therefore, the loading of noble metal nanoparticles into anatase $\text{SO}_4^{2-}/\text{TiO}_2$ may have contributed to the increased activities.

3.4. Surface Chemical States of the Samples. The chemical states of the samples were investigated by XPS. The C 1s peak of the aliphatic carbon with a binding energy (BE) of 284.6 eV was used as the reference. The spectra show no difference in the BEs of O and Ti atoms before and after the noble metal nanoparticles were dispersed homogeneously (Figure 5(a)). The O 1s, Ti 2p, and S 2p peaks of $\text{SO}_4^{2-}/\text{M-TiO}_2$ ($\text{M} = \text{Ag, Au, Rh, and Pt}$) are shown in Figure 5(b), confirming sulfation. The XPS spectra of Ag 3d, Au 4f, Rh 3d, and Pt

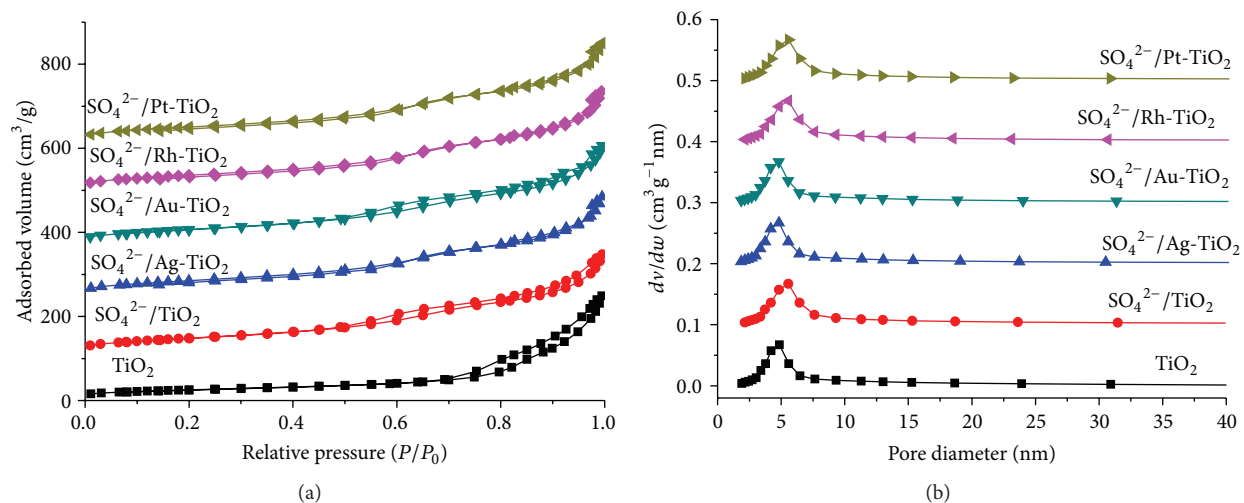


FIGURE 2: (a) N_2 -sorption isotherms and (b) corresponding pore-size distribution curves for the samples.

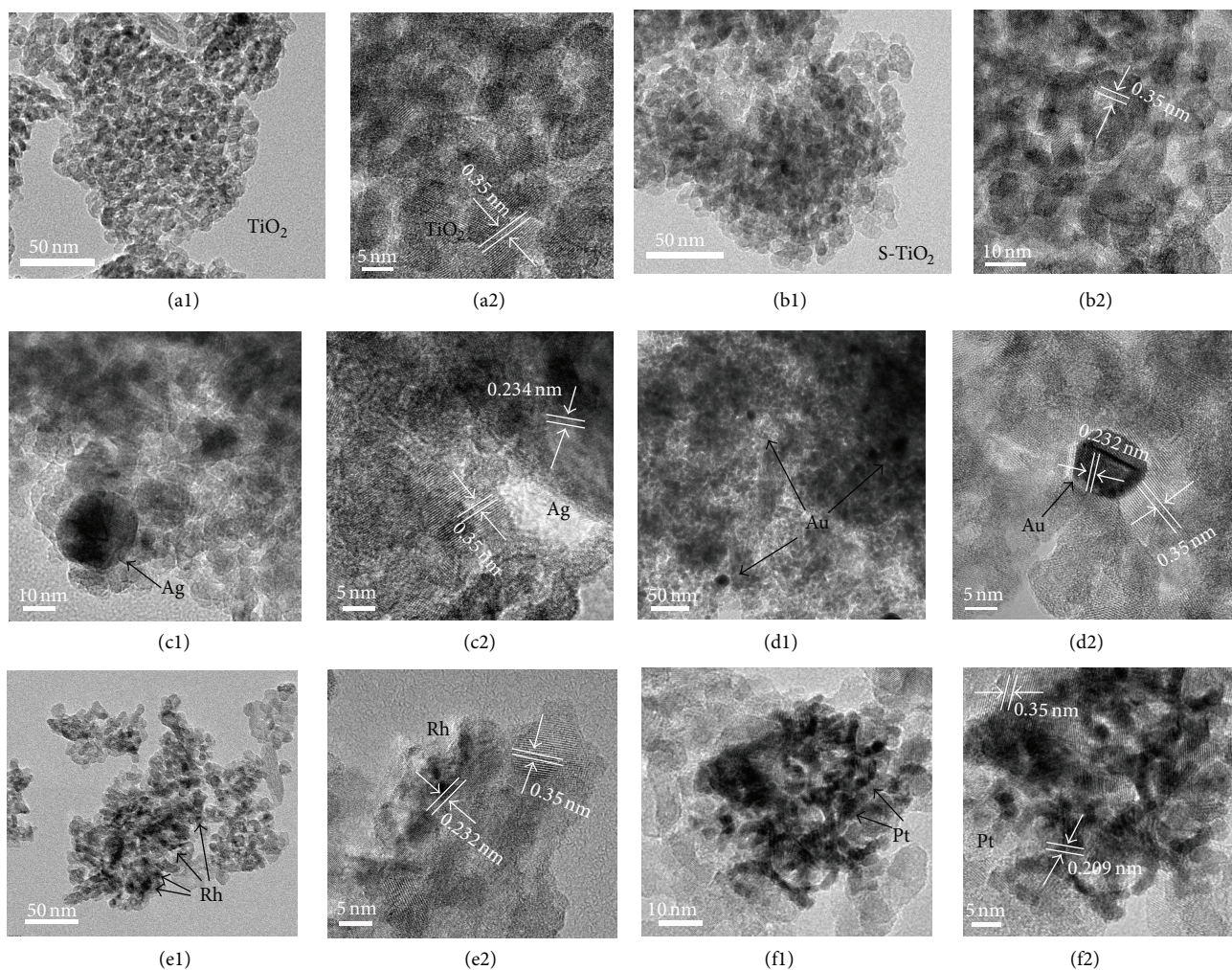


FIGURE 3: TEM and HRTEM images of TiO_2 (a1, a2), SO_4^{2-}/TiO_2 (b1, b2), $SO_4^{2-}/Ag-TiO_2$ (c1, c2), $SO_4^{2-}/Au-TiO_2$ (d1, d2), $SO_4^{2-}/Rh-TiO_2$ (e1, e2), and $SO_4^{2-}/Pt-TiO_2$ (f1, f2) samples.

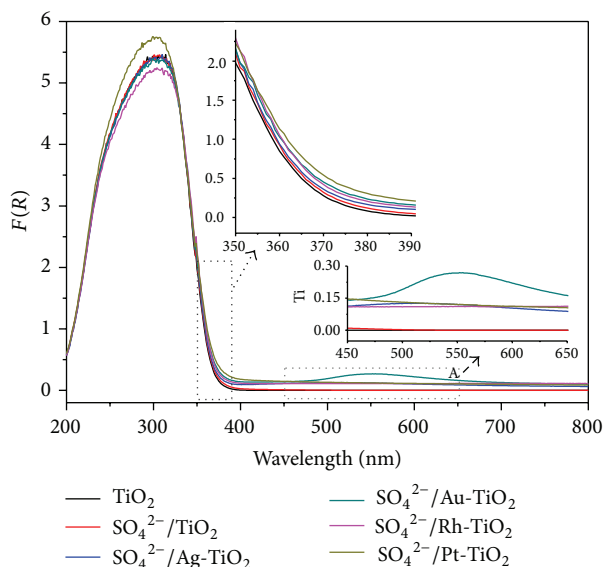


FIGURE 4: UV-vis DRS of the samples.

4f are shown in Figures 5(c)–5(f), respectively. The observed peaks at ca. 368 eV and 374 eV (Figure 5(c)) correspond to the $3d_{5/2}$ and $3d_{3/2}$ core levels of the Ag^0 cations in $\text{SO}_4^{2-}/\text{Ag-TiO}_2$; however, Ag^+ cations could not be identified because of the small differences in Bes [30]. The observed peaks at ca. 83.64 eV and 86.86 eV (Figure 5(d)) correspond to the $4f_{7/2}$ and $4f_{5/2}$ core levels of Au^0 cations in $\text{SO}_4^{2-}/\text{Au-TiO}_2$ [31]. The observed peaks at ca. 307.5 eV and 312.5 eV (Figure 5(e)) correspond to the $3d_{5/2}$ and $3d_{3/2}$ core levels of Rh^0 cations in $\text{SO}_4^{2-}/\text{Rh-TiO}_2$; the second pair of peaks with BEs of ~ 309.45 eV and 314.2 eV can be assigned to the $3d_{5/2}$ and $3d_{3/2}$ core levels of Rh^{3+} valence state, respectively [32]. The peaks at ca. 70.7 eV and 74.0 eV (Figure 5(f)) can be attributed to the $4f_{7/2}$ and $4f_{5/2}$ core levels of Pt^0 cations in $\text{SO}_4^{2-}/\text{Pt-TiO}_2$; the second pair of peaks with BEs of ~ 72.6 eV and 75.9 eV can be assigned to the $4f_{7/2}$ and $4f_{5/2}$ core levels of Pt^{2+} valence state, respectively [33].

Although the Au nanoparticle-loaded sulfated TiO_2 shows only the presence of Au^0 valence state, less than the BE of pure metallic Au, this is probably responsible for the improved catalytic activity. This indicates that the nanoparticles with Au^0 valence states are responsible for the catalytic activity in the esterification reaction to synthesize CABu and decomposition of MO.

3.5. FT-IR Spectra of Samples. The FT-IR spectra of TiO_2 , $\text{SO}_4^{2-}/\text{TiO}_2$, and $\text{SO}_4^{2-}/\text{M-TiO}_2$ ($\text{M} = \text{Ag}, \text{Au}, \text{Rh}, \text{and Pt}$) are shown in Figure 6 band was observed at 1105 cm^{-1} , corresponding to free SO_4^{2-} ; that is, free SO_4^{2-} groups is present in $\text{SO}_4^{2-}/\text{M-TiO}_2$. $\text{SO}_4^{2-}/\text{TiO}_2$ and $\text{SO}_4^{2-}/\text{M-TiO}_2$ showed two bands at 3422 cm^{-1} and 1637 cm^{-1} , in which one can be attributed to adsorbed water and the other can be attributed to the surface hydroxyl group of TiO_2 . The S–O stretching frequencies of $\text{SO}_4^{2-}/\text{TiO}_2$ and $\text{SO}_4^{2-}/\text{M-TiO}_2$ were found at

$1137\text{--}1128 \text{ cm}^{-1}$ and $1068\text{--}1051 \text{ cm}^{-1}$, respectively [34]. Based on the reported S–O stretching frequencies [35, 36], the two new absorption bands at 1133 cm^{-1} and 1062 cm^{-1} for $\text{SO}_4^{2-}/\text{M-TiO}_2$ and $\text{SO}_4^{2-}/\text{TiO}_2$ were the characteristics of chelating bidentate SO_4^{2-} group. Herein, the zero valence state of Au^0 may have changed the surface properties of the catalyst, consistent with the XPS data. The strongest intensity of both the 1133 cm^{-1} and 1062 cm^{-1} bands of the $\text{SO}_4^{2-}/\text{Au-TiO}_2$ can be attributed to the high concentration of surface-adsorbed sulfate groups.

3.6. Photoelectrochemical Properties and ESR Measurements of Samples. The photoelectronic chemical and ESR measurements of the samples were conducted. Figure 7 shows that the transient photocurrent responses of $\text{SO}_4^{2-}/\text{M-TiO}_2$ ($\text{M} = \text{Ag}, \text{Au}, \text{Rh}, \text{and Pt}$) were higher than those of $\text{SO}_4^{2-}/\text{TiO}_2$ and TiO_2 under 365 nm light irradiation (Hamamatsu Co., LC8). This is because the modification with noble metals can significantly enhance the photocurrent. This indicates a more efficient separation of the photoexcited charge carriers on catalysts under their radiation. $\text{SO}_4^{2-}/\text{Au-TiO}_2$ showed the highest transient photocurrent response (Figure 7(a)) and the smallest EIS radius (Figure 7(b)) in all the samples. This indicates that Au nanoparticles may have the best ability to decrease the impedance of electron transfer and increase the charge mobility. This is because of the optimized electronic band structure and interface/surface properties induced by the modification [37–39]. In the esterification reaction for CABu and decomposition of MO, the electron transfer efficiency and formation of active species induced by Au modification also play an important role.

$\cdot\text{OH}$ and $\cdot\text{O}_2^-$ radicals were detected by the DMPO spin-trapping EPR technique, contributing to a better understanding of the photoinduced hole and electrontransfer and photoredox processes as shown in Figures 8(a) and 8(b), respectively. Under the irradiation of $\lambda = 365 \text{ nm}$, four characteristic peaks of the ESR signal of $\text{DMPO}\cdot\text{OH}$ adduct were detected in all the aqueous suspensions of the samples (Figure 8(a)). Six characteristic peaks of the $\text{DMPO}\cdot\text{O}_2^-$ adduct were clearly observed in the ESR spectra (Figure 8(b)). The presence of the active species can be attributed to the reaction of photoinduced holes (h^+) with H_2O molecules [40, 41]. The signal intensities of the $\text{DMPO}\cdot\text{OH}$ and $\text{DMPO}\cdot\text{O}_2^-$ adducts in the ESR spectra of $\text{SO}_4^{2-}/\text{Au-TiO}_2$ were the strongest, indicating that this catalyst has the highest photocatalytic activity in the decomposition of MO. Thus, $\text{SO}_4^{2-}/\text{Au-TiO}_2$ catalyst may have increased the surface acidity for ester synthesis and dye decomposition, great practical value for industrial applications.

3.7. Acid Density Test. The total acid densities of all these catalysts were determined as follows: the samples (0.1 g) were placed in an Erlenmeyer flask and mixed with 15 mL of 2 mol/L NaCl solution. As H^+ ions were present in the SO_3H group of the sulfonated catalyst, they exchanged with Na^+ ions by ultrasonication for 60 min. After the filtration, a 0.02 mol/L NaOH solution was used to titrate the filtrate

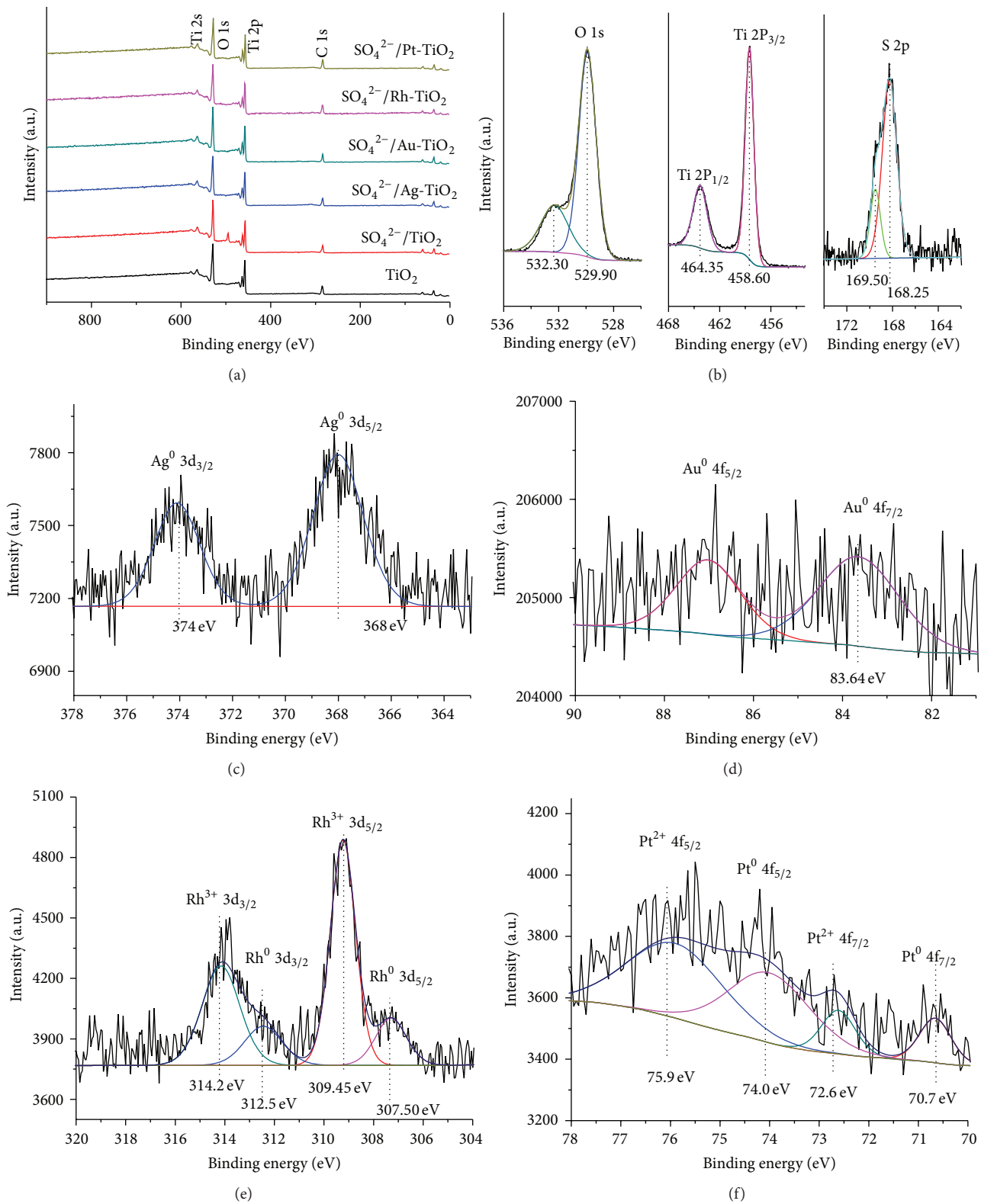


FIGURE 5: XPS (a) spectra of samples, (b) O 1s, Ti 2p, and S 2p peaks of $\text{SO}_4^{2-}/\text{M-TiO}_2$ samples, (c) Ag 3d spectra of $\text{SO}_4^{2-}/\text{Ag-TiO}_2$ sample, (d) Au 4f 3d spectra of $\text{SO}_4^{2-}/\text{Au-TiO}_2$ sample, (e) Rh 3d spectra of $\text{SO}_4^{2-}/\text{Rh-TiO}_2$ sample, and (f) Pt 4f spectra of $\text{SO}_4^{2-}/\text{Pt-TiO}_2$ sample.

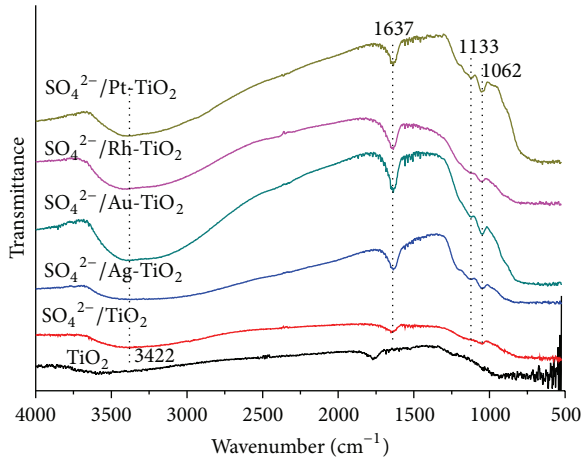


FIGURE 6: FT-IR spectra of samples.

using phenolphthalein as the indicator. When the color of the filtrate changed from colorless to slightly red, the endpoint of the titration reached [35]. The accurate acid quantity was calculated as follows:

$$c(\text{H}^+) = \frac{c(\text{OH}^-) \times \Delta V}{m}, \quad (1)$$

where $c(\text{H}^+)$ is the acid quantity of the sulfated samples; $c(\text{OH}^-)$ is the concentration of the NaOH solution; ΔV is the volume of the NaOH solution consumed in titration; and m is the quality of the samples used in ultrasonication.

The results of acid density are shown in Table 2. The amount of sulfate groups on TiO_2 was $201 \mu\text{mol/g}$ or $\sim 0.71 \text{ SO}_4^{2-}$ groups per nm^2 on the surface of TiO_2 . The surface coverage of SO_4^{2-} was calculated using the BET surface area. However, the amounts of SO_4^{2-} groups on M-TiO_2 ($\text{M} = \text{Ag, Au, Rh, and Pt}$) were $296 \mu\text{mol/g}$, $804 \mu\text{mol/g}$, $542 \mu\text{mol/g}$, $664 \mu\text{mol/g}$, or about 1.32, 2.71, 1.87, 2.05 SO_4^{2-} groups per nm^2 on the surface of TiO_2 , respectively. The surface sulfate groups played an important role in catalysis by offering active acid sites; evidently, the $\text{SO}_4^{2-}/\text{Au-TiO}_2$ had the most abundant Lewis acid sites with the highest acid density, increasing the catalytic activities.

3.8. Esterification Reactions for CABu on Samples. The catalytic activities of the $\text{SO}_4^{2-}/\text{TiO}_2$ and $\text{SO}_4^{2-}/\text{M-TiO}_2$ ($\text{M} = \text{Ag, Au, Rh, and Pt}$) samples were investigated using the CABu esterification reaction shown in Figure 11 as the model reaction, where the mass fraction of the catalyst was 2% of CA.

CABu can be widely used as a solvent in medical products, food packaging materials, and resin plasticizers [42]. Therefore, TiO_2 , $\text{SO}_4^{2-}/\text{TiO}_2$ and $\text{SO}_4^{2-}/\text{M-TiO}_2$ were used to test the performance of the catalysts in the esterification reaction of CA and $n\text{BuOH}$ to synthesize CABu. The results are shown in Figure 9.

Previously, 97.67% CABu conversion was attained at 393 K, with a reaction time of >270 min via the phosphotungstic acid loading of an epoxy resin catalyst [43]. In this

TABLE 2: Amount of SO_4^{2-} groups on prepared catalysts.

Samples	Amount ($\mu\text{mol/g}$)	SO_4^{2-} groups (per nm^2)
TiO_2	201	0.71
Ag-TiO_2 ($w(\text{Ag}) = 0.5\%$)	296	1.32
Au-TiO_2 ($w(\text{Au}) = 0.5\%$)	804	2.71
Rh-TiO_2 ($w(\text{Rh}) = 0.5\%$)	542	1.87
Pt-TiO_2 ($w(\text{Pt}) = 0.5\%$)	664	2.05

TABLE 3: CABu conversion of esterification reaction catalyzed by TiO_2 , $\text{SO}_4^{2-}/\text{TiO}_2$ and $\text{SO}_4^{2-}/\text{M-TiO}_2$ ($\text{M} = \text{Ag, Au, Rh, and Pt}$) solid-acid catalysts^a.

Samples	Conversion (%)
TiO_2	62.3
$\text{SO}_4^{2-}/\text{TiO}_2$	83.5
$\text{SO}_4^{2-}/\text{Ag-TiO}_2$ ($w(\text{Ag}) = 0.5\%$)	86.7
$\text{SO}_4^{2-}/\text{Au-TiO}_2$ ($w(\text{Au}) = 0.5\%$)	98.2
$\text{SO}_4^{2-}/\text{Rh-TiO}_2$ ($w(\text{Rh}) = 0.5\%$)	90.3
$\text{SO}_4^{2-}/\text{Pt-TiO}_2$ ($w(\text{Pt}) = 0.5\%$)	91.3

^aReaction conditions: $T = 400 \text{ K}$, $P = 1 \text{ atm}$, and $T = 6 \text{ h}$.

study, a conversion rate of $>98.2\%$ was achieved at 400 K with $\text{SO}_4^{2-}/\text{Au-TiO}_2$ catalysts; the reaction time was almost the same as that of the previous report. Figure 9 shows the amount of CABu conversion in the esterification reaction using TiO_2 , $\text{SO}_4^{2-}/\text{TiO}_2$ and $\text{SO}_4^{2-}/\text{M-TiO}_2$ as the catalysts. The results show that all the sulfated samples had a better stability over 270 min, consistent with the reported esterification reactions as shown in Table 3. After the reactions reached equilibrium, $\text{SO}_4^{2-}/\text{Au-TiO}_2$ showed the highest catalytic activity for CABu at 400 K, whereas a blank experiment (with TiO_2 catalyst) showed that the conversion of CABu was $<63\%$. Notably, the sulfated TiO_2 catalysts clearly increased the catalytic activity for the esterification reaction to synthesize CABu; the loading of noble metals further increased the catalytic activity. Particularly, $\text{SO}_4^{2-}/\text{Au-TiO}_2$ exhibited the highest conversion rate; this can be attributed to the stronger acidity and the strong interactions between Au and $\text{SO}_4^{2-}/\text{TiO}_2$.

3.9. Photocatalytic Decomposition of MO. The photocatalytic activities of TiO_2 , $\text{SO}_4^{2-}/\text{TiO}_2$, and $\text{SO}_4^{2-}/\text{M-TiO}_2$ ($\text{M} = \text{Ag, Au, Rh, and Pt}$) samples were evaluated by using the photodecomposition of MO under halogen lamp irradiation. The results are shown in Figure 10. Noble metals had a high work function and formed a Schottky barrier between the semiconductor and metal; this trapped the injected electrons of the conduction band in TiO_2 and suppressed the recombination of photoelectrons and holes [44]. Moreover, $\text{SO}_4^{2-}/\text{Au-TiO}_2$ exhibited a much higher activity for the degradation rate than other noble metal-modified TiO_2 samples in the decomposition of MO. This is because Au nanoparticles not only increased the rate of electron-hole pair

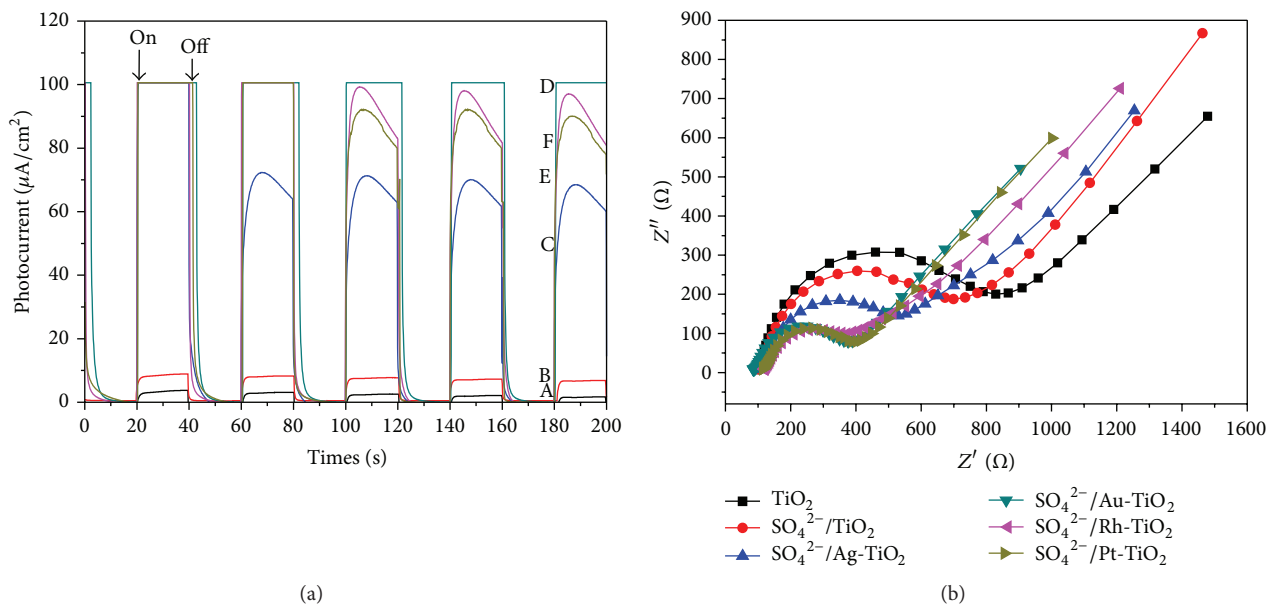


FIGURE 7: (a) Transient photocurrent response of (A) TiO₂, (B) SO₄²⁻/TiO₂, (C) SO₄²⁻/Ag-TiO₂, (D) SO₄²⁻/Au-TiO₂, (E) SO₄²⁻/Rh-TiO₂, and (F) SO₄²⁻/Pt-TiO₂ samples under intermittent UV light irradiation; (b) EIS of samples.

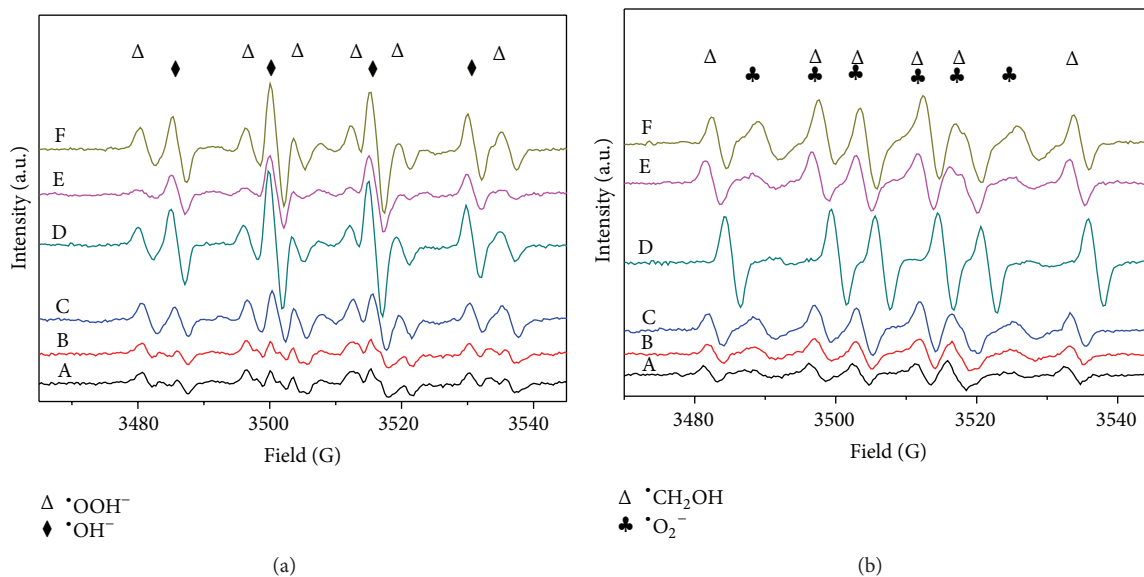


FIGURE 8: DMPO spin-trapping ESR spectra of (A) TiO₂, (B) SO₄²⁻/TiO₂, (C) SO₄²⁻/Ag-TiO₂, (D) SO₄²⁻/Au-TiO₂, (E) SO₄²⁻/Rh-TiO₂, and (F) SO₄²⁻/Pt-TiO₂ samples, at ambient temperature in an aqueous dispersion for (a) DMPO·OH and in a methanol dispersion for (b) DMPO·O₂⁻.

formation but also acted as a photosensitizer to harvest visible photons and converted them to electrical energy [45].

4. Conclusion

Noble metal-modified SO₄²⁻/M-TiO₂ (M = Ag, Au, Rh, and Pt) catalysts were synthesized using the photodeposition and ultrasonic methods. The results show that SO₄²⁻/Au-TiO₂

had the best catalytic activity in the esterification reactions of CA and *n*BuOH for the synthesis of CABu, and also in the decomposition of MO under halogen lamp irradiation. The enhanced activity can be attributed to stronger acidic sites, larger specific surface areas, and the composition or valence states of noble metal nanoparticles. Moreover, the photoelectrochemical and ESR measurements confirmed the highest electron transfer efficiency and formation of ·OH

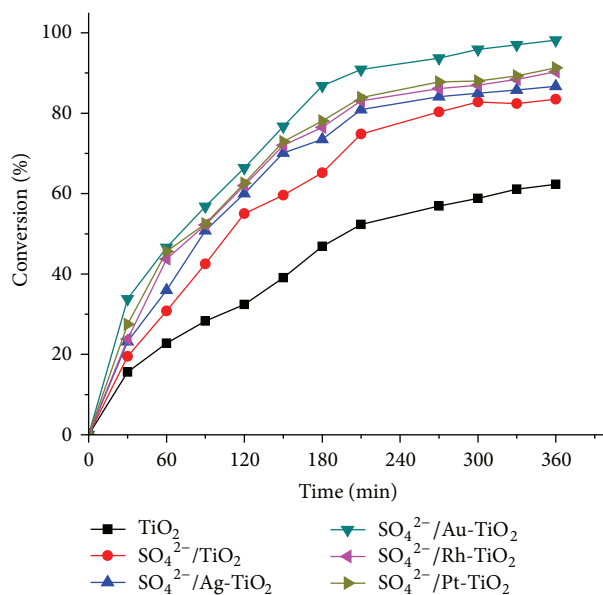


FIGURE 9: Conversion of CABu.

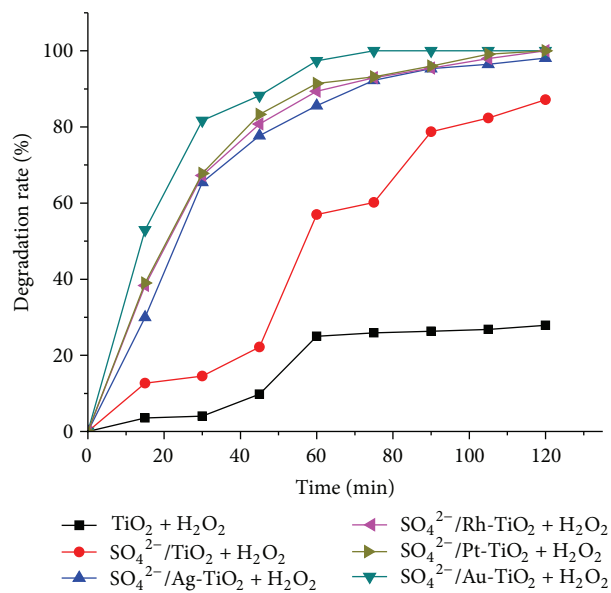


FIGURE 10: Photocatalytic decomposition of samples.

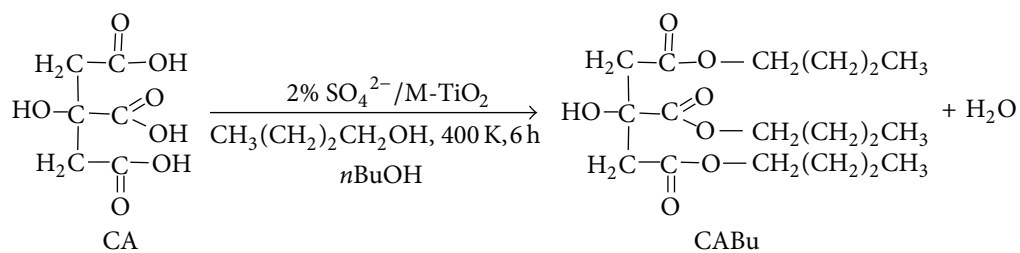


FIGURE 11

and $\cdot\text{O}_2^-$ active species in $\text{SO}_4^{2-}/\text{Au-TiO}_2$ sample. This study indicates a great potential of the solid-acid catalysts for esterification reactions and wastewater treatments.

Conflict of Interests

The authors declare that there is no conflict of interests regarding the publication of this paper.

Acknowledgments

This work was financially supported by the Collaborative Innovation Center of Clean Coal Gasification Technology (XK1403, XK1401), Natural Fund of Fujian Province (2015J01601), and Youth Fund of Fujian Province (JA14290, JA15475).

References

- [1] J. Zhang, Q. Xu, Z. Feng, M. Li, and C. Li, "Importance of the relationship between surface phases and photocatalytic activity of TiO_2 ," *Angewandte Chemie—International Edition*, vol. 47, no. 9, pp. 1766–1769, 2008.
- [2] C. Yu, D. Cai, K. Yang, J. C. Yu, Y. Zhou, and C. Fan, "Sol-gel derived S, I-codoped mesoporous TiO_2 photocatalyst with high visible-light photocatalytic activity," *Journal of Physics and Chemistry of Solids*, vol. 71, no. 9, pp. 1337–1343, 2010.
- [3] A. Fujishima, X. Zhang, and D. A. Tryk, " TiO_2 photocatalysis and related surface phenomena," *Surface Science Reports*, vol. 63, no. 12, pp. 515–582, 2008.
- [4] M. Zhang, C. Chen, W. Ma, and J. Zhao, "Visible-light-induced aerobic oxidation of alcohols in a coupled photocatalytic system of dye-sensitized TiO_2 and TEMPO," *Angewandte Chemie—International Edition*, vol. 47, no. 50, pp. 9730–9733, 2008.
- [5] M. Grätzel, "Dye-sensitized solar cells," *Journal of Photochemistry and Photobiology C: Photochemistry Reviews*, vol. 4, no. 2, pp. 145–153, 2003.
- [6] X.-Q. Gong, A. Selloni, O. Dulub, P. Jacobson, and U. Diebold, "Small Au and Pt clusters at the anatase $\text{TiO}_2(101)$ surface: behavior at terraces, steps, and surface oxygen vacancies," *Journal of the American Chemical Society*, vol. 130, no. 1, pp. 370–381, 2008.
- [7] G. Liu, Y. Zhao, C. Sun, F. Li, G. Q. Lu, and H.-M. Cheng, "Synergistic effects of B/N doping on the visible-light photocatalytic activity of mesoporous TiO_2 ," *Angewandte Chemie—International Edition*, vol. 47, no. 24, pp. 4516–4520, 2008.
- [8] C. Yu and C. Y. Jimmy, "A simple way to prepare C–N-codoped TiO_2 photocatalyst with visible-light activity," *Catalysis Letters*, vol. 129, no. 3–4, pp. 462–470, 2009.
- [9] X. Chen, X. Wang, Y. Hou, J. Huang, L. Wu, and X. Fu, "The effect of postnitridation annealing on the surface property and photocatalytic performance of N-doped TiO_2 under visible light irradiation," *Journal of Catalysis*, vol. 255, no. 1, pp. 59–67, 2008.
- [10] C. Yu, J. C. Yu, and M. Chan, "Sonochemical fabrication of fluorinated mesoporous titanium dioxide microspheres," *Journal of Solid State Chemistry*, vol. 182, no. 5, pp. 1061–1069, 2009.
- [11] P. Periyat, S. C. Pillai, D. E. McCormack, J. Colreavy, and S. J. Hinder, "Improved high-temperature stability and sun-light-driven photocatalytic activity of sulfur-doped anatase TiO_2 ," *Journal of Physical Chemistry C*, vol. 112, no. 20, pp. 7644–7652, 2008.
- [12] D. S. Muggli and L. Ding, "Photocatalytic performance of sulfated TiO_2 and Degussa P-25 TiO_2 during oxidation of organics," *Applied Catalysis B: Environmental*, vol. 32, no. 3, pp. 181–194, 2001.
- [13] S. Liu, J.-H. Yang, and J.-H. Choy, "Microporous SiO_2 - TiO_2 nanosols pillared montmorillonite for photocatalytic decomposition of methyl orange," *Journal of Photochemistry and Photobiology A: Chemistry*, vol. 179, no. 1–2, pp. 75–80, 2006.
- [14] C. Chen, W. Ma, and J. Zhao, "Semiconductor-mediated photodegradation of pollutants under visible-light irradiation," *Chemical Society Reviews*, vol. 39, no. 11, pp. 4206–4219, 2010.
- [15] B. Krishnakumar and M. Swaminathan, "A recyclable and highly effective sulfated TiO_2 -P25 for the synthesis of quinoxaline and dipyrrophenazine derivatives at room temperature," *Journal of Organometallic Chemistry*, vol. 695, no. 24, pp. 2572–2577, 2010.
- [16] J. L. Roper-Vega, A. Aldana-Pérez, R. Gómez, and M. E. Niño-Gómez, "Sulfated titania [$\text{TiO}_2/\text{SO}_4^{2-}$]: a very active solid acid catalyst for the esterification of free fatty acids with ethanol," *Applied Catalysis A: General*, vol. 379, no. 1–2, pp. 24–29, 2010.
- [17] D. Yang, J. Li, M. Wen, and C. Song, "Selective catalytic reduction of NO_x with CH_4 over the in/sulfated TiO_2 catalyst," *Catalysis Letters*, vol. 122, no. 1–2, pp. 138–143, 2008.
- [18] B. Wang, X. Cui, H. Ma, and J. Li, "Photocatalytic activity of $\text{SO}_4^{2-}/\text{SnO}_2$ - TiO_2 catalysts: direct oxidation of n-heptane to ester under mild conditions," *Energy & Fuels*, vol. 21, no. 6, pp. 3748–3749, 2007.
- [19] S. Han, G. Zhang, H. Xi, D. Xu, X. Fu, and X. Wang, "Sulfated TiO_2 decontaminate 2-CEES and DMMP in vapor phase," *Catalysis Letters*, vol. 122, no. 1–2, pp. 106–110, 2008.
- [20] P. Chen, M. Du, H. Lei et al., " $\text{SO}_4^{2-}/\text{ZrO}_2$ -titania nanotubes as efficient solid superacid catalysts for selective mononitration of toluene," *Catalysis Communications*, vol. 18, pp. 47–50, 2012.
- [21] L. Liu, G. Zhang, L. Wang, T. Huang, and L. Qin, "Highly active S-modified ZnFe_2O_4 heterogeneous catalyst and its photo-Fenton behavior under UV-visible irradiation," *Industrial and Engineering Chemistry Research*, vol. 50, no. 12, pp. 7219–7227, 2011.
- [22] S. J. Wind, J. Appenzeller, R. Martel, V. Derycke, and P. Avouris, "Vertical scaling of carbon nanotube field-effect transistors using top gate electrodes," *Applied Physics Letters*, vol. 80, no. 20, pp. 3817–3819, 2002.
- [23] H. Nishikiori, M. Hayashibe, and T. Fujii, "Visible light-photocatalytic activity of sulfate-doped titanium dioxide prepared by the sol-gel method," *Catalysts*, vol. 3, no. 2, pp. 363–377, 2013.
- [24] S. M. Jung and P. Grange, "Characterization and reactivity of pure TiO_2 - SO_4^{2-} SCR catalyst: influence of SO_4^{2-} content," *Catalysis Today*, vol. 59, no. 3, pp. 305–312, 2000.
- [25] X. P. Lin, D. M. Song, X. Q. Gu, Y. L. Zhao, and Y. H. Qiang, "Synthesis of hollow spherical TiO_2 for dye-sensitized solar cells with enhanced performance," *Applied Surface Science*, vol. 263, pp. 816–820, 2012.
- [26] H. Li, X. Zhang, Y. Huo, and J. Zhu, "Supercritical preparation of a highly active S-doped TiO_2 photocatalyst for methylene blue mineralization," *Environmental Science & Technology*, vol. 41, no. 12, pp. 4410–4414, 2007.
- [27] I. Lee, J. B. Joo, Y. Yin, and F. Zaera, "A yolk@shell nanoarchitecture for Au/ TiO_2 catalysts," *Angewandte Chemie—International Edition*, vol. 50, no. 43, pp. 10208–10211, 2011.

- [28] J. R. Sohn and D. G. Lee, "Characterization of zirconium sulfate supported on TiO_2 and activity for acid catalysis," *Korean Journal of Chemical Engineering*, vol. 20, no. 6, pp. 1030–1036, 2003.
- [29] K. Yang, K. Huang, Z. He, X. Chen, X. Fu, and W. Dai, "Promoted effect of PANI as electron transfer promoter on CO oxidation over Au/TiO_2 ," *Applied Catalysis B: Environmental*, vol. 158–159, pp. 250–257, 2014.
- [30] C. Yu, L. Wei, X. Li, J. Chen, Q. Fan, and J. C. Yu, "Synthesis and characterization of Ag/TiO_2 -B nanosquares with high photocatalytic activity under visible light irradiation," *Materials Science and Engineering B: Solid-State Materials for Advanced Technology*, vol. 178, no. 6, pp. 344–348, 2013.
- [31] N. Kruse and S. Chenakin, "XPS characterization of Au/TiO_2 catalysts: binding energy assessment and irradiation effects," *Applied Catalysis A: General*, vol. 391, no. 1, pp. 367–376, 2011.
- [32] Y. V. Larichev, O. V. Netskina, O. V. Komova, and V. I. Simagina, "Comparative XPS study of $\text{Rh/Al}_2\text{O}_3$ and Rh/TiO_2 as catalysts for NaBH_4 hydrolysis," *International Journal of Hydrogen Energy*, vol. 35, no. 13, pp. 6501–6507, 2010.
- [33] T. Huizinga, H. v. T. Blik, J. Vis et al., "XPS investigations of Pt and Rh supported on $\gamma\text{-Al}_2\text{O}_3$ and TiO_2 ," *Surface Science*, vol. 135, no. 1, pp. 580–596, 1983.
- [34] Y.-H. Xu, L.-Y. Wang, Q. Zhang, S.-J. Zheng, X.-J. Li, and C. Huang, "Correlation between photoreactivity and photo-physics of sulfated TiO_2 photocatalyst," *Materials Chemistry and Physics*, vol. 92, no. 2-3, pp. 470–474, 2005.
- [35] T. Yamaguchi, "Recent progress in solid superacid," *Applied Catalysis*, vol. 61, no. 1, pp. 1–25, 1990.
- [36] Y. M. Wang, C. Z. Chen, J. H. Luo et al., "Studies on the acidity, structures and crystalline phases of $\text{SO}_4^{2-}/\text{TiO}_2$, $\text{PO}_4^{3-}/\text{TiO}_2$, $\text{BO}_3^{3-}/\text{TiO}_2$ solid acids," *Chinese Journal of Structural Chemistry*, vol. 18, no. 3, pp. 175–181, 1999.
- [37] G. Zhang, M. Zhang, X. Ye, X. Qiu, S. Lin, and X. Wang, "Iodine modified carbon nitride semiconductors as visible light photocatalysts for hydrogen evolution," *Advanced Materials*, vol. 26, no. 5, pp. 805–809, 2014.
- [38] N. Zhang, M.-Q. Yang, Z.-R. Tang, and Y.-J. Xu, "CdS-graphene nanocomposites as visible light photocatalyst for redox reactions in water: a green route for selective transformation and environmental remediation," *Journal of Catalysis*, vol. 303, pp. 60–69, 2013.
- [39] G. Zhang and X. Wang, "A facile synthesis of covalent carbon nitride photocatalysts by Co-polymerization of urea and phenylurea for hydrogen evolution," *Journal of Catalysis*, vol. 307, pp. 246–253, 2013.
- [40] W. Wu, L. Wen, L. Shen, R. Liang, R. Yuan, and L. Wu, "A new insight into the photocatalytic reduction of 4-nitroaniline to p-phenylenediamine in the presence of alcohols," *Applied Catalysis B: Environmental*, vol. 130–131, pp. 163–167, 2013.
- [41] W. Adam, M. A. Arnold, M. Grüne, W. M. Nau, U. Pischel, and C. R. Saha-Möller, "Spiroiminodihydantoin is a major product in the photooxidation of 2'-deoxyguanosine by the triplet states and oxyl radicals generated from hydroxyacetophenone photolysis and dioxetane thermolysis," *Organic Letters*, vol. 4, no. 4, pp. 537–540, 2002.
- [42] J. Xu, J. Jiang, L. V. Wei, and Y. Gao, "Synthesis of tributyl citrate using solid acid as a catalyst," *Chemical Engineering Communications*, vol. 198, no. 4, pp. 474–482, 2010.
- [43] Y. Huang, J. Guo, N. Yu et al., "Preparation and catalytic performance of $\text{PW}_{12}/\text{E-12}$ over esterification reaction of citric acid with n-Butyl alcohol," *Speciality Petrochemicals*, vol. 32, no. 4, pp. 6–10, 2015.
- [44] V. Subramanian, E. E. Wolf, and P. V. Kamat, "Catalysis with TiO_2 /gold nanocomposites. Effect of metal particle size on the Fermi level equilibration," *Journal of the American Chemical Society*, vol. 126, no. 15, pp. 4943–4950, 2004.
- [45] J. Long, H. Chang, Q. Gu et al., "Gold-plasmon enhanced solar-to-hydrogen conversion on the 001 facets of anatase TiO_2 nanosheets," *Energy & Environmental Science*, vol. 7, no. 3, pp. 973–977, 2014.